Universität Rostock

Traditio et Innovatio

Modeling the Cold Start Process of Spark Ignition Engines

Dissertation

zur Erlangung des akademischen Grades

Doktor-Ingenieur (Dr.-Ing.)

der Fakultät für Maschinenbau und Schiffstechnik

der Universität Rostock

vorgelegt von

Dipl.-Ing. Martin Reißig

aus Hagenow

Hauptreferent:	Prof. Dr.-Ing. E. Hassel
Korreferenten:	Prof. Dr.-Ing. H. Harndorf
	Dr.-Ing. O. Magnor
Tag der Einreichung:	22.07.2011
Tag der Verteidigung:	17.04.2012

Lehrstuhl für Technische Thermodynamik

Universität Rostock

2012

urn:nbn:de:gbv:28-diss2012-0080-0

Dissertation

Fakultät für Maschinenbau und Schiffstechnik

Meiner lieben Frau Maria und meiner Tochter Paulina Isabell

Vorwort

Die vorliegende Dissertation wurde im Rahmen einer Kooperation zwischen dem Lehrstuhl für Technische Thermodynamik der Universität Rostock und der IAV GmbH Gifhorn erarbeitet.

Besonderer Dank gebührt Herrn Prof. Dr.-Ing. habil. E. Hassel und Herrn Dr.-Ing. J. Nocke für die Annahme dieser Arbeit sowie für die regen Diskussionen. Außerdem danke ich den weiteren Gutachtern Herrn Prof. H. Harndorf vom Lehrstuhl für Kolbenmaschinen und Verbrennungsmotoren und Herrn Dr.-Ing. O. Magnor von der IAV GmbH Gifhorn.

Zu gleichen Teilen gebührt Dank den Mitarbeitern der Lehrstühle für Technische Thermodynamik und denen des Lehrstuhls für Kolbenmaschinen und Verbrennungsmotoren sowie der FVTR GmbH für das sehr freundschaftliche Arbeitsklima und die stets geleistete Unterstützung. Insbesondere gilt dies für meinen Kollegen und guten Freund Christof Benz, der mir in vielerlei Hinsicht ein hervorragender Diskussionspartner war.

Weiterhin gilt mein Dank denjenigen Mitarbeitern der IAV GmbH, die mir während meiner Arbeit am Prüfstand in Gifhorn mit Rat und Tat zur Seite standen: Herrn M. Schultalbers, Herrn S. Ollinger, Herrn Dr.-Ing. W. Gottschalk und Herrn Dr. G. Hübner.

Ebenfalls dankend zu erwähnen ist der Beitrag der Studenten, die mit Ihrer Arbeit zum Gelingen dieser Doktorarbeit beigetragen haben, insbesondere der der Herren René Smirnow und Michael Reska.

Zu guter Letzt danke ich meiner Frau, Maria, ohne deren Unterstützung diese Arbeit nicht in dieser Form entstanden wäre.

Rostock im Juli 2011

Kurzfassung

Der Kaltstart eines Verbrennungsmotors im Allgemeinen und der eines Ottomotors im Besonderen stellt die Fahrzeug-Hersteller vor Herausforderungen, die im sonstigen Motorbetrieb nicht auftreten. So kommt insbesondere der Start-Robustheit eine herausragende Bedeutung zu, da das Hochfahren des Motors die Voraussetzung für jegliche weitere Optimierung darstellt. Die Robustheit ist hingegen in erster Linie von einem erfolgreichen Durchbrennen des Kraftstoff-Luft-Gemisches abhängig und somit von der Qualität des Gemisches an sich. Als kritische Randbedingung ist hier die niedrige Temperatur im Brennraum zu nennen, durch die die Gemischbildung verschleppt abläuft, so dass hauptsächlich leichtsiedende Komponenten des Kraftstoffs verdampfen, die höhersiedenden jedoch dazu neigen, die Wände zu benetzen. Da während des Kaltstarts außerdem nur ungenügende Daten über das Kraftstoff-Luft-Gemisch zu Verfügung stehen - die Lambda-Sonde geht im regulären Start erst nach einer Aufheizzeit in Betrieb - kann nicht auf die Gemischqualität geregelt werden. Dies führt nicht nur zu einer eingeschränkt kontrollierbaren Energieumsetzung mit möglichen Fehlverbrennungen bzw. partiellen Verbrennungen, sondern infolgedessen auch zu erhöhten Schadstoff-Emissionen, insbesondere HC- und CO-Emissionen. Eine Vorsteuerung stellt hier den möglichen Kompromiss dar, relevante Stellgrößen in Abhängigkeit messbarer Größen, wie z. B. Kühlwassertemperatur, Umgebungsdruck und Motordrehzahl, anzupassen. Die Bedatung dieser Vorsteuerung ist jedoch durch die zahlreichen gegenseitigen Abhängigkeiten der Stellgrößen sowie den hohen experimentellen Aufwand, den Kaltstartmessungen erfordern, zeit- und kostenintensiv.

Wie in anderen Bereichen der Produktentwicklung üblich, wird in vorliegender Arbeit zu diesem Zweck ein mathematisches Modell vorgestellt, das in der Lage ist, den ottomotorischen Kaltstart vorherzusagen. Das Modell basiert auf einer null-dimensionalen thermodynamischen Beschreibung des Gaspfades von der Ansaugung der Luft über die Verbrennung

im Zylinder bis zum Ausschieben des Abgases. Wie gezeigt werden konnte, lässt sich die Verbrennung von homogenen sowie von geschichteten Gemischen mittels eines fraktalen Ansatzes für die Beschreibung der voll ausgebildeten turbulenten Flamme abbilden. Der aus der Verbrennung und sekundären Phänomenen wie Wandwärmestrom und Leckage resultierende Zylinderdruck wird über ein mechanisches Modell in ein Antriebsmoment der Kurbelwelle überführt, womit sich einschließlich der Massenträgheiten sowie Verlustmomenten der Drehzahlhochlauf beschreiben lässt.

Da die verwendeten Submodelle zumindest teilweise auf empirischen bzw. semi-empirischen Ansätzen beruhen, ist eine Anpasssung der dann applizierten Modellkonstanten an geeignete Messungen, die sowohl den Kaltstart als auch Stationärpunkte umfassen, nötig. Verwendung fand hierzu ein globaler Optimierungsalgorithmus, der es ermöglicht, nicht nur lokale, sondern auch globale Optima einer Zielfunktion aufzufinden. Nach Anpassung der Modellkonstanten ist das Motormodell dazu in der Lage, den ottomotorischen Kaltstart mit geringem Rechenaufwand und annehmbarer Genauigkeit abzubilden.

Durch eine Variation der Eingangsparameter, sowohl was Geometrie- und Steuergerätegrößen als auch Umgebungsbedingungen betrifft, konnten grundsätzliche Abhängigkeiten des Kaltstartprozesses aufgezeigt werden. Zusätzlich dazu lässt sich mit einer Kombination aus Motormodell und Optimierungsalgorithmus eine automatisierte Optimierung des Kaltstarts durchführen. Weiterhin konnte nachgewiesen werden, dass eine Evaluierung von gemessenen Daten möglich ist, d.h. indirekt auf nicht messbare Größen geschlossen werden kann. Dies gilt für gemessene hochaufgelöste Drehzahlsignale, aus denen sich für einen Start zyklusaufgelöst indizierte Mitteldrücke abschätzen lassen, sowie für gemessene Zylinderdrücke, mit denen Aussagen über die Gemischbildung getroffen werden können.

Abstract

In terms of ECU calibration, an SI engine cold start still implies challenges for the OEMs that do not occur during other operation modes. Special emphasis lies on start robustness since every other optimization criterion depends on a reliable engine run-up. Robustness itself is dependent upon a combustion that is as complete as possible and thus on the mixture quality. Mixture preparation is hampered by low temperatures in the cylinder during cold start, favoring evaporation of low boiling fuel components while high boiling components tend to accumulate on the cylinder walls. Since measurement data is limited during start - the EGO-sensor is inactive due to low temperatures - the injection can not be controlled by means of mixture quality. Energy conversion is therefore not optimal leading to misfires and pollutant emissions such as HC and CO emissions. An open loop control of relevant ECU parameters in dependence upon existent measurement variables, such as engine block temperature, ambient pressure and engine speed, is a possible compromise here. Calibration of this open loop controllers on the other hand is cost intensive and time consuming due to the high effort that is necessary for cold start experiments and the numerous interdependencies between ECU parameters.

As with other fields of product development, a mathematical model is presented in this work, which accommodates with the task to predict the cold start of SI engines. The model bases upon a zero-dimensional thermodynamic description of the gas state incorporating intake of air, combustion of the fuel-air mixture and finally discharge of the flue gas. A description of the combustion of homogeneous as well as stratified charges by a fractal approach for the fully established turbulent flame proved to be successful. The cylinder pressure resulting from the combustion and secondary effects such as wall heat transfer and gas leakage across the piston rings is transferred via a mechanical model of the power train into a driving torque. Quantifying loss torques as well as inertias in addition to this driving torque enables the

simulation of the engine run-up.

The submodels incorporated in the complete engine model are at least partially of empirical or semi-empirical nature. This requires fitting model constants to appropriate measurements comprising cold starts as well as stationary engine operation. To this end, a global optimization algorithm (Simulated Annealing) is applied to identify the best parameter values. As a result, the engine model is capable of simulating the cold start with low computational effort on the one hand and reasonable accuracy on the other.

A variation of input parameters, including geometric as well as ECU parameters in addition to boundary conditions, show the sensitivity of the process at hand. Apart from a pure description of interdependencies, an optimization of the cold start in regard to different criteria can be achieved by the mentioned optimization algorithm. Furthermore, it could be demonstrated that evaluations of measurement data can be realized in order to increase information gain from a given cold start measurement. This comprises heat release rate calculation from cylinder pressure as well as equivalence ratio and additionally estimation of indicated mean effective pressure from engine speed data.

Contents

List of Figures

List of Tables

Nomenclature

Symbol	Unit	Meaning
A	m^2	Area
A_T	m^2	Turbulent flame surface
$(A/F)_s$	-	Stoichiometric air-fuel ratio
B	m	Bore of cylinder
b	$^{Nm\ s}/_{rad}$	Damping constant
c	$^{Nm}/_{rad}$	Spring constant
c_p	$^{J}/_{kg\ K}$	Specific heat capacity at constant pressure
c_V	$^{J}/_{kg\ K}$	Specific heat capacity at constant volume
D	m	Diameter
E	J	Energy
$fmep$	Pa	Friction mean effective pressure
H	J	Enthalpy
$\dot{H}$	$^{J}/_{s}$	Enthalpy flow
h	$^{J}/_{kg}$	Specific enthalpy
H_u	$^{J}/_{kg}$	Lower heating value

Symbol	Unit	Meaning
$imep$	Pa	Indicated mean effective pressure
L	m	Flame wrinkling scale
L		Lagrange function
l	m	Connecting rod length
l_v	m	Valve lift
m	kg	Mass
$\dot{m}$	$^{\mathrm{kg}}/_{\mathrm{s}}$	Mass flow
MW	$^{\mathrm{kg}}/_{\mathrm{kmol}}$	Molar weight
N	kmol	Amount of substance
N	-	Number
n	-	Polytropic index
n	min^{-1}	Crankshaft speed
P	W	Power
p	Pa	Pressure
Q	J	Heat
$\dot{Q}$	$^{\mathrm{J}}/_{\mathrm{s}}$	Heat flow
r	m	Radius
r	m	Crank radius
R_m	$^{\mathrm{J}}/_{\mathrm{kmol\,K}}$	Universal gas constant

Symbol	Unit	Meaning
s	m	Position
t	s	Time
U	J	Internal energy
u	$^{\mathrm{J}}/_{\mathrm{kg}}$	Specific internal energy
u	$^{\mathrm{m}}/_{\mathrm{s}}$	Velocity
V	m^3	Volume
W	J	Work
X	-	Mole fraction
Y	-	Mass fraction

Greek symbols

Symbol	Unit	Meaning
α_{th}	$^\circ$	Throttle plate angle
ε	-	Compression ratio
ϑ	$^\circ$C	Temperature
κ	-	Isentropic coefficient
λ	-	Equivalence ratio
λ_c	-	Connecting rod ratio
λ_V	-	Volumetric efficiency
ν	$\mathrm{m^2/s}$	Kinematic viscosity
ρ	$\mathrm{kg/m^3}$	Density
σ	$^\circ$	Valve seat angle
τ	s	Time constant
Φ	-	Equivalence ratio
ϕ	-	Relative humidity of air
φ	$^\circ$	Crank angle

Indices

Symbol	Meaning
a	Air
aux	Auxiliary systems
b	Burnt
c	Compression
cr	Critical
$crev$	Crevices
cyl	Cylinder
d	Displacement
eoi	End of injection
ev	Exhaust valve
evc	Exhaust valve closed
evo	Exhaust valve opened
ext	External
F	Flame
F	Flywheel
f	Fuel
im	Intake manifold
ign	Ignition

Symbol	Meaning
in	Inflow
iv	Intake valve
ivc	Intake valve closed
ivo	Intake valve opened
i, j, k	Enumeration indices
kin	Kinetic
L	Laminar
$leak$	Leakage
mix	Mixture
osc	Oscillating
out	Outflow
P	Piston
pot	Potential
$prim$	Primary
R	Chemical reaction
res	Residual
rot	Rotational
sec	Secondary
T	Taylor

Symbol	Meaning
T	Turbulent
th	Throttle
tr	Transition
u	Unburnt
V	Volume
v	Valve
vs	Valve seat
W	Wall

Abbreviations

Symbol	Meaning
CFD	Computational Fluid Dynamics
CO	Carbon monoxide
$DISI$	Direct Injection Spark Ignition
$DOHC$	Double Overhead Camshaft
ECU	Engine Control Unit
EGO	Exhaust Gas Oxygen
EGR	Exhaust Gas Recirculation
ETK	Emulator Tastkopf (German)
FEM	Finite Element Method
$FFID$	Fast Flame Ionization Detector
HC	Hydro-Carbon
LIF	Laser-Induced Flourescence
MPI	Multi-Point Injection
PFI	Port-Fuel Injection
$RANS$	Reynolds-Averaged Navier-Stokes
RIM	Refractive Index Matching
SI	Spark Ignition
SMD	Sauter Mean Diameter

1. Introduction and Scientific Scope

Cold start is defined as the engine operation directly after activating the starter until closed loop engine control is reached. Since internal combustion engines are not capable of generating an output torque from standstill - apart from the relatively novel direct-start described later on - an electric starter is used to accelerate the engine to a speed-threshold that allows a reliable first combustion. Good start performance has to be guaranteed for different starting conditions like ambient temperature ranges from -30 to +50 °C and ambient pressure levels encountered with different heights above sea level. In addition, engine conditions such as engine block temperature, battery status and fuel characteristics have to be taken into account.

The functionality of the engine control unit (ECU) shall meet these requirements optimally. To this end, data maps are used to determine the operation of actuators like injection nozzles, throttle or spark plugs. These data maps have to be generated in order to cover every possible combination of boundary conditions to obtain an optimal cold start. The primary optimization criterion is robustness followed by repeatability, pollutant emissions and noise. Current technology makes it possible to achieve this by a steadily increasing number of actuating variables. Downfall of this trend is the rising number of experiments to configure the required operating maps. What was once throttle position, fuel mass and spark timing is now extended by injection timing(s), number of injections, fuel mass split and rail pressure. This is further exacerbated by the steadily shortening of product cycles and widening portfolio of OEMs. These circumstances require the aforementioned parameter space to be measured in increasingly short time.

This can be partially fulfilled with automated test benches. Nonetheless, there is a limit to which extend the time for engine conditioning can be reduced. Engine conditioning in this context means to restore the initial condition of the cold start measurement, especially

engine block temperature. These factors combined lead to relatively high effort and therefore high costs of cold start ECU calibration. This is where simulation can play a major role for reducing test bench time which is the focus of this work and is elaborated on in the following sections.

The first chapter outlines the scientific scope of the present work and creates a context to the available literature. After a brief description of the experimental basis in Chapter 2, the developed model for an SI engine during cold start is depicted in Chapter 3. The calibration of the model with experimental data in Chapter 4 complements this. Finally examples for applications of the model are explained in depth in Chapter 5, followed by a conclusion and an outlook.

1.1. Character of SI Engine Cold Start

At the time the cold start is initiated, a start control mechanism is launched by the ECU. This control is open looped, i.e. no direct feedback of process signals takes place. The foremost goal of a cold start strategy is a reliable start, meaning the engine sustains itself without an electrical starter. Other criteria are low starting time durations to meet customer demands and legal requirements concerning pollutant emissions. Several boundary conditions cause this optimization problem to be challenging.

The most severe is the inhibited mixture formation compared to the fully warmed-up engine operation. The main and most obvious reason is the low engine block temperature. Heat flow to the injected fuel is compromised compared to the warmed up case and thus the process of evaporation is slower and selective. A multicomponent fuel as gasoline evaporates in the order of the boiling temperatures of its components. Hence, the high-boiling residue remains as liquid in the cylinder and can form a wall film, as described in detail later, or exit through the exhaust valves as unburnt or partially burnt hydrocarbons (HC).

Another cause for poor evaporation is the supplied fuel pressure during start-up. Operation fuel pressure of direct injection spark ignition engines (DISI) is typically in the range of 40 to 150 bar [49]. At the beginning of the cold start, however, fuel pressure is at ambient pressure level and since the high pressure pump is directly connected to the camshaft, the

pressure built-up occurs simultaneously to the engine run-up. Here, either a longer cranking phase or a lowered fuel pressure for the first injections has to be accepted. According to Gandhi et al. [27] increased fuel pressure leads to a decreased Sauter mean diameter (SMD). An exponential decay of SMD over pressure is observed. An increased SMD, however, results in a reduced total surface area which in turn causes evaporation to take place slower. This work implies that marginal utility is achieved at a pressure value of about 40...60 bar. If this requirement can not be met by the pressure pump fuel, evaporation is hampered.

The resulting incomplete evaporation necessitates an enrichment of the nominal mixture, i.e. more fuel is injected than would be necessary for a stoichiometric mixture at ideal conditions. Enrichment can be as high as 30 for very low starting temperatures of -30 °C, resulting in fuel injection mass that is 30 times higher than that of a stoichiometric mixture [50]. This enrichment factor is further increased by a safety factor to account for different fuel batches with differing volatilities.

Such unfavorable conditions lead to a fuel wall film on the combustion chamber walls. This has implications on the mixture preparation process and on emissions. A great amount of work was put into solving this problem, e.g. investigations regarding in-cylinder wall wetting that were conducted by Hochgreb [40]. Here, injection timing was varied to determine the influence on piston wetting where the liquid film was measured with Laser-Induced Fluorescence method (LIF), Fig. 1.1. An influence of temperature on piston wetting during stratified operation mode could be observed. Nonetheless, temperature effect is relatively small as film boiling, also known as Leidenfrost effect, offsets the enhanced evaporation conditions with higher temperature.

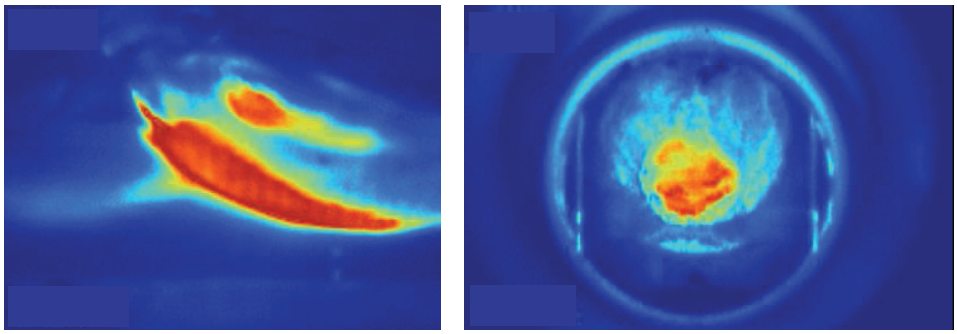

Figure 1.1.: LIF measurements of fuel wall film on piston [40], left picture shows cross section of the piston, right the top view

Stanglmaier et al. [85] furthermore state that condensation of fuel on the cylinder walls can be another source of fuel wall film. As the in-cylinder pressure rises during compression stroke, vapor pressure of certain fuel components can be exceeded particularly at the walls where heat flow reduces gas temperature. While flame passage may lead to evaporation of fuel off the wall film, the influence of the flame passage depends strongly on quench distance and, since walls are cold and heat transfer high during cold start, quench distance is increased. Thus, a wall film remains on the walls until combustion ceases and the liquid fuel evaporates when the pressure falls to levels below the fuel vapor pressure at the current wall film temperature. At this point, however, temperature is too low to oxidize the fuel components which ultimately leads to increased HC emissions during cold start.

Koga [48] compared wall film dynamics of port-fuel injection engines (PFI) with DISI engines at cold start and observed an increase in wall film mass with the DISI concept. The reason is that high-boiling fuel components are stored temporarily in the manifold wall film of the PFI engine. With direct-injection the whole spectrum of fuel components enters the cylinder with the high-boiling components not evaporating and accumulating on the walls. Correct injection timing can mitigate this effect and reduce wall film mass by half. A late injection, at 60° BTDC, minimizes cylinder wetting in this particular engine configuration.

Fuel wall film does not only increase HC emissions but contributes to mixture formation of the subsequent cycles in an a priori unknown amount as shown by Grünefeld et al. [33] and Shayler et al. [82] respectively. Fuel deposited on the surfaces persists through many cycles and feed to the fuel-air mixture that has to be quantified. These prior-cycle effects can therefore influence the equivalence ratio and complicate cold start calibration since cyclic variations known from warmed up engine operation [11] are aggravated.

Suck [88], among others [38],[79], analyzed causes for HC emissions in DISI engines in general. In contrast to PFI engines with crevice volumes and oil films as the main contributor to engine-out HC emissions, DISI engines in stratified mode display different mechanisms, namely lean quenching and fuel wall film, Fig. 1.2. Higher load increases the necessary fuel mass to be injected which induces more wall film in turn. Compared to the total HC and CO emissions during a typical engine test cycle, a high amount is emitted during cold start and warm-up of the engine. This is especially problematic since the catalytic converter is inactive

until light-off temperature is reached, resulting in engine-out emissions not converted but counted towards tail-pipe emissions instead [16], [74]. The storage of HC in the converter due to adsorption could be identified as a mechanism to reduce the tailpipe HC [81]. Despite this, it was also identified as being insufficient for solving the emission problem with standard catalytic converters during start since the storage capacity is inadequate.

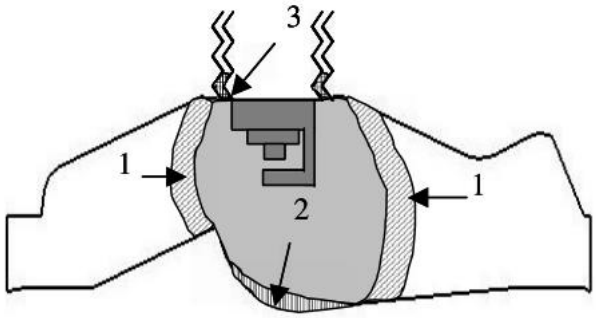

Figure 1.2.: Sources of HC emissions in DISI engines [38], 1 - lean quenching, 2 - wall film, 3 - spark plug crevices

In addition to HC emission, wall films contribute to soot formation as well. Drake et al. [20] analyzed the influence of wall film on pool fires in a DISI engine with swirl and multihole type injectors. Fuel film was measured by Refractive Index Matching (RIM) quantitatively, i.e. area, thickness and, hence, volume. It was observed that late (past 60° ATDC) soot formation resulted from diffusion flames that originate from wall film evaporation during the expansion stroke. As emission of particulates is restricted by introduction of the emission standard Euro 5, soot formation is a major optimization criterion for DISI engines.

Another problem related to fuel wall film is that oil in the cylinder liner is washed down past the piston. This effect is amplified at cold start conditions by an increased blow-by mass flow on the one hand and the increase in injected fuel mass with wall film build-up on the other. Oil-fuel mixture transported to the crankcase is returned only partially via the crankcase breather route and thus leads to increased oil dilution [10],[52]. Oil dilution is to be avoided because of decreasing viscosity with increased fuel ratio and therefore increased wear.

In order to lessen the wall film problem during DISI engine cold start Kufferath et al. [50] described a high pressure stratified start in comparison to the conventional low pressure

homogeneous start. Low pressure start strategy employs an injection timing in the intake stroke with a moderate fuel pressure of about 5 bar which is comparable to a PFI engine. This necessitates an enrichment factor of two to three at starting temperatures of about 20 °C and exponentially rising enrichment with even lower temperatures. The resulting necessary long injection durations lead to over-penetration and wall film build-up. With the high pressure stratified start on the other hand, injection takes place during compression stroke. Injection timing is typically in the range of 75 to 20° BTDC. The elevated temperature level during compression enhances evaporation compared to the intake stroke injection where none or very little heat transfer can occur as the temperature gradient is very low. Another characteristic of this strategy is the placement of the mixture in the vicinity of the spark plug in order to improve the ignition reliability. Enrichment can thus be lowered to reasonable values in the order of one to two for starting temperatures of 20 °C.

Even with the improved start strategy, a major problem with cold start remains to be solved. This is the high variation in mixture formation quality and, hence, combustion quality from one cold start event to another. It is in turn dependent upon operation, i.e. upon boundary conditions and operating parameters during start. The reason for this is the high variability in initial and boundary conditions such as the fuel storage after stopping the engine. At shut-down of the engine by means of injector cut-off, exhaust gas from the last burning cycles is not purged completely, leaving unburnt hydrocarbons in the engine cylinders and manifolds [46]. Furthermore stationary wall film in the cylinder occurs even with DISI engines. It does not evaporate completely during cast-down and is therefore a source for the next start, influencing mixture formation. Another source of variation is the rail pressure, which can not be reproduced reliably leading to different droplet sizes.

These unfavorable conditions at start-up can lead to misfires because of over-lean or over-rich air fuel-mixture. As a result of failed combustions the drop in engine speed is a major issue, particularly, if multiple combustions fail. Then the engine does not start at all or comes to a halt after a short speed flare. Wiemer et al. [95] show a strong influence of enrichment factor and injection timing on reliability of engine cold start. A rising enrichment factor increases reliability with diminishing return but at the same time HC emissions also. Furthermore, indicated mean effective pressure does not increase with enrichment factor when a certain

threshold is exceeded. The end of injection was varied from 90 to 50° BTDC and also showed an influence on reliability. An early injection of 90 °BTDC was followed by a less robust start due to lower in-cylinder temperatures and, therefore, less effective evaporation. The late injection ensured the fuel-air mixture to be located in the vicinity of the spark electrode and increased reliability.

Apart from being characterized by a challenging mixture preparation, the engine start-up is hampered by mechanical problems as well. The two-mass flywheel, which is mounted in increasing numbers on passenger car engines, is constructed in order to decrease oscillations of the output side of the engine for engine speeds from idle speed onwards [73]. This, however, requires resonance frequency to be passed during start. If the engine then has a low number of cylinders or the torque output exhibits high amplitudes, oscillations can become critical as far as the engine being stuck in the resonance frequency range or coming to a complete halt.

Not only the engine operation during cold start poses a challenge but also the measurement of critical signals. Thus, measurement of the equivalence ratio in the exhaust gas is possible but suffers from influence from other factors such as pressure waves. If a cycle-resolved equivalence ratio is to be determined, the EGO-sensor is to be mounted in the exhaust manifold upstream of the turbocharger. Since current EGO-sensors are sensitive to pressure fluctuation this promotes unreliable results. This problem is compounded by exhaust gas dilution, which occurs during the first cycles as residual air is not purged completely. This effect biases the measured equivalence ratio to higher values than actually occurring.

1.2. Scientific Scope

Legal and consumption requirements cause the number of calibration parameters of the ECU functions to increase. Test bench costs in turn play an increasing role in cold start calibration. Engine experiments are costly for stationary engine operation in general and even more so for cold start. The major cause for this is the fact that cold starts, as the name implies, need the engine to be cooled down to ambient conditions which increases necessary test bench time. Backing up the measurements with a simulation tool can lower

the experimental effort. This encompasses the optimization of engine parameters by optimization algorithms and equally further assessment of measurements that lead to greater insight into the process. Other advantages arising from using mathematical models are, firstly that the simulation gives an insight into conditions that are not measured. Secondly certain conditions can be held fix which is often impossible or at least impeded during real experiments because of interacting processes.

Several approaches can be distinguished to model engine behavior. With increasing modeling complexity these are black, gray and white box models. On the lower part of the complexity spectrum, black box models are utilized which model the process by arbitrary equations that have to be fitted carefully to measurement data. As an example polynomial or artificial neural network can be mentioned. Black box models can close voids in an otherwise discrete parameter space with low computational effort guaranteeing computation in real time. They can be set up and calibrated quite easily with common tools such as *MATLAB®* or *Visual-XSel®* due to the low complexity. On the downside, this model category does not provide insights into the process modeled, neither while setting up the model nor while working with it. This is due to the non-physically based modeling approach. Extrapolation does not provide reliable results either with these models.

As a contrast, white box models, e.g. CFD, base on known physical laws and feature spatial discretization. Since only few empirical models are necessary, e.g. turbulence modeling in RANS or boundary layer modeling, relatively low calibration effort is required. However, computational effort is high. They are characterized by a very good insight into the process due to spatial discretization of the modeling domain. This makes white box modeling well suited for preliminary development and scientific research. The main disadvantages of these models are the time-consuming process of mesh-generation as well as the very high computational effort. Thus, white box models are deemed impractical for the use as a tool for ECU calibration in this context. Furthermore, boundary conditions must be spatially and temporarily resolved and also of high quality to achieve sound results. Examples for commercial software used in internal combustion engine development are *CFX FLUENT®*, *STAR-CD®* and *FIRE®*, for free software *OpenFOAM^{TM}*.

As an intermediate approach, gray box models are possible. These have a known struc-

ture based on physical laws with submodels for the underlying processes. Since more (semi-)empirical models are necessary than for the white box model, the number of unknown parameters is higher and therefore model calibration becomes more of an issue. The relative detailed modeling of the governing processes raises the opportunity to gain good insight into the process. This increases the understanding and facilitates skeptical verification of the results. Gray box models are especially suited to assist ECU calibration due the acceptable computational cost and the easy transfer to other engines by means of calibrating the model constants. Boundary conditions have to be temporarily resolved but not spatially. This in turn favors ECU calibration since in most cases matching experiments can not deliver spatially resolved measurements. Several commercial tools are available, such as *BOOST*® or *GT-POWER*®. Since those tools are designed to cover engine operation in general and the option to modify the underlying models is restricted, an approach based on the *Modelica*® simulation language is used.

The following theses can be derived from the statements above:

- Simulation of SI engine cold start is possible with gray box models based on thermodynamic and mechanical modeling approaches.
- Describing the flame propagation in the combustion chamber by means of fractal theory is suitable for the simulation of cold start combustion.
- Optimization of the cold start is possible with these models .
- The engine model enables cycle-resolved estimation of mean effective pressure from high-resolution engine speed measurement during cold start.
- The generic nature of the model can be used for different engines based upon sound calibration of model constants.

1.3. Existing Engine Cold Start Models

The modeling of the SI engine cold start in general is used to support the calibration process and to increase knowledge of the cold start process. Two different modeling approaches can be distinguished with the gray box method in mind: The first uses measurement data to

gain information about quantities that can not be measured directly such as evaporated fuel mass. The second approach simulates the cold start process in order to investigate advantageous parameter combinations. Either the whole start process is simulated using zero-dimensional models with simplified models for fuel evaporation or a certain part of the process is investigated, e.g. at a fixed engine speed, which is typical for more sophisticated models such as spray models.

The work of Grote [34] is an example for the first approach to increase the information gain of measurement data. It introduces a one-dimensional model of the fuel wall film in the intake port of a MPI engine. Heat and mass transfer at the boundary of the wall film is modeled by conservation laws as well as gas and liquid properties of each control volume along the axis of the intake port. It yields reliable results for port injection engines. For modeling a DISI engine, however, it is suitable to a limited extent only because it requires information about the flow field in the combustion chamber, which is limited in zero-dimensional modeling.

Wermuth [94] shows a combined offline and online model to determine the optimal fuel mass to be injected during the start of a port injection engine. Air mass is calculated via an in-cylinder pressure signal. Together with an x-τ-model by Aquino [3],[18] for fuel wall film behavior it can determine the fuel to be injected on a cycle-by-cycle basis. Wermuth, however, states that the empirical x-τ-model is prone to inaccuracy in operation regimes not covered by the calibration of the model. It is used nonetheless, due to the high computational efficiency. Luan [55] describes a similar model for the fuel calibration during cold start that enhances information gain by modeling evaporated and wall film fuel mass. It is then possible to determine the cycle-based fuel to be injected optimally for a given ambient temperature and fuel. The model discriminates between several evaporation mechanisms: evaporation from fuel spray, contribution of hot exhaust backflow, forced convective evaporation and diffusive evaporation of intake port fuel wall film. The approach is also restricted to modeling MPI engines.

As an example for the second model type the work of Kulzer [51] is referred to. Kulzer describes a combined thermodynamical and mechanical model to simulate engine behavior during cold start in order to optimize direct-start capabilities. Direct-start is a cold start

technique that forgoes using a starter and relies on ignition and combustion of a fuel-air mixture from standstill. The aim is to reduce starting duration, noise and emissions. The model itself features thermodynamic control volumes for intake and exhaust manifolds and the individual cylinders with a separation of the mixture zones to model stratified mixture preparation. Fuel evaporation is modeled via a delay between fuel injection and evaporation characterized by a fixed time constant. A quasi-dimensional combustion model provides the heat release and consequently the in-cylinder pressure for further use in the simplified powertrain model.

Liebsch et al. [54] investigate DISI engine cold start by modeling fuel evaporation similar to parcel models used in Diesel engine modeling. The focus is the application of such a model to the calibration of engines using E85[1] fuel. Since ethanol has a higher evaporation enthalpy and a lower vapor pressure than gasoline the realization of a reliable cold start is a more challenging task. The basis of the model is again the zero-dimensional thermodynamic control volume of a DISI engine contributing pressure and temperature to the spray model. The spray model considers primary break-up indirectly by providing a droplet size distribution from measurement data. Evaporation of droplets is then modeled by the well-known D^2-law, which considers heat and mass flow across the droplet boundaries and the resulting reduction in diameter. Furthermore, wall-film on the walls of the cylinder is modeled by describing the fuel-wall interaction. This model is capable of optimizing the cold start strategy concerning fuel enrichment, injection timings and split ratio between two injections. As combustion is not modeled, a criterion of the mixture preparation process like the effective equivalence ratio is used for optimization instead.

1.4. Development Environment

In this work the physical models describing the engine are implemented in *Modelica®* [62], an object-oriented modeling language. It is used in favor of e.g. *MATLAB/SIMULINK®* or *Mathematica®* for several reasons. The first is the aforementioned object-oriented approach where models and submodels are capsuled as classes with attributes and methods rather than functions. Classes can inherit attributes and behavior of other classes and therefore

[1] E85 stands for an ethanol-gasoline mixture with 85 % ethanol used as fuel in SI engines.

code maintenance and reusability is improved. Object behavior is described by differential, algebraic and discrete equations. The user does not need to sort these differential-algebraic equations (DAE) nor is it required to algebraically solve these equations for a specific variable [26]. It is possible to state equations in text-book form, while the algebraic transformation for determining individual variables is done by the simulator instead.

Another important feature is the acausal modeling. Causal modeling as in *MATLAB®* uses a block-oriented modeling style with unidirectional information flow from the inputs to the outputs of the model, which is useful and well accepted for control theory. Acausal modeling on the other hand, relies upon laws of conservation where information flow is bidirectional. As a consequence, direct visibility of inputs and outputs of a system is absent. Instead, individual objects are linked via "connectors" for which a flow direction is not prescribed. This captures behavior of physical systems better and simplifies the modeling process for the user. [65] Furthermore, *Modelica®* supports multi-engineering, i.e. models can consist of components from different domains, like for example combinations of mechanical and thermodynamic models. Several domains are covered already in commercial and non-commercial libraries. The *Modelica Standard Library* contain models for domains like mechanical, electronic and thermal systems.

Due to its availability and maturity, *Dymola®* [2] serves as a simulation environment. Other examples are *SimulationX®*, *MathModelica®* or *OpenModelica*. *Dymola®* comprises of several tools for stating and simulating models. A graphical editor and a text editor is available for describing the mathematical model of the considered physical system as an object-diagram. Individual objects can be stated symbolically in a hierarchy system. On the last layer only, equations describing the physical behavior have to be stated. Algorithms that enable symbolic equation solving and index-reduction for the transformation of the unstructured equation system into a form that can be translated into C-code and compiled are at hand. The model is then saved as *dymosim.exe* that contains both model and integration algorithms like *LSODE* [70] and *DASSL* [15].

2. Engine Measurements

The subsequent chapter elaborates on the experiments carried out in the context of the model development. The first section shows the experimental engine followed by a presentation of the test bench and the measurement equipment used. Thereafter, the specific experiments, which were conducted in order to calibrate the engine model are described.

2.1. Engine

The engine employed for the tests is a four cylinder direct-injection, spark ignition engine. The engine data is presented in Tab. 2.1. It is equipped with a turbo- as well as a supercharger to achieve a high mean effective pressure within the scope of engine downsizing. To provide a sufficient boost pressure the supercharger is engaged at low engine speeds where exhaust gas mass flow rate is too low to operate the turbo-charger effectively. A throttle controls the mass flow trough the supercharger and the turbocharger.

The configuration of the engine comprises two overhead camshafts, where the camshaft of the intake valves adopts a variable phase shift. This way internal EGR and also volumetric efficiency can be controlled directly.

The fuel delivery system comprises a low pressure loop with a delivery pump that supplies fuel with a pressure up to eight bar to the high pressure injection loop. The high pressure pump delivers fuel with a maximum pressure of 150 bar to the fuel-rail with the pressure regulator. Each cylinder is equipped with a high-pressure multi-port injection nozzle, which is mounted inclined under the intake valves.

In order to exploit the advantages of a three-way catalytic converter, engine operation is restrained mainly to stoichiometric conditions. As this necessitates a homogeneous air-fuel

Table 2.1.: Engine data

Parameter	**Unit**	**Value**
Number of cylinders	–	4
Compression ratio	–	9.7
Bore	mm	76.5
Stroke	mm	75.6
Connecting rod length	mm	144
Number of intake valves per cylinder	–	2
Number of exhaust valves per cylinder	–	2
Intake valve diameter	mm	29.5
Exhaust valve diameter	mm	26
Maximum valve lift	mm	9
Intake valve open at 1 mm valve lift	$°ATDC$	21.4
Intake valve close at 1 mm valve lift	$°ABDC$	35.7
Exhaust valve open at 1 mm valve lift	$°BBDC$	24
Exhaust valve close at 1 mm valve lift	$°BTDC$	10

mixture, an early injection in the suction stroke is applied. In addition to the homogeneous mixture preparation other operation modes are used as well: a stratified operation mode with single injection during compression stroke and a split-injection with a single suction-stroke injection and an additional compression-stroke injection. The stratified operation mode with a late injection at high fuel pressure decreases wall film build-up during engine start and thus the necessary enrichment, see Chapter 1.1. A longer time span, which is necessary for rail pressure build-up compared to a low pressure start with suction stroke injection, has to be taken into account. Another operation mode is the split-injection during catalytic

converter heating, which is used to enable a stable combustion with late spark timings. The tendency for engine knock can also be reduced by a similar strategy.
The aforementioned variable mixture formation modes require a compromise on the form of the piston. Wall- and air-guided stratified operation necessitates a distinct bowl form of the piston to enable a redirection of the fuel injected. A bowl on the other hand increases the surface area and subsequently the heat entering the piston material. As homogeneous and stratified injection modes are applied, a shallow piston bowl is used. This limits the lean operation of the engine, which is especially problematic during cold start where stratified mixture formation is hindered.

2.2. Test Bench Setup

Measurement Equipment

The experiments conducted required modifications and additional measurement equipment compared to the production engine configuration. Fig. 2.1 shows the test bench, Fig. 2.2 the schematic setup of the measurement equipment used, see corresponding Tab. 2.2 for explanation of the individual sensors.

NiCr-Ni-thermocouples are equipped for measurement of temperatures in the intake and exhaust ports. To determine surface temperature of the combustion chamber, surface thermocouples are embedded in the cylinder head, see Fig 2.3.

A central measure for the analysis of engine working cycles is the in-cylinder pressure. Therefore water-cooled piezoelectric pressure sensors Kistler 6061B are installed in boreholes in the cylinder head of each cylinder. The pressure sensors have a measurement range of 0-250 bar and a sensitivity of 25 pC/bar. Thermal shock and zero shift is minimized by an active water cooling. Thermal shock is a signal deviation caused by high temperature changes during combustion. The heat penetration leads to thermal stress in the quartz and ultimately to a signal change not based on pressure and, therefore, to be avoided. The pressure sensors are flush mounted to reduce influences on the working cycle itself and to avoid the formation of stationary waves in the bore hole.
Pressures in the intake and exhaust manifold are detected by piezoresistive sensors WIKA

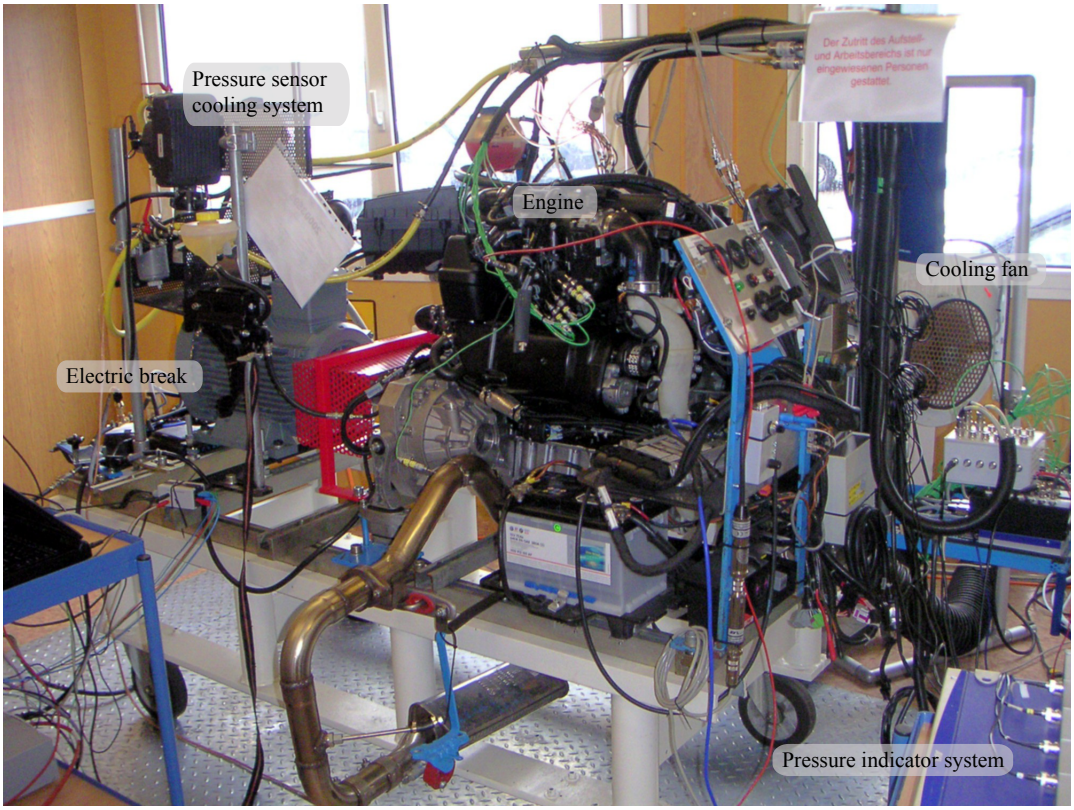

Figure 2.1.: Test bench

S-10 with a measurement range of 0-4 bar.

Engine cold start experiments include the measurement of engine speed. The sensor used is part of the standard engine and consists of a crank shaft mounted wheel with 60 teeth with a single gap two teeth wide (60-2-wheel). A hall effect sensor detects the passage of the individual teeth. The resulting signal is sampled with a frequency of 20 MHz. Since the wheel is divided into 60 segments the frequency of the discrete signals of the hall effect sensor is a direct measure of the engine speed in min^{-1}. Due to a production process that is afflicted with finite tolerances, systematic errors have to be taken into account with speed measurement carried out by such a sensor. With the knowledge about the tooth-error $\Delta\varphi$ - Fig. 2.4 shows the characteristic curve for the 60-2-wheel equipped - the corrected crank shaft speed can be calculated by [86]

$$\dot{\varphi}_{corr} = \frac{d\varphi + \Delta\varphi}{dt + \Delta t} \approx \frac{6° + \Delta\varphi}{dt} = \dot{\varphi}_{meas}\left(1 + \frac{\Delta\varphi}{6°}\right) . \tag{2.1}$$

The gap in the 60-2-wheel is necessary to identify the top dead center of cylinder one. Since

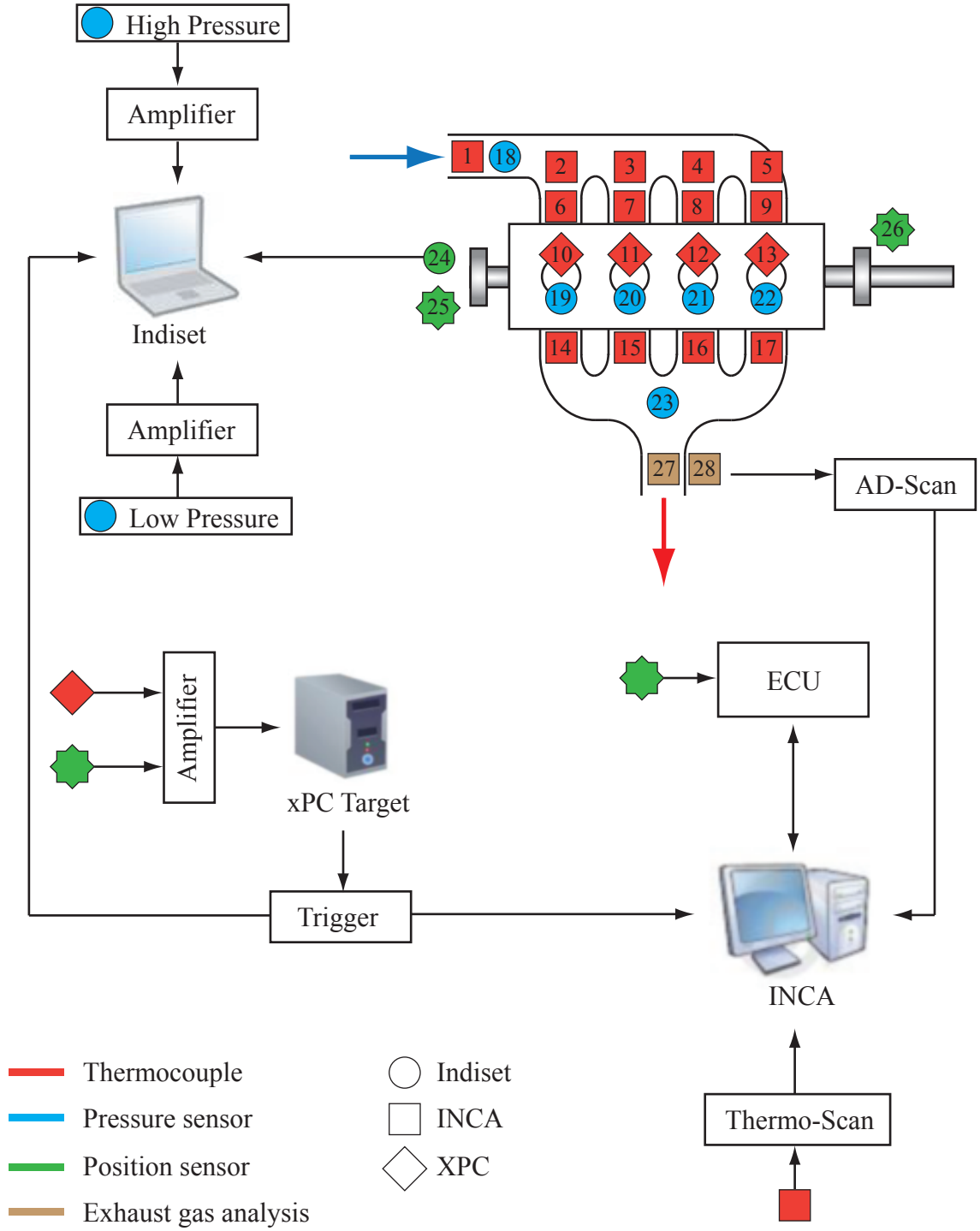

Figure 2.2.: Schematic test bench setup with measuring points and signal processing equipment Indiset, INCA and XPC

Table 2.2.: Sensor positions of the test bench

1	Thermocouple intake manifold
2...5	Thermocouple intake plenums
6...9	Thermocouple at intake valve
10...13	In-cylinder surface thermocouple
14...17	Thermocouple exhaust plenums
18	Pressure sensor intake manifold
19...22	In-cylinder pressure sensor
23	Pressure sensor exhaust manifold
24	Angular position sensor Indiset
25	Camshaft angular position sensor
26	Crank shaft angular position sensor
27	EGO-sensor
28	FFID

the engine is of a four-stroke type, another signal is required to determine the exact stroke. Hence, a phase sensor is equipped on the camshaft.

Exhaust gas analysis is implemented in the form of AFR and HC measurement. Therefore, the standard two-point EGO-sensor is replaced by a wide-band EGO-sensor Bosch LSU 4.2. Furthermore, a Fast Flame Ionization Detector (FFID) of the type Testa FID-123 I/S [29] is installed to quantify hydrocarbons. The FFID is calibrated prior to each start with a gas mixture of nitrogen and propane with a defined propane concentration of 7000 ppm. This gas mixture is chosen to simulate a representative HC composition and concentration in the exhaust gas of a SI engine. The EGO-sensor as well as the FFID are located in the header of the exhaust manifold.

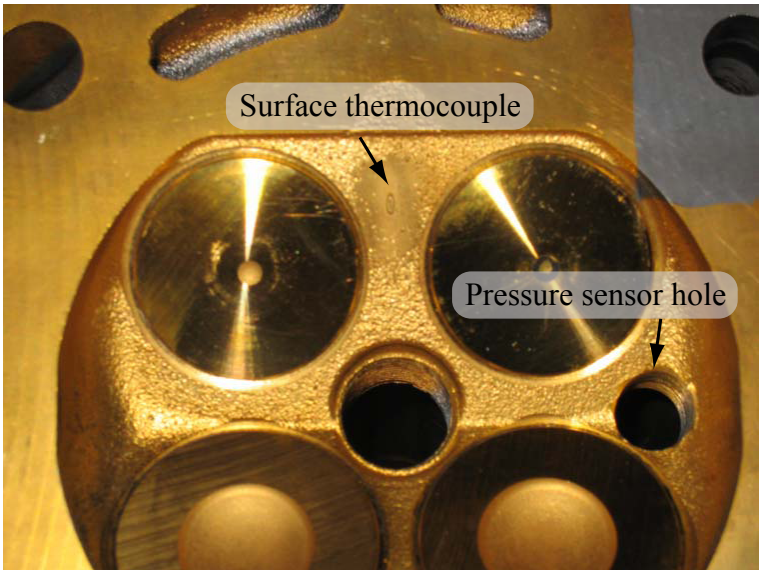

Figure 2.3.: Modified cylinder head with surface thermocouple and bore hole for the pressure sensor

Signal Processing

As apparent from Fig. 2.2, the test-bench periphery consists of the experimental ECU and the three signal processing systems *INCA*®, *Indiset*® and *xPC Target*®. These three systems have to be synchronized via a trigger-signal, which is generated by the *xPC Target* when a motion of the crankshaft is detected and transmitted as a voltage peak to the *INCA* and the *Indiset* systems.

INCA is a measurement and calibration software tool by ETAS [22]. It is capable of measuring ECU signals as well as additional signal inputs via A-D converter (AD-Scan, Thermo-Scan), here the thermocouple signals. Online communication with the ECU is implemented via an ETK[1], which is connected by an interface module ETAS ES590 to the PC-based *INCA*, enabling the direct manipulation of ECU data during the experiment.

The recording of in-cylinder pressures as well as pressures of the intake and exhaust system is realized by the *Indiset* indicating system by AVL [4]. The crank-angle based signals are detected with a resolution of 0.5° which is supplied by the position sensor applied to the crankshaft. *Indiset* then processes the signals from the piezoelectric pressure sensors. Since piezoelectric sensors respond only to changes in pressure applied to the surface, an offset

[1] *E*mulator-*T*ast*k*opf (German) - ECU communication interface.

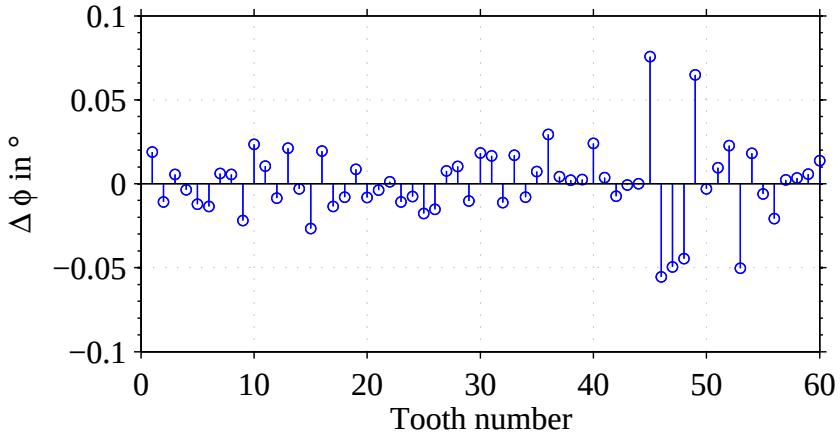

Figure 2.4.: Tooth error of the 60-2 wheel

correction has to be realized. In this case the pressure value is adjusted to the value of the intake manifold pressure measured during open intake valves supplied by the piezoresistive sensor in the intake manifold.

The third signal processing device is the *xPC Target*. This system is a host-target environment by The MathWorks [58] for real-time simulation and measurement. The *xPC Target* is installed on a PC and operated via *MATLAB*. Measurement data is uploaded directly into the *MATLAB* workspace. The signals of the position sensor of crank- and camshaft are transmitted to the *xPC* system and are sampled with a frequency of 20 MHz. Based on this data the engine speed is calculated after each cold start experiment. As in-cylinder wall temperatures are highly fluctuating, the detection and processing is executed by this system as well.

2.3. Experiments

A number of different experiments were carried out, which can be divided into two categories. Fully warmed up engine operation for calibration of the various sub-models as described in Chapter 4. Examples are stationary operation points for the calibration of the combustion and the loss model as well as instationary experiments in order to calibrate the gas exchange model. Additionally, cold starts were conducted with different parameter settings to establish a data base for optimization in regard to start robustness, fast engine speed-up and HC emissions. Engine parameters to be varied were: spark timing φ_{ign} = 35...-5° BTDC, end

of injection $\varphi_{eoi} = 30...82°$ BTDC, enrichment factor $F_{fuel} = 1.15...3.00$, nominal air mass flow 12.5...17.2 kg/h and start temperatures 7 and 20 °C respectively.

Fig. 2.5 shows the in-cylinder pressures, engine speed and HC emission during a reference cold start.

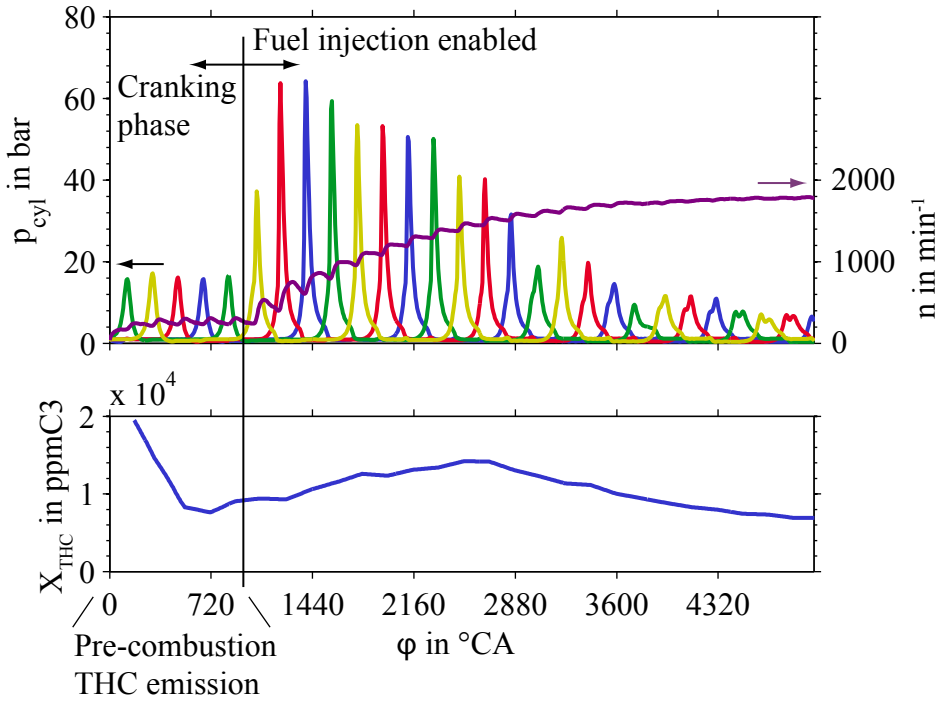

Figure 2.5.: Measurement data of a typical engine start

During cranking the engine is powered by the starter with a relatively low engine speed of 250 min^{-1} corresponding to the power output of the motor. Attached to the camshaft is the high pressure fuel pump, which builds up rail pressure to a nominal value for the fuel injection to start. Also, during cranking the ECU has to synchronize with the rotation of the crankshaft. This means a definite position information has to be identified, which is necessary to make a precise timing of operation parameters possible, e.g. injection and spark timing.

Obvious from the lower part of Fig. 2.5 is an emission of HC before the first injection has taken place. The cause for this is the remaining fuel from the previous engine-run that is

now flushed by the fresh air mass flow aspirated by the engine. Additionally injector leakage during standstill cause HC to accumulate in the combustion chamber. This manifests in HC emissions that can not be influenced by the choice of parameter values of the current engine start and was hence omitted for the analysis of experiments.

When the rail pressure threshold is reached, fuel injection is enabled and, if a combustible mixtures forms, combustion takes place with the engine running up in turn. A maximum in-cylinder pressure of 60 to 65 bar is possible for the compression ratio of the engine during the first combustion as intake pressure is at ambient level.

Based on the experimental data, an engine model capable of simulating the cold start at different boundary conditions with any desired values for the ECU parameters is to be formulated. This shall be the content of the following chapter with the description of the compound thermodynamical-mechanical model.

3. Model Description

This chapter provides a description of the coupled thermodynamic-mechanical model of a direct injection spark ignition engine for the simulation of the cold start. It starts off with an outline of the architecture of the engine model. Afterwards the individual submodels are discussed.

3.1. Architecture

Due to the object-oriented method applied, the engine model is arranged very similarly to a real engine. It consists of the intake and exhaust manifolds, the engine block with the individual cylinders, camshafts and crankshaft.

By means of the complete gas exchange model, which is composed of the intake manifold with a throttle plate and the intake valves, the aspirated fresh air is determined. Combined with the residual gas from the preceding cycle, supposing there is any, and the fuel injected, the complete charge can be estimated. With this information the coupled ignition delay and fractal combustion model can then determine the burnt gas mass fraction and hence the heat release from chemical reactions. This in turn enables the calculation of pressure and temperatures in the combustion chamber and therefore the torque at the crank of each cylinder. The speed of the engine run-up can then be obtained by the combined torques of the individual cylinders, starter and friction torque and momentum of inertia.

The model is implemented in *Dymola®* which uses the *Modelica®* modeling language and bases on the *SIMPLECAR* package by Tiller [90]. The hierarchy of the complete engine model is shown in Fig. 3.1.
The individual `Testbench` contains the `EngineSetup` and the `EngineRun` information. The object `EngineRun` is used to specify engine input parameters. `EngineSetup` provides the

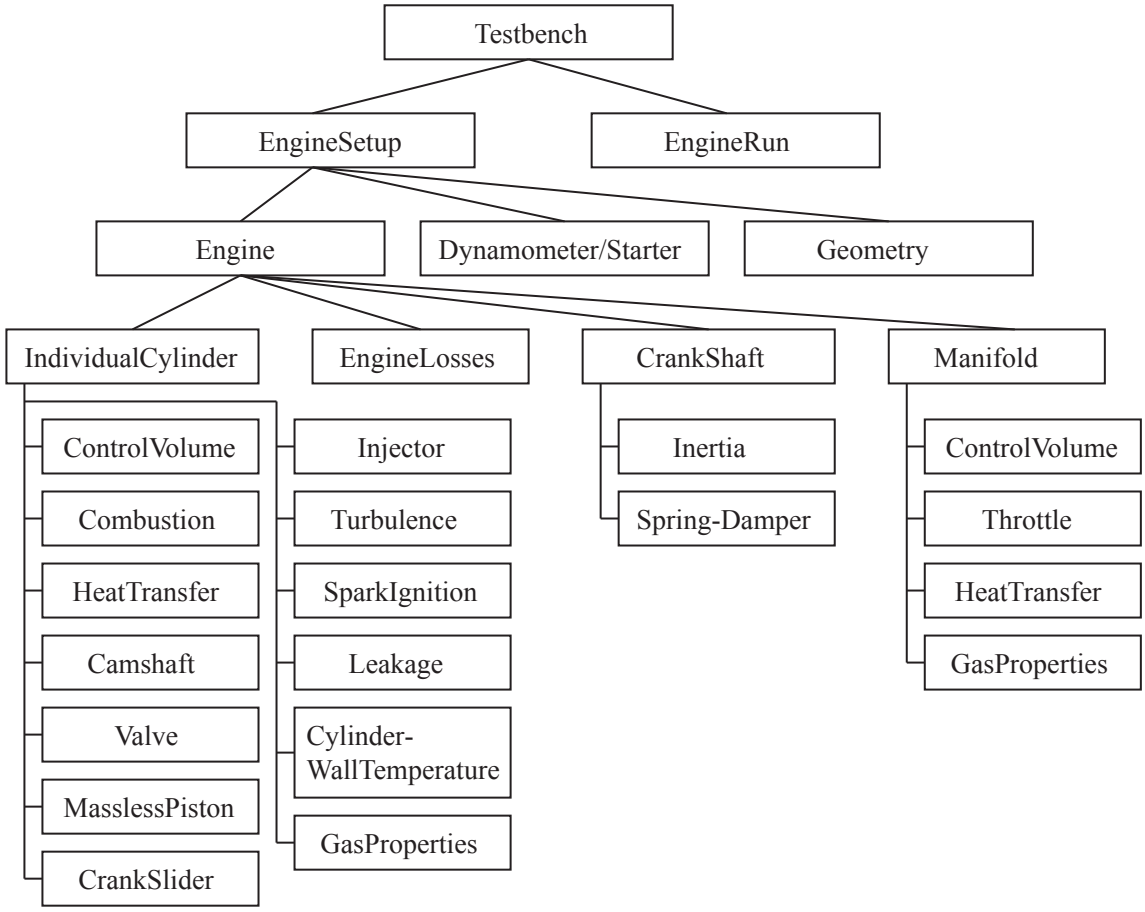

Figure 3.1.: Hierarchy of the engine model

`Geometry` and whether a `Dynamometer` or a `Starter` is installed. The `Engine` composes intake and exhaust `Manifolds`, a `Crankshaft`, an arbitrary number of `IndividualCylinders` and the `EngineLosses` model. An individual cylinder, Fig. 3.2, consists of submodels such as a `ControlVolume`, an `Injector`, a `SparkIgnition`, a `Combustion` model including a `Turbulence` as well as an `IgnitionDelay` submodel. Furthermore, this comprises `HeatTransfer` to and from the walls, a `Leakage` and a `CrankSlider` model as evident from Fig. 3.1. Further details are shown in the Appendix. Information about the engine-run are supplied via a bus connector very similar to the information transfer of a real engine concept. The engine-run information contains ambient temperature and pressure, throttle position, spark timing, phase shift of the intake camshaft, relative equivalence ratio, start of injection and - dependent on application - engine speed or starter torque.

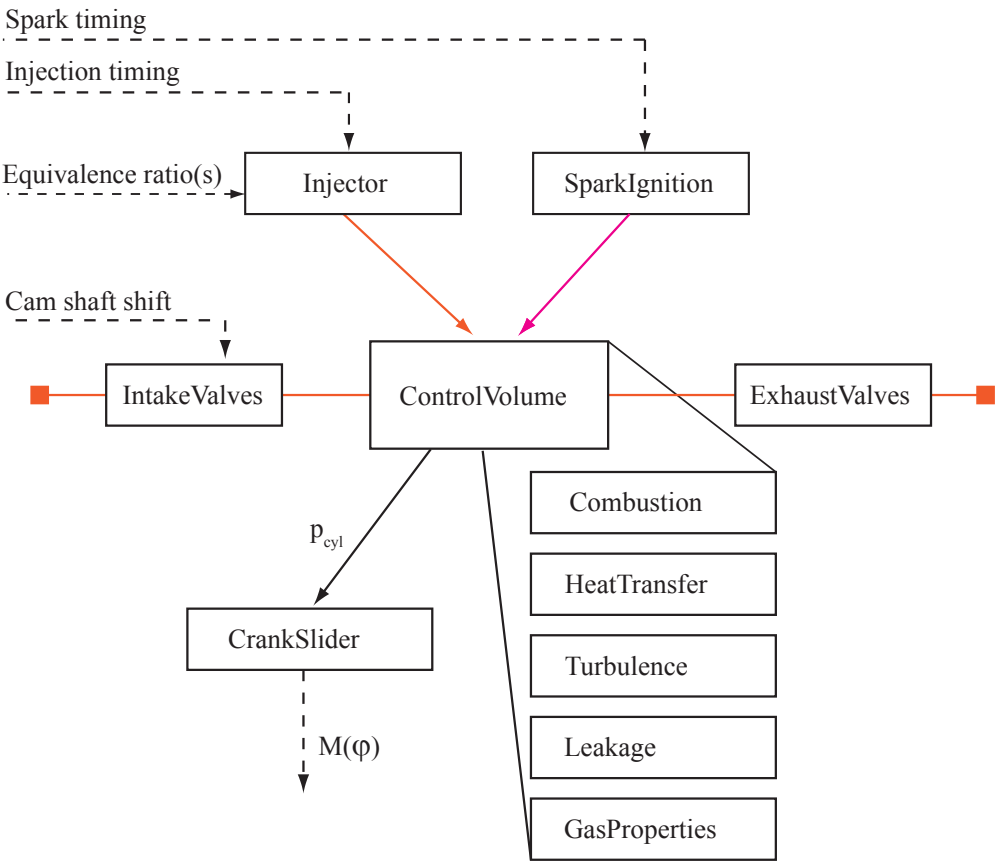

Figure 3.2.: Model scheme of an individual cylinder with input parameters and major output parameters shown with dotted lines. Connectors to adjacent control volumes are depicted as orange squares.

3.2. Control Volumes

Modeling physical systems with the aforementioned gray box approach requires balancing state variables, in the case of a thermodynamic system this means balancing mass and energy. Momentum balance is not accounted for in this case because pressure is assumed to be constant throughout the control volume for every instant of time. In the following all control volumes are modeled as open systems. A closed system represents a special case, e.g. for the combustion chamber for closed valves and an ignored leakage mass flow. The elements where mass flows cross the boundaries are modeled as orifices.

Mass Balance

As mentioned, the mass balance is required for determining the masses within the control volume. The general form of the total mass balance

$$\frac{dm}{dt} = \sum_{\forall k} \dot{m}_k \tag{3.1}$$

expresses that incoming and outgoing mass flows constitute the enclosed mass in the control volume and that neither sources nor sinks exist for the total mass.

In the case of chemical reactions, here primarily the combustion, a species balance is required to account for conversion of air and fuel into burnt gas. This is implemented in terms of a basic species balance for the four lumped components air, fuel, burnt gas and residual gas from the preceding cycle.

Energy Balance

Besides mass balance, a balance of energy is required to obtain information about the internal energy of the considered system. To this end, the first law of thermodynamics can be written for an open system as

$$\frac{dU}{dt} + \frac{dE_{ext}}{dt} = \sum_{\forall i} \dot{Q}_i + \sum_{\forall j} \dot{W}_j + \sum_{\forall k} \dot{H}_k \; + \dot{H}_R \; . \tag{3.2}$$

- dU/dt denotes the change in internal energy of the gas mixture of the control volume and is supplied as a function of temperature, pressure and composition by the caloric equation of state.
- dE_{ext}/dt is the time derivative of all external energies, i.e. kinetic and potential energies of the system in its surrounding and is not considered any further.
- $\sum_{\forall i} \dot{Q}_i$ is the sum of all heat flows crossing the systems boundaries.
- $\sum_{\forall j} \dot{W}_j$ is the sum of all work done to or by the system. The relevant work in the context of internal engine combustion is the work done by the moving boundary constituted by the moving piston: $\dot{W}_V = -p\ \dot{V}$. The volume time derivative $\dot{V}$ is

calculated directly from the position variant geometry of the combustion chamber.

- $\sum_{\forall k} \dot{H}_k$ is the sum of all enthalpy flows tied to the mass flows in and out of the system through its orifices, where enthalpy can be expressed in terms of internal energy and the product of pressure and volume $h = u + p\,v$. Mass flows crossing the boundaries of the system are obtained from the respective orifice model depending on the actual pressure differences across these orifices.

- $\dot{H}_R$ describes the contribution of chemical reactions. It shall be named $\dot{Q}_b$ hereafter to comply with the nomenclature used in engine design and simulation.

Equations of State

The thermodynamic behavior of a gas mixture can be specified by the fundamental equations of its individual components. It is possible to derive the three equations of state for an ideal gas from the molar Gibbs function. A deduction of these can be found in Baehr [5].

The thermal equation of state for an ideal gas can then be written in component form

$$p_i\,V = m_i\,R_i\,T. \tag{3.3}$$

It links pressure and temperature for a given mass and volume and is used here as a functional correlation for $T = f(p)$. R_i denotes the specific gas constant and m_i the mass of each component. The ideal gas assumption is exact only for $p \to 0$. This leads to errors when using the following equations of state for $p > 0$.

To take real gas effects such as van der Waals forces, dissociation of molecules and compressibility of the gas at high pressures into account[1] a compressibility factor Z can be incorporated

$$p_i\,V = Z\,m_i\,R_i\,T\,. \tag{3.4}$$

Fig. 3.3 shows the compressibility factor of air determined by REFPROP [53] for the pressure range of interest. Up to a pressure of about 60 bar and temperatures above 300 K a maximum deviation to the ideal gas model of 2 % can be identified. This error is tolerable compared to

[1] Gases in a combustion engine are far from the critical point or from a phase change region in general and at thus high pressures are to be considered only.

the effort necessary implementing a real gas model. Therefore, the real gas approach shall not be pursued further and the ideal gas approach applied instead.

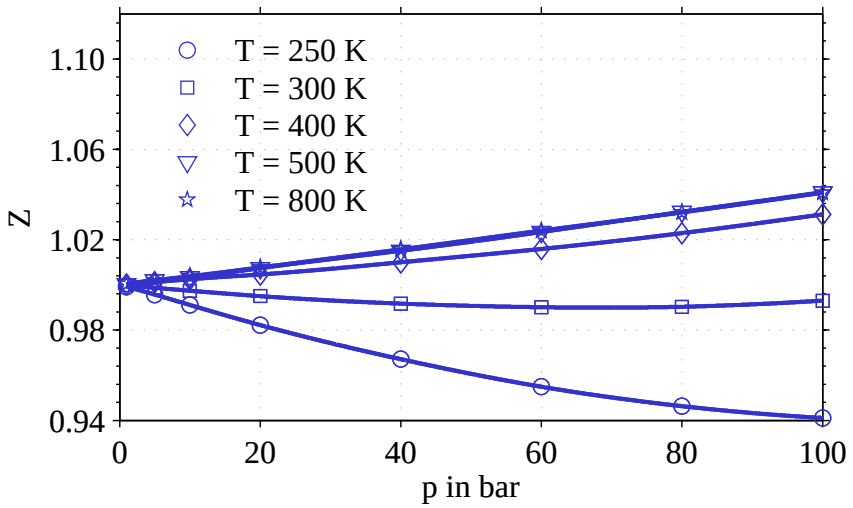

Figure 3.3.: Compressibility factor Z of air [53]

Furthermore the caloric equations of state

$$du = c_V(T,p)\ dT \qquad\qquad dh = c_p(T,p)\ dT \tag{3.5}$$

specify the change in internal energy u respectively enthalpy h in accordance to temperature change. c_V and c_p denote the specific heat capacities of the gas at constant volume and pressure and can be calculated for a mixture by

$$c_{V,mix} = \sum_{\forall k} Y_k\ c_{V,k} \qquad\qquad c_{p,mix} = \sum_{\forall k} Y_k\ c_{p,k} \tag{3.6}$$

Entropy is not a focus of this work and the entropic equation of state is thus not presented here.

3.2.1. Intake and Exhaust Manifold

Gas flow into and out of the cylinder is modeled according to the filling and emptying method i.e. describing a thermodynamic system as a single volume where mass and energy flows can occur across predefined boundaries. [37]

The following assumptions and simplifications shall be valid:

- *Pressure and temperature is uniform in the control volume.* This assumption is legitimate as engine speed is low during starting, which results in low velocities in the intake manifold. Therefore traveling pressure waves, the so-called gas dynamics, can be neglected.
- $p\,\dot{V} = 0$ as for the rigid walls of the intake and exhaust plenums.
- *Chemical reactions are neglected in the plenums.*

With one inflow and one outflow orifice, Eq. (3.1) becomes

$$\frac{dm}{dt} = \dot{m}_{in} - \dot{m}_{out} \tag{3.7}$$

and Eq. (3.2)

$$\frac{dU}{dt} = \dot{Q}_W + h_{in}\dot{m}_{in} - h_{out}\dot{m}_{out}\ . \tag{3.8}$$

3.2.2. Combustion Chamber

Like the aforementioned plenums the cylinder volume is also modeled as an open system as well, see Fig. 3.4. However, mixture formation and combustion make the process at hand more complex.

In modeling terms there is a differentiation between homogeneous and stratified mode. Homogeneous mode stands for an early injection during intake stroke, which results in a good mixture preparation in stationary engine operation. Stratified mode results from an injection in the compression stroke. The fuel does not mix completely with the present air but ideally forms a relatively rich mixture in the vicinity of the spark plug. Therefore, in stationary engine operation this mode can be used to reduce fuel consumption. However, a Denox catalytic converter[1] for exhaust gas aftertreatment is necessary. In engine cold start

[1] Denox catalytic converter for SI engines traps NO_x during stoichiometric or lean operation and reduces it during phases of rich operation.

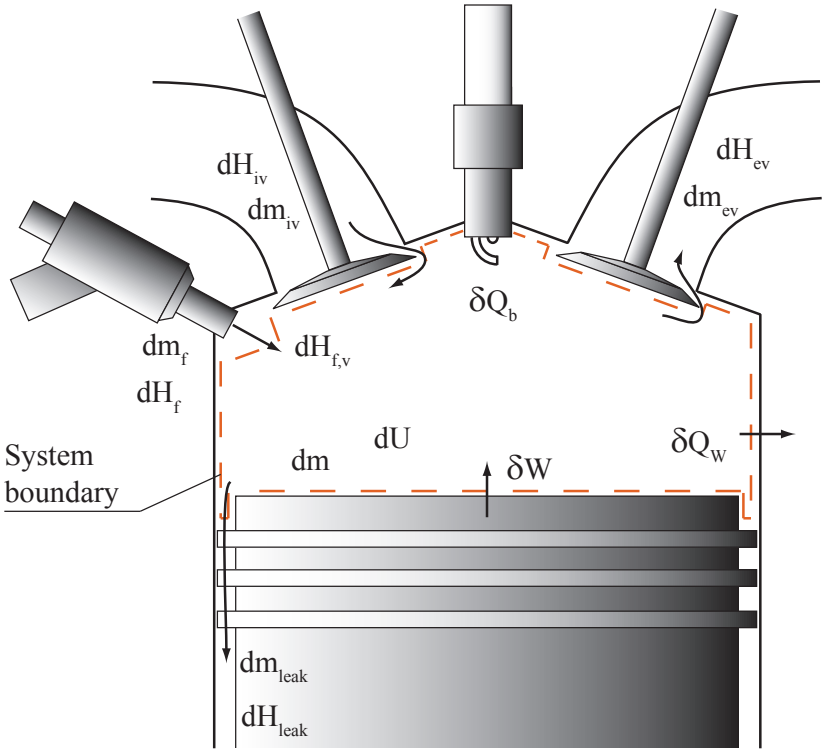

Figure 3.4.: Combustion chamber with system boundaries

operation it has an advantage over early injection in the reduction of required enrichment and therefore in HC emissions as explained in Sec. 1.1.

As shown in Fig. 3.5, modeling mixture formation in stratified mode is achieved by dividing the control volume into two mixture zones as proposed in [51]. With the start of injection, two homogeneous thermodynamic systems are assumed in the control volume - two mixture zones. The zones are uniform in temperature and pressure and identical in both state variables leaving one thermal equation of state for both zones. The differences are the respective volumes and compositions. The mixture zone contains air, fuel and residual gas, whereas the second zone is filled with residual gas and air only.

This approach is implemented by dividing the complete air mass into air mass of the mixture zone, $m_{a,strat}$, and air mass of the surrounding, $m_{a,\infty}$, which does not enter combustion

$$m_a = m_{a,strat} + m_{a,\infty} \; . \tag{3.9}$$

The air mass $m_{a,\infty}$ in the surrounding of the mixture zone can be determined by supplying a global equivalence ratio λ that is lower than the equivalence ratio λ_{mix} of the local air-fuel mixture

$$m_{a,\infty} = m_a \frac{\lambda}{\lambda_{mix}} . \tag{3.10}$$

With these two equations the model determines the two unknowns $m_{a,\infty}$ and $m_{a,strat}$ by supplying the air mass trapped in the cylinder and additionally the global and local equivalence ratios. This can be used as an interface for a spray model.

The quasi-dimensional approach necessitates the assumption that $m_{a,strat}$ *is the only air to be burnt.* The stratification leads to a lowered fuel mass compared to the homogeneous operation and a lowered burn time due to the air-fuel mixture being concentrated at the spark plug.

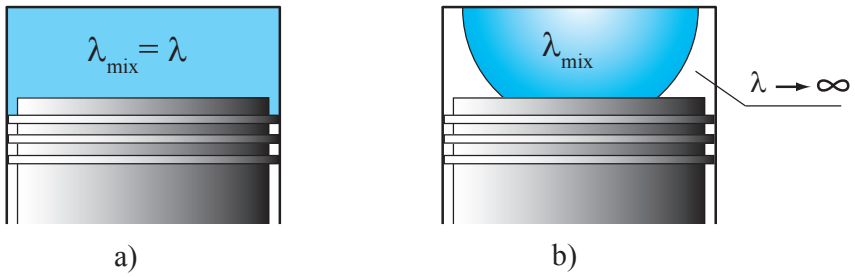

Figure 3.5.: Scheme of a) homogeneous and b) stratified charge - air-fuel mixture depicted as shaded areas

For modeling the combustion process there is another partitioning of the mixture zone into burnt and unburnt gases as depicted in Fig. 3.6. This is known as two-zone analysis in literature [8], [47]. Each zone is described by its own thermal equation of state, whereas only one energy balance equation is stated for the whole cylinder volume. The individual temperatures are calculated by the polytropic correlation of the unburnt zone and the thermal equation of state of the burnt zone.

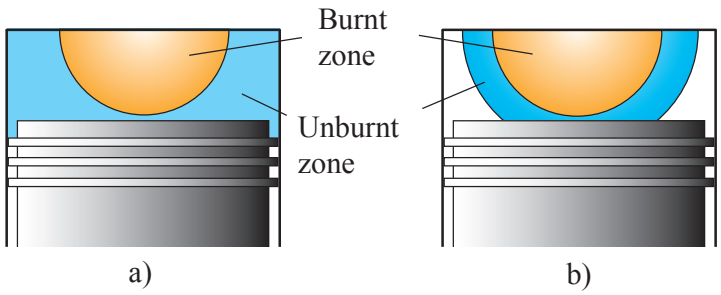

Figure 3.6.: Scheme of unburnt and burnt zone for a) homogeneous and b) stratified charge mode

Further assumptions for the combustion chamber model are:

- *Calculation of heat transfer from gas to the walls can be modeled holistically for burnt and unburnt zone* because the heat transfer model by Bargende [8] takes temperatures of unburnt and burnt zones into account respectively.
- *There is no post-oxidation after the flame front has passed the complete volume of the combustion chamber or if the combustion is not complete when exhaust valve opens.* Since modeling unburnt fuel and carbon monoxide shall not be considered, post-oxidation can be neglected.

As indicated in Fig. 3.4, mass balance for the combustion chamber can be described as follows

$$\frac{dm}{dt} = \dot{m}_{iv} + \dot{m}_{ev} + \dot{m}_{inj} + \dot{m}_{leak} \tag{3.11}$$

where

- $\dot{m}_{iv}$ and $\dot{m}_{ev}$ are the mass flows across the inlet and exhaust valve respectively,
- $\dot{m}_{inj}$ is the fuel mass flow through the injector and
- $\dot{m}_{leak}$ is the leakage mass flow across the piston rings.

Gas mass inside the combustion chamber consists of various components as described above

$$m = m_a + m_f + m_b + m_{EGR} + m_{crev} \tag{3.12}$$

where m_a is the air mass, m_f fuel mass, m_{EGR} mass of residual gas, m_b burnt mass and m_{crev} mass trapped in the crevices of the combustion chamber.
In this context the equivalence ratio is defined as

$$\Phi = \frac{m_f \cdot (A/F)_s}{m_a} \tag{3.13}$$

with $(A/F)_s$ as the stoichiometric equivalence ratio, which has to be measured for the specific fuel used. The relative equivalence ratio is then

$$\lambda = \frac{1}{\Phi}. \tag{3.14}$$

Another characteristic often used is the volumetric efficiency

$$\lambda_V = \frac{m_{a,ivc}}{m_{a,theor}} \tag{3.15}$$

with $m_{a,ivc}$ as the air mass trapped in the cylinder volume at intake valve closed and the theoretical air mass $m_{a,theor}$ at norm conditions $p_{norm} = 1013$ mbar and $T_{norm} = 273$ K

$$m_{a,theor} = \frac{p_{norm}\, V_d}{R_{air}\, T_{norm}} \tag{3.16}$$

where V_d denotes the displaced volume.

Change in internal energy is given by the energy balance

$$\frac{dU}{dt} = \dot{Q}_W - p\frac{dV}{dt} + \dot{H}_{iv} + \dot{H}_{ev} + \dot{H}_{leak} + \dot{H}_f - \dot{H}_{f,v} + \dot{Q}_b \tag{3.17}$$

with

- $\dot{Q}_W$ as the heat transfer across the combustion chamber walls,
- $-p\frac{dV}{dt}$ as the work done due to change in volume,
- $\dot{H}_{iv}$ and $\dot{H}_{ev}$ as the enthalpy flows due to mass flows across the inlet and exhaust valves respectively,
- $\dot{H}_{leak}$ as the enthalpy flow tied to leakage mass flow,
- $\dot{H}_f$ as the enthalpy flow of fuel through the injector,

- $\dot{H}_{f,v}$ as the change in enthalpy caused by vaporization of fuel in the combustion chamber, $\dot{H}_{f,v}$ has to be accounted for in the combustion chamber in the case of a direct injection engine. For an indirect injection engine $\dot{H}_{f,v}$ is relevant in the intake manifold.

- $\dot{Q}_b$ as the release of reaction enthalpy during combustion, which can be determined by quantifying fuel mass conversion and the lower heating value of the fuel.

Internal energy is the sum of internal energies of the individual components

$$U = m_a\, u_a + m_f\, u_f + m_{EGR}\, u_{EGR} + m_b\, u_b + m_{crev}\, u_{crev}\ . \tag{3.18}$$

The caloric equation of state, Eq. (3.5), yields h_k and u_k respectively.

Mass and energy balance are necessary for the calculation of pressure in the control volume. Of particular interest for calculation of gas properties and modeling heat transfer are furthermore temperatures in the burnt and unburnt zones respectively.

The temperature of the unburnt zone is obtained by correlating pressures and temperature for a polytropic change of state

$$T_u = T_{ign} \left(\frac{p}{p_{ign}} \right)^{\frac{n-1}{n}} \tag{3.19}$$

with T_{ign} and p_{ign} temperature and pressure at the point of spark ignition and n as the polytropic index of the expansion process, set to 1.25. The choice of n is differing from common practice for SI engines with a value of 1.32 [68]. The reason is that due to low engine speeds during start wall heat transfer and leakage are increased which result in a lower polytropic index compared to stationary measurements with a heated up engine and higher engine speeds.

The thermal equation of state then yields the temperature for the burnt zone

$$p\, V_b = m_b\, R_b\, T_b \tag{3.20}$$

where V_b is calculated by the following formulas

$$V = V_b + V_u + V_{crev} \tag{3.21}$$

and

$$p\, V_u = m_u\, R_u\, T_u\ . \tag{3.22}$$

Here m_u denotes the unburnt mass and consists of m_a, m_f and m_{EGR}.

The position dependent cylinder volume V is given by

$$V(\varphi) = V_c + \frac{\pi}{4} B^2 s_P(\varphi) \tag{3.23}$$

with V_c as the volume at top dead center, B bore and $s_P(\varphi)$ piston position.

Crevices

The combustion chamber is connected to several small volumes such as the piston top land clearance, the clearance between the rings, spark plug thread clearances and the clearance between the injector and its hole. These crevices have a substantial impact on engine performance in stationary operation [37]. In cold start conditions, however, this is further aggravated by low wall temperatures and an increased crevice volume [77]. Mass is compressed into these clearances during pressure rise and cooled down to or near to wall temperature due to a high surface-to-volume ratio.

This, in effect, leads to a lowered pressure and temperature at the end of compression and thus decreased mean effective pressure. Low wall temperatures during cold starting result in a higher crevice mass-ratio compared to the stationary operation with high wall temperature and therefore make it an effect not to be neglected.

These crevice effects can be modeled by mass flow into and out of the crevice volumes with temperature in the crevice volume at wall temperature level as shown in Rao et al. [71]. Fig. 3.7 depicts the model approach where the mass in the crevices increase during compression stroke and decreases as pressure falls during expansion.

Assumptions for modeling crevice effects on pressure and temperature are:

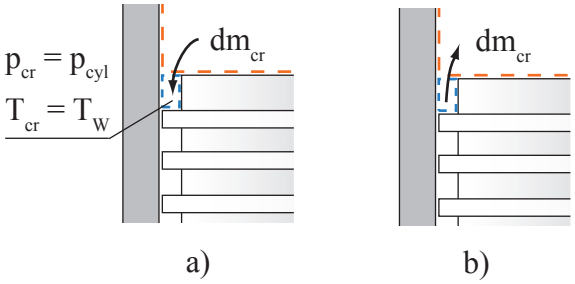

Figure 3.7.: Compression of gas into crevices during a) pressure rise and b) release during expansion

- *All crevice volumes are lumped into a single crevice control volume, which is constant for a given engine.* There is no time dependency since the majority of crevices is located at the engine head and at the piston rings which are not subject to movement by the piston. A thermal expansion of the engine parts, which would influence the crevice volume, is neglected. Its influence is small compared to temperature effects on the gas.

- *Mass trapped in the crevices is composed of air and residual gas only.* This is valid for stratified mode where fuel is supposed to be located in the center of the cylinder. Even if mixture is homogeneous, errors in pressure estimation are minimal because oxidation processes in the crevice volumes are frozen due to low temperatures.

- *Pressures in crevices and in the cylinder are assumed to be identical at all instants.* The area the mass flow has to pass, is large compared to the volumes involved. Thus, influence of momentum exchange is low.

According to [71], crevice volume can be estimated by

$$\frac{V_{crev}}{V_d} = \frac{C_{crev}}{B} \tag{3.24}$$

where C_{crev} is a dimensional constant with a value of 0.3 mm [71], B as the cylinder bore and V_d as the displacement volume.

The thermal equation of state for the crevices volume

$$p\, V_{crev} = m_{crev}\, R_{cr}\, T_W \tag{3.25}$$

finally yields m_{crev} at any instant during a cycle.

3.3. Restrictions

Fluid movement is accompanied by viscous friction and dissipation causing a characteristic pressure drop. This effect is intensified across restrictions in internal combustion engines. To some extent these pressure drops are intended, e.g. for the throttle plate, which regulates mass flow into the cylinder for conventional systems. Often, however, they are not intended and equally unavoidable, e.g. for leakage across piston rings or undesired pressure loss across an air filter.

Modeling these restrictions is possible by inserting restriction objects between control volumes. The following assumptions are valid here [12], [31], [68]:

- *The gas behaves like a Newtonian fluid*, i.e. the shearing force per unit area is proportional to the negative velocity gradient.
- *The flow through the restriction shall be axis-symmetrical and the profile of the inlet velocity shall be uniform.* A one-dimensional model of the flow can thus be formulated. This owes to the limitations of the general modeling approach as stated in Chapter 1, and can be overcome by two- or three-dimensional modeling only.
- *Viscous dissipation and non-uniform velocity profile is lumped into the discharge coefficient C_d.* This is the logical consequence of the above statement. C_d accounts for the contraction of the flow as shown in Fig. 3.8 for a given geometry. It is in the range of 0 to 1 with a lower value characterizing an increased contraction and therefore lowered mass flow at a given pressure drop.

The instantaneous mass flow rate $\dot{m}$ through a restriction can then be modeled by

$$\dot{m} = C_d \, \dot{m}_{is}$$

with

$$\dot{m}_{is} = \rho \, A \, u_{is} \tag{3.26}$$

with the density ρ, the cross-sectional area A and the velocity u_{is}.
Equation of Saint-Vernant states that the isentropic velocity u_{is} for a flow in a converging

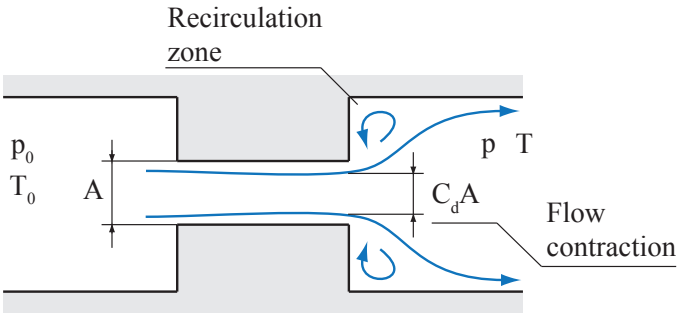

Figure 3.8.: One-dimensional flow through a restriction

nozzle emptying into a large volume can be determined by

$$u_{is} = \sqrt{\frac{2\,p_0}{\rho_0}}\,u \tag{3.27}$$

where the velocity function u is described as

$$u = \sqrt{\frac{\kappa}{\kappa-1}\left[1-\left(\frac{p}{p_0}\right)^{(\kappa-1)/\kappa}\right]}\,. \tag{3.28}$$

Apparently, to generate a positive flow, the pressure gradient must suffice $p/p_0 < 1$. Analogue, reverse flow occurs when $p/p_0 > 1$. κ is the isentropic exponent for the gas mixture in question with $\kappa = c_p/c_V$ for an ideal gas.
Eq. (3.26) can then be written as

$$\dot{m} = C_d\,A\,\sqrt{2\,p_0\,\rho_0}\,\psi \tag{3.29}$$

with ψ as the flow equation

$$\psi = \sqrt{\frac{\kappa}{\kappa-1}\left[\left(\frac{p}{p_0}\right)^{2/\kappa}-\left(\frac{p}{p_0}\right)^{(\kappa+1)/\kappa}\right]}\,. \tag{3.30}$$

As velocity does not exceed the speed of sound, there is a critical pressure ratio where choked flow occurs

$$\frac{p_{cr}}{p_0} = \left(\frac{2}{\kappa+1}\right)^{\kappa/(\kappa-1)}\,. \tag{3.31}$$

The flow equation for choked flow reaches a maximum of

$$\psi_{max} = \sqrt{\frac{\kappa}{\kappa+1}} \left(\frac{2}{\kappa+1} \right)^{1/(\kappa-1)} . \tag{3.32}$$

In internal combustion engines critical pressure ratios particularly arise at the exhaust valves.

With this information, mass flow across restrictions can be determined with information about pressures up- and downstream of the restriction if geometrical area A and discharge coefficient C_d are known. The calculation of these two properties for the relevant restrictions are outlined in the following subsections.

3.3.1. Throttle

Since torque output of SI engines in homogeneous mode is regulated via volumetric efficiency and spark timing, the function of the throttle plate is to adjust air mass flow into the cylinder to achieve torque regulation.

Cross sectional area of the throttle plate is given by

$$A_{th} = \frac{\pi}{4} D_{th}^2 \tag{3.33}$$

where D_{th} is the throttle diameter. Discharge coefficient is [90]

$$C_d = sin^2 \left(\alpha_{th} \frac{\pi}{180^\circ} \right) + C_{d,offset}. \tag{3.34}$$

The offset $C_{d,offset}$ is introduced to account for the leakage mass flow when the throttle plate is closed.

3.3.2. Valves

Engine poppet valves function is to enclose the combustion chamber during compression and combustion and to unblock the path from the plenums into the cylinder during gas exchange. They are usually actuated by camshafts. Free valve area is then a function of valve lift and can be determined with a model by Hardenberg [36]:

$$A_v = \pi\, l_v \cos\, \sigma\, \left(D_v - 2\, l_{vs}\, cos\, \sigma + l_v\, sin\, \sigma\, cos\, \sigma\right)$$
$$\forall\, l_v\, \leq\, l_{vs}/sin\, \sigma$$
$$A_v = \pi\, \sqrt{l_v^2 - 2\, l_v\, l_{vs}\, sin\, \sigma + l_{vs}^2}\, \left(D_v - \, l_{vs}\, cos\, \sigma\right)$$
$$\forall\, l_v\, >\, l_{vs}/sin\, \sigma\, . \tag{3.35}$$

Here free valve area A_v is linked to valve lift l_v and to geometry parameters: the valve seat angle σ, the valve seat length l_{vs}, and the valve diameter D_v, see Fig. 3.9. A switch in lift regimes at $l_v\, =\, l_{vs}/sin\, \sigma$ leads to a distinction of free valve area calculation.

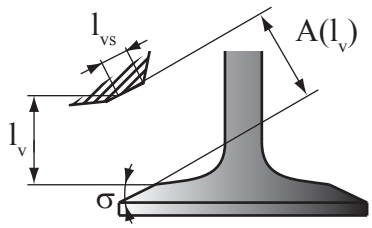

Figure 3.9.: Poppet valve geometry

Discharge coefficients C_d are usually determined using a flow bench, measuring mass flow while a number of different stationary pressure ratios and valve lifts are applied to the valve. Eq. (3.29) is then solved for the discharge coefficient. For a flow bench being not available, values of a similar engine from literature [78] where utilized as depicted in Fig. 3.10. The reason for the negative correlation between discharge coefficient and valve lift is, owing to friction, the elevated energy loss. It accompanies an elevated velocity across the free valve area with a higher valve lift.

Furthermore, a valve lift profile has to be supplied by a table or simplified as a sine function. Shifting of intake camshaft is implemented by shifting of the camshaft angle supplied to the look-up table, Fig. 3.11. Positive camshaft shift is defined as shift to late opening.

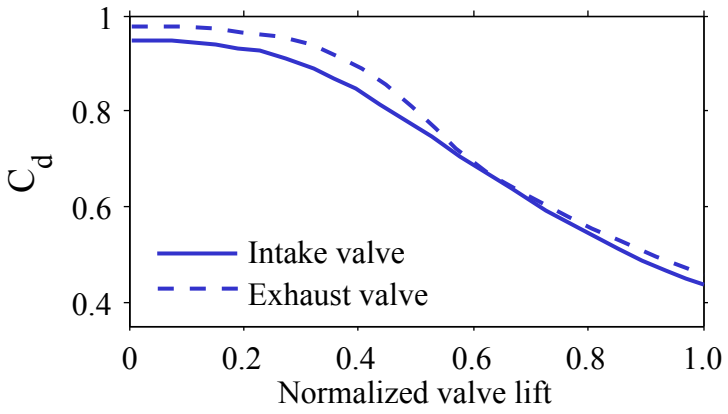

Figure 3.10.: Discharge coefficient of intake and exhaust valves [78]

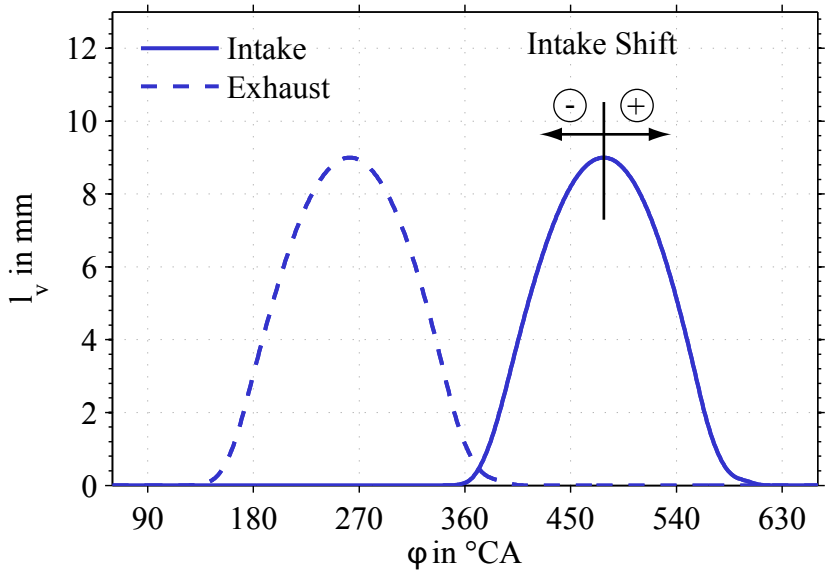

Figure 3.11.: Valve lifts for intake and exhaust valves for $\Delta\varphi_{ivo} = \Delta\varphi_{evo} = 0$

3.3.3. Leakage

Leakage of gas and liquid phase components across the piston rings is, to this day, an unsolved problem. A conflict of objectives is apparent in optimizing the piston rings in regard to sealing and heat transfer on the one hand and friction on the other. When modeling stationary operation, leakage can often be neglected because the impact on in-cylinder pressure is low. This, however, is not the case for the cold start of an engine due to

- low engine speeds,
- engine components, which are not warmed up and have therefore not achieved their stationary operation thermal expansion, which then results in a larger ring gap and
- a thin and discontinuous oil film on the liner.

Excessive leakage leads to a considerable lowering of mass and internal energy of the system, which in turn leads to a reduced pressure and output torque. Leakage paths across the piston rings are lumped into a single effective area, which is modeled as proposed by Rao et al. [71]

$$\begin{aligned} A_{leak} = C_{leak}\ B\ \left(\frac{1000}{n}\right)^{n_{leak}} \quad & \forall n \leq 1000\ min^{-1} \\ A_{leak} = C_{leak}\ B \quad & \forall n > 1000\ min^{-1} \end{aligned} \tag{3.36}$$

where A_{leak} includes both A and C_d in Eq. (3.29). C_{leak} and n_{leak} are model constants.

The distinction of A_{leak} for engine speeds above and below 1000 min^{-1} base on the observed fact of increased leakage with low engine speed and can be explained by the aforementioned cold start issues.

3.4. Combustion

Different approaches are available in literature to model mass conversion during combustion in an internal combustion engine. With increasing complexity these are:

- Vibe burn rate model,
- Quasi-dimensional models,
  - Eddy-breakup model
  - Fractal model

The simple empirical burn rate model by Vibe [92] describes the burnt mass ratio by

$$y_b = 1 - exp\left[-a\left(\frac{\varphi - \varphi_{spark}}{\Delta\varphi_{BD}}\right)^{m+1}\right] \tag{3.37}$$

where a, φ_{BD} and m are model constants, which have to be fitted to a single engine operation point. To overcome this disadvantage of a static model and to achieve a higher degree of flexibility, Csallner [17] extended the modeling approach by parameters as functions of engine inputs such as spark timing, engine speed, EGR rate etc. Although being an enhancement over the original model, it still suffers from narrow boundaries, which is why the Vibe burn rate model is considered as being not suited for cold start simulation.

In regard to flexibility and accuracy on the one hand and reasonable computational effort on the other, quasi-dimensional models represent the best compromise for an engine cold start simulation. These models base on the flamelet-assumption, which states that the flame front in engine combustion is wrinkled by the turbulent flow field but behaves like a laminar flame on a local scale. The flamelet regime can be depicted in the Borghi diagram, Fig. 3.12.

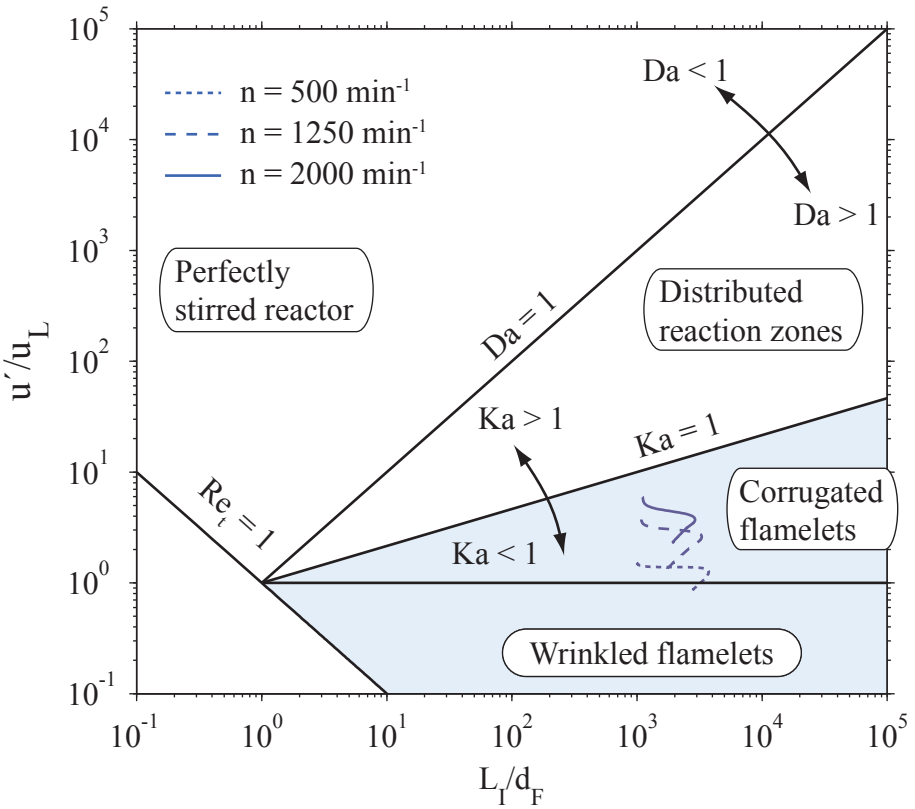

Figure 3.12.: Borghi diagram, Peters [67], with flamelet regimes depicted as shaded area. Computed trajectories at different engine speeds show the validity of the flamelet assumption.

Various combustion regimes can be identified in this diagram dependent upon length L_I/d_F and velocity ratios u'/u_L using two dimensionless criteria Damköhler[1] and Karlowitz[2] number [93]:

- *Perfectly stirred reactor* where $Da < 1$, which expresses that fast mixing occurs due to turbulent motions possessing a lower time characteristic than the chemical reactions.
- *Distributed reaction zones* are characterized by a Kolmogorov time scale smaller than chemical scales which in turn are smaller than the integral time scales. The flow field can thus modify the inner flame structure breaking ground for a thickened flame front to develop.
- *Corrugated flamelets* exhibit a strong wrinkling of the flame front and a formation of pockets of fresh and burnt gases. This regime occurs when chemical time scales are smaller than the Kolmogorov time scales, $Ka < 1$, and the fluctuating velocity of the turbulent flow field u' is larger than the laminar flame speed u_L.
- For the *Wrinkled flamelet* regime $Ka < 1$ applies as well, but u' is lower than the laminar flame speed u_L. Therefore, the flow field wrinkles the flame front but does not cause pockets to develop.

The *Corrugated flamelet* and the *Wrinkled flamelet* regimes are the regimes encountered in premixed flames of SI engines [14]. The Borghi diagram enables a validation of this model assumption. Fig. 3.12 shows the computed trajectories of a combustion process at three representative engine speeds encountered during cold start. All locate in the flamelet regime. Higher engine speeds lead to higher turbulence levels and thus to a shift of the trajectories from *Wrinkled flamelets* to *Corrugated flamelets*.

A widespread quasi-dimensional model that assumes a flamelet regime is the eddy-breakup model, which was initially formulated by Spalding [84] and further refined, see e.g. [13], [39], [60] and [69]. Combustion process is assumed to be dominated by air-fuel mixture entrainment into the flame front where it is burnt according to a burning time for a characteristic

[1] Damköhler number Da is defined as the ratio of integral time scale and chemical time scale of the largest eddies.

[2] Karlowitz number Ka is the ratio of chemical time scales to the Kolmogorov time scale of the smallest eddies.

eddy. Modeling the underlying physical process is more sophisticated than the Vibe model and therefore flexibility is enhanced. However, there are a number of limitations: Matthews and Chin [59] state that there is no experimental evidence that eddies are burning in the post flame zone, which would shift the combustion regime into the distributed reaction regime rather than the wrinkled flamelet regime as supported by experiments. Furthermore, the entrainment velocity is modeled simplified as a sum of the fluctuating component of the flow field u' and laminar flame velocity u_L without experimental evidence. Based on the above mentioned facts another quasi-dimensional combustion model is adopted, namely the fractal combustion model. Here wrinkling of the laminar flame front by turbulence is accounted for by the so-called fractal dimension of the flame. It consists of several submodels: the ignition delay model, the fractal model for the fully established turbulent flame, the flame area calculation and the laminar flame velocity model. These shall be elaborated upon in the context of the next sections.

3.4.1. Ignition Delay

Combustion in SI engines is initialized via an electrode spark. The generated plasma constitutes the flame kernel, which expands into the remaining air-fuel mixture. During this phase pressure rise is minuscule such that a seeming ignition delay is observed. In turn this effect enables the modeling of ignition delay as a time offset after which the fractal combustion model starts with a preset flame radius.

Several approaches to model ignition delay in SI engines exist in literature, e.g. [7], [39]. Since these models do not fit well with measurements, a different approach by Scheele [78] is applied:

$$\Delta t_{ign} = C_{ign}\,\tau \tag{3.38}$$

with C_{ign} as a model constant and τ as the burning time for a characteristic eddy at the time of spark ignition. The approach assumes that the ignition kernel is smaller than a characteristic eddy size and, hence, is not influenced by turbulence. The kernel is burning

in a laminar regime and flame velocity can be set to the laminar flame velocity:

$$\tau = \frac{L_T}{u_L} \,. \tag{3.39}$$

L_T denotes the Taylor micro scale, which can be estimated by

$$L_T = \sqrt{\frac{15\ L_{max}\ \nu_u}{u'}} \tag{3.40}$$

with L_{max} as the outer cutoff scale of the flame and ν_u as the kinematic viscosity of the unburnt gas.

3.4.2. Fractal Combustion Model

After the initialization phase the combustion progresses as a thin flame front strongly influenced by the turbulent flow field. As obvious from flame images [11], [28], [97] the flame front is highly wrinkled by turbulence (Fig. 3.13).

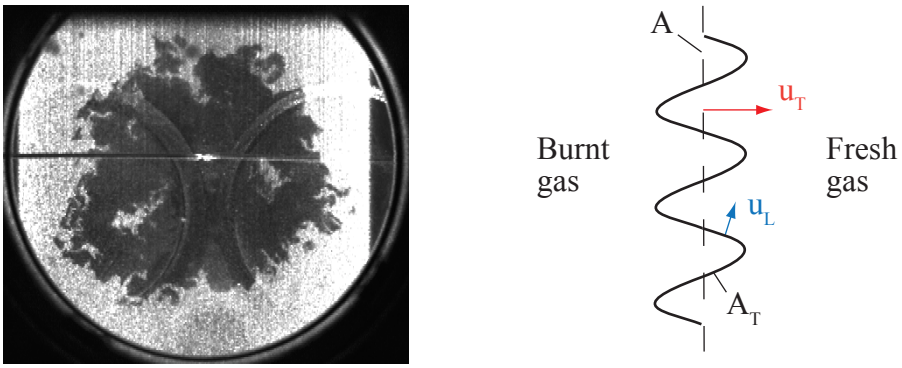

(a) (b)

Figure 3.13.: Turbulent flame front, (a) shows the flame image of spark ignition engine with homogeneous mixture [97], (b) the corresponding model representation

These findings imply that the scale of turbulence is larger than the flame thickness. Therefore, the sole effect of eddies on the flame front is to wrinkle it and consequently to increase the surface area and with it the flame velocity

$$\frac{u_T}{u_L} = \frac{A_T}{A} \,. \tag{3.41}$$

The projected flame surface area A is assumed to be a smooth and spherical surface centered at the spark plug as visible from flame imaging studies [11]. Chemical reactions are not

considered in detail. Instead, laminar flame velocity is modeled empirically as a function of in-cylinder pressure, temperature, relative equivalence ratio and residual gas fraction. It is outlined later on.

Fractal geometry can be used to describe the increase in surface area. This theory was developed by Mandelbrot [56]. It states that a fractal is a rough or fragmented geometric shape that can be split into parts, each of which is (at least approximately) a reduced-size copy of the whole shape. Gouldin [30] adopted this theory for describing a turbulent frame front:

$$\frac{A_T}{A} = \left(\frac{L_{max}}{L_{min}}\right)^{D_3-2} . \tag{3.42}$$

The increase in flame surface area A_T/A is scaled between the inner and outer cutoff limits, L_{min} and L_{max}, by the fractal dimension D_3. These limits characterize the possible influence of the eddies on the flame front. A maximum eddy size L_{max}, the integral length scale, is determined by the combustion chamber geometry and a minimal size that is assumed to be the smallest eddy size and thus the Kolmogorov length.

According to Bozza et al. [14] the outer cutoff scale L_{max} in an internal combustion engine can be described by

$$L_{max} = L_I = C_l \ (s_P + h_{min}) . \tag{3.43}$$

L_{max} scales to the instantaneous clearance height $s_P + h_{min}$ with a constant C_l, which is to be estimated by fitting to appropriate engine measurements. The inner cutoff scale is assumed to be the Kolmogorov length scale

$$L_{min} = L_K = \frac{L_I}{Re_T^{0.75}} \tag{3.44}$$

whereas the turbulent Reynolds number is defined as

$$Re_T = \frac{u' L_I}{\nu_u} , \tag{3.45}$$

with u' as the fluctuation component of the main flow field and ν_u as the kinematic viscosity of the unburnt mixture.

Fractal dimension characterizes the increase in the length of the objects border. It does

not need to be an integer as with euclidean objects and, in fact, exceeds the topological dimension D. In the case of a freely propagating spherical flame front, the fractal dimension is a measure of the roughness or degree of wrinkling of the flame by turbulence. D_3 of the flame is in the order of about 2.1...2.3 whereas the topological dimension is 2 (it is a surface).

The fractal dimension is modeled empirically [76] by

$$D_3 = \frac{2.35\ u' + 2.0\ u_L}{u' + u_L}\ , \tag{3.46}$$

with the laminar flame velocity u_L and the fluctuation component of the flow field u'. For measurement of fractal dimension of a premixed flame refer to e.g. Yoshiyama et al. [97].

The turbulent flame velocity u_T, respectively the increase in flame front area A_T/A, finally enables the calculation of burning rate of the freely propagating flame front

$$\frac{dm_{b,fr}}{dt} = \rho_u\ A_T\ u_L = \rho_u \frac{A_T}{A}\ A\ u_L\ . \tag{3.47}$$

When the flame front reaches the combustion chamber walls, however, conversion rate decreases due to lower temperatures in the boundary layer. This particular burning mode can not be modeled by fractal theory but by a wall-combustion burning rate as proposed by Bozza et al. [14]

$$\frac{dm_{b,W}}{dt} = \frac{m - m_b}{\tau}\ . \tag{3.48}$$

Here τ denotes the characteristic time scale of the process and is described as

$$\tau = \frac{(m - m_b)_{tr}}{(\rho_u\ A_T\ u_L)_{tr}}\ . \tag{3.49}$$

It is assumed that wall combustion burning rate equals turbulent combustion rate at transition time t_{tr}. This transition time is set, when the first flamelets reach the wall

$$t_{tr} = t \quad \text{for} \quad C_{tr}\left(r_F + \frac{L_I}{2}\right) = \frac{B}{2}. \tag{3.50}$$

The transition time is scaled by a constant C_{tr} to achieve better estimation of the latter part of the heat release. Transition between both burning modes is gradual and can be described

by a weighted sum

$$\frac{dm_b}{dt} = (1-w)\frac{dm_{b,fr}}{dt} + w\frac{dm_{b,W}}{dt} \tag{3.51}$$

with a linearly increasing weighting factor

$$w = 1 - \frac{m - m_b}{(m - m_b)_{tr}} \,. \tag{3.52}$$

With known mass conversion rate dm_b/dt, it is finally possible to calculate heat release by burning an air-fuel mixture

$$\begin{aligned} \dot{Q}_b &= \frac{dm_b}{dt}\ \frac{\lambda}{(A/F)_s + 1}\ H_u \quad \forall \lambda < 1 \\ \dot{Q}_b &= \frac{dm_b}{dt}\ \frac{1/\lambda}{(A/F)_s + 1}\ H_u \quad \forall \lambda \geq 1 \end{aligned} \tag{3.53}$$

with H_u as the lower heating value corresponding to 45 MJ/kg for typical gasoline.

3.4.3. Laminar Flame Velocity

To solve Eq. (3.47) it is necessary to obtain knowledge, inter alia, about laminar flame velocity, being a function of pressure, temperature, equivalence ratio and dilution by residual gas. It is possible to solve the equations for the kinetical or equilibrium reactions involved directly with software for computational chemistry, e.g. *CHEMKIN®* [44] or *Cantera* [63] combined with an adequate reaction mechanism. Detailed information about species concentration and temperature during reaction progression can be gained. As modeling pollutant emissions are not the object of this work and this approach requires a high computational effort, it is not pursued here. Instead, empirical correlations are used to model laminar flame velocity. A correlation often used in literature as stated by Metghalchi and Keck [61] is

$$u_L = u_{L,0} \left(\frac{T}{T_0}\right)^{\alpha} \left(\frac{p}{p_0}\right)^{\beta} (1 - 2.1\ Y_{EGR}) \tag{3.54}$$

where Y_{EGR} is the residual gas fraction, α and β are model constants, which have to be fitted to respective measurements. Eq. (3.54) does not account for the shift in lean flammability limit with changing temperature. This is particular problematic for cold start boundary conditions where limited evaporation processes frequently lead to a lean air-fuel mixture.

Therefore, a correlation by Hustad and Sönju [41] is used

$$u_{L,eq} = \frac{D(P)}{100}\left[B(T)\ exp\left(-\left(\frac{1}{\lambda_{eq}} - \frac{1}{\lambda_{max}}\right)^2\right) + C(T)\right], \tag{3.55}$$

which was extended by Meier [60] by a term incorporating the dilution of fresh gases by residual gas:

$$u_L = \left(1 - \frac{Y_{EGR}}{\lambda}\right)^{1.5} u_{L,eq}\ . \tag{3.56}$$

Here λ_{eq} is the equivalent relative equivalence ratio taking residual gas into account

$$\lambda_{eq} = \frac{1}{1 - Y_{EGR}}\ \lambda\ . \tag{3.57}$$

The coefficients of Eq. (3.55) are given by

$$\begin{aligned} D(P) &= \left(\frac{P}{P_0}\right)^{\beta}\ , \\ B(T) &= b_2\ T^{b_1} + b_3\ , \\ C(T) &= c_2\ T^{c_1} + c_3\ , \end{aligned} \tag{3.58}$$

and

$$\beta = \left[-0.16 + 0.22\left(\frac{1}{\lambda_{eq}} - 1\right)\right] \cdot F + 0.01\ . \tag{3.59}$$

With the offset of Eq. (3.59) set to 0.2 as in [60] the model does not yield result as shown in other references, such as [60] or [61]. Hence, the offset is set to 0.01 here to fit the data. Coefficients of Eqs. (3.58) and (3.59) and λ_{max} are given in Tab. 3.1.

The resulting laminar flame velocity of gasoline as a function of relative equivalence ratio, temperature and pressure is shown in Fig. 3.14 and Fig. 3.15. Laminar flame velocity is positively correlated with temperature and negatively with residual gas ratio. Flammability limits are visible as well, which are in turn correlated with temperature and residual gas ratio.

Table 3.1.: Coefficients of the laminar flame velocity model [60]

Fuel	$\mathbf{1/\lambda_{max}}$	$\mathbf{b_1}$	$\mathbf{b_2}$	$\mathbf{b_3}$	$\mathbf{c_1}$	$\mathbf{c_2}$	$\mathbf{c_3}$	**F**
Gasoline	1.1	1.372	6.507e-2	-30	0.9102	-1.05	91.57	1
Propane	1.1	1.478	3.348e-2	-29	1.011	-0.512	74.87	1
Isooctane	1.05	1.374	7.940e-2	-46.62	0.9786	-0.8605	104.5	1
Methanol	1.15	2.251	2.372e-4	-3.235	2.275	-1.255e-4	3.922	1
Hydrogen	1.5	1.032	0.5156	297	0.3167	22.62	-284.1	0

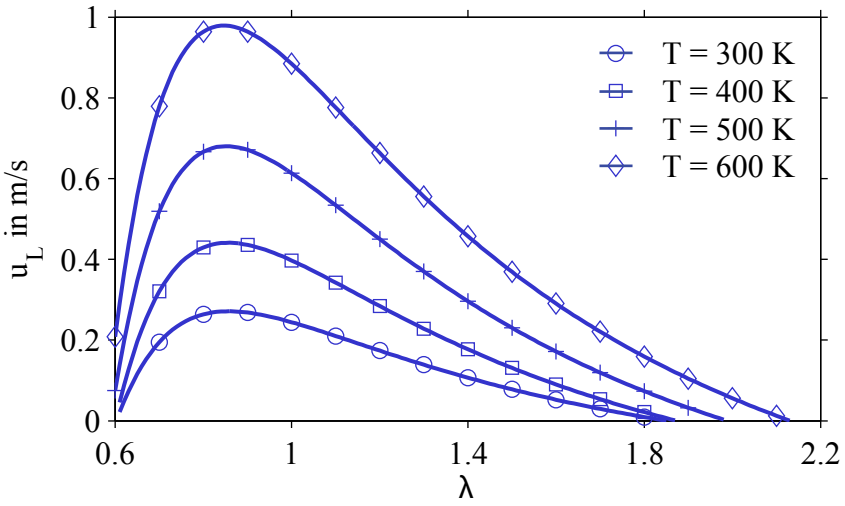

Figure 3.14.: Computed laminar flame velocity of gasoline at $p = 10$ bar and $Y_{EGR} = 0$

3.4.4. Flame Front Area

As obvious from Eq. (3.47), it is necessary to model flame area to obtain turbulent flame velocity and in turn burn rate. The mean flame front is assumed to expand spherically from the spark electrode (Fig. 3.16). When simplifying the combustion chamber as a cylinder with disc shaped piston and head and a centrally positioned spark electrode, four possible flame geometry modes exist: (1) hemisphere, (2) spherical segment for early combustion, (3) spherical cap and (4) spherical segment for late combustion.

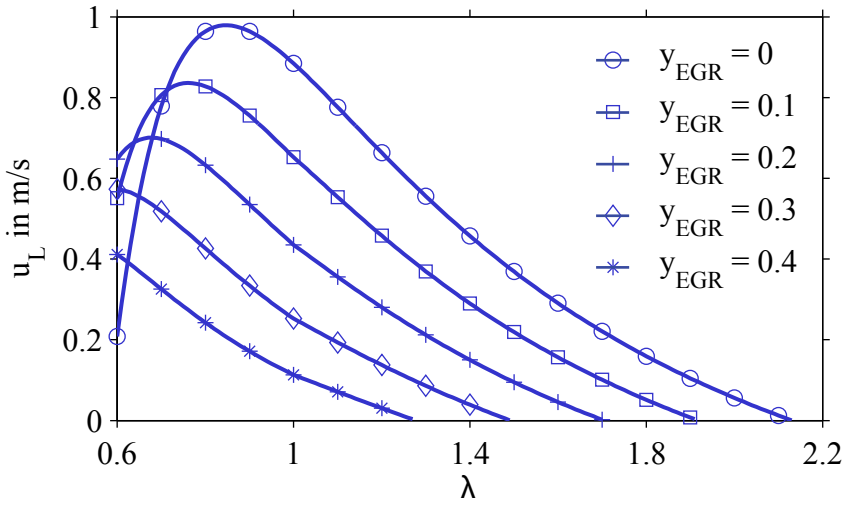

Figure 3.15.: Computed laminar flame velocity of gasoline at $p = 10$ bar and $T = 600$ K

Determination of flame front area is based on known volume of the burnt zone and can be determined by firstly obtaining burnt volume from the two-zone model, Sec. 3.2.2, and secondly, piston position. With this information, one can calculate flame radius and, in turn, the flame area depending on geometry mode as described in Tab. 3.2. Calculated flame front area for the examined engine can be found in the Appendix B.

Table 3.2.: Geometry equations for a spherical flame

	a	$\mathbf{h_1}$	$\mathbf{h_2}$	**A**	**V**
(1)	r_F	0	0	$2\pi {r_F}^2$	$\frac{2}{3}\pi {r_F}^3$
(2)	r_F	s_P	0	$2\pi r_F h_2$	$\frac{\pi}{6}h_2(3a^2 + 3{r_F}^2 - 3{s_P}^2 + {h_2}^2)$
(3)	$\frac{B}{2}$	$r_F - h_2$	$\sqrt{{r_F}^2 - a^2}$	$2\pi r_F h_2$	$\frac{\pi}{3}h_2^2(3r_F - h_2) + \frac{\pi}{4}B^2 h_1$
(4)	$\frac{B}{2}$	$s_P - h_2$	$\sqrt{{r_F}^2 - a^2}$	$2\pi r_F h_2$	$\frac{\pi}{6}h_2(3a^2 + 3{r_F}^2 - 3{s_P}^2 + {h_2}^2) + \frac{\pi}{4}B^2 h_1$

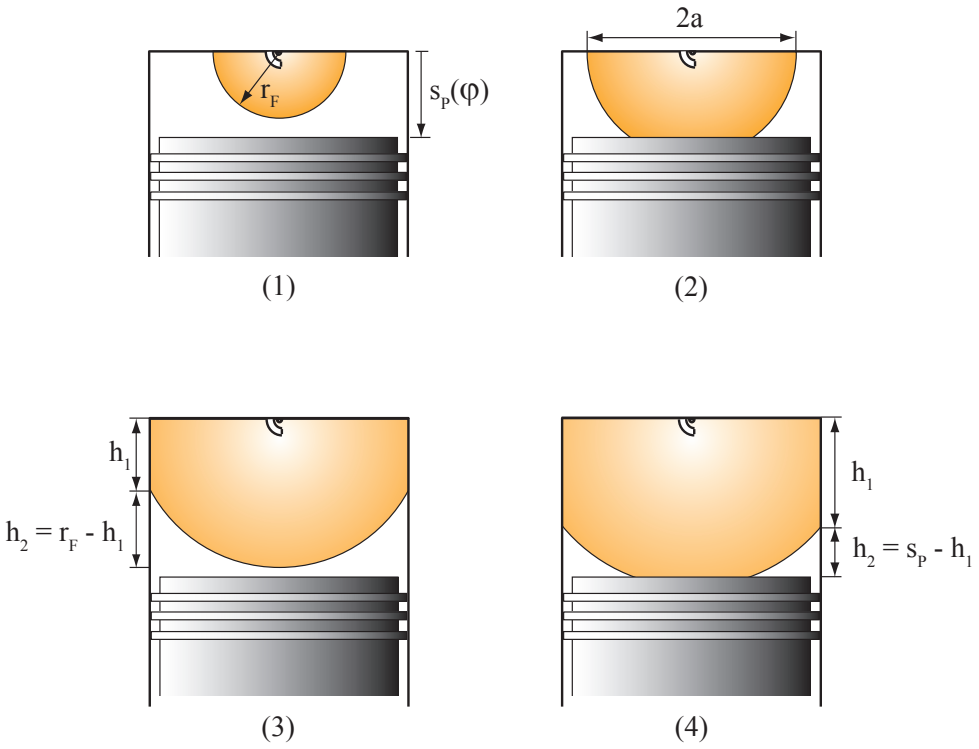

Figure 3.16.: Possible flame front geometries - (1) hemisphere, (2) spherical segment, (3) spherical cap, (4) spherical segment

3.5. Wall Heat Transfer

Solving energy balance, Eq. (3.2), for a given control volume requires information about wall heat transfer. Heat transfer between gas and control volume walls is driven by the temperature difference between gas and walls. Local flow field plays a major role in heat transfer which can be modeled via computational fluid dynamics. This, however, is not in the scope of this work. Semi-empirical correlations based on dimensional analysis of one-dimensional flow are applied here instead. A lumped heat transfer characteristic - the heat transfer coefficient α - describes the heat flow to and from the walls.

3.5.1. Cylinder Wall Heat Transfer

The locally varying heat flows[1] across the system boundaries are modeled as a single heat flow $\dot{Q}_W$. As radiation heat transfer is generally negligible for SI engines [37], Newtons

[1] Due to the locally varying flow fields and temperatures.

relation for convective heat transfer is used exclusively

$$\dot{Q}_W = \alpha_{cyl}\, A_{cyl}\, (T - T_W)\,. \tag{3.60}$$

Temperature T is the mean gas temperature and is provided by the thermal equation of state, Eq. (3.3). T_W is the wall temperature averaged over the whole surface. Surface area A_{cyl} is dependent upon piston position

$$A_{cyl}(\varphi) = A_P + A_{head} + A_{liner}(\varphi) + 0.3\, A_{tl} \tag{3.61}$$

with either given piston A_P and head area A_{head} or with the approximation as flat cylinder $A_P = A_{head} = \frac{\pi}{4}B^2$. Liner area is $A_{liner} = \pi\ B\ s_P(\varphi)$ and piston top land area $A_{tl} = \pi\ B\ H_{tl}$. Heat transfer coefficient α_{cyl} can not be determined by balance equations in the scope of a quasi-dimensional engine model and is therefore modeled semi-empirical by a combined approach described by Kulzer [51]. This approach uses a hybrid model of correlations by Woschni [96] for the gas exchange and by Bargende [8] for the high pressure part of the cycle.

The influence of fluid flow on heat transfer can be modeled using similarity theory with a dimensional analysis of the flow in the combustion chamber. The non-dimensional parameters Nusselt, Reynolds and Prandtl numbers are used to describe the heat transfer coefficient α. The heat transfer model by Woschni [96] is based primarily on this analysis. As a result it estimates α_{cyl} by

$$\alpha_{cyl} = 127.93\ B^{-0.2} p^{0.8} T^{-0.53} \left(6.18\ u' + C_W \Delta p\right)^{0.8} \tag{3.62}$$

with Δp as the pressure rise due to combustion, which is zero during gas exchange. Eq. (3.62) then simplifies to

$$\alpha_{cyl} = 127.93\ B^{-0.2} p^{0.8} T^{-0.53} \left(6.18\ u'\right)^{0.8}. \tag{3.63}$$

The pressure p has to be supplied in bar.

A further improvement of SI engine heat transfer modeling was conducted by Bargende [8]. Bargende introduced a new combustion term Δ, which utilizes the advantages of the two-zone approach of the cylinder volume - the separate modeling of temperatures in the

burnt and unburnt zones respectively - without the need to determine the "wetted" surfaces of the combustion chamber. Δ is defined as

$$\begin{aligned} \Delta &= (A+B)^2 \quad \text{with} \\ A &= x_b \, \frac{T_b}{T} \, \frac{T_b - T_W}{T - T_W} \\ B &= (1-x_b) \, \frac{T_u}{T} \, \frac{T_u - T_W}{T - T_W} \end{aligned} \tag{3.64}$$

and the mean gas temperature T, temperature of the unburnt zone T_u, temperature of the burnt zone T_b from the two-zone model, Sec. 3.2.2. The complete equation for determining heat transfer coefficient by Bargende is

$$\alpha_{cyl} = 253.5 \; V^{-0.073} \; T_m^{-0.477} \; p^{0.78} \; u^{0.78} \; \Delta \; , \tag{3.65}$$

with the actual cylinder volume V, cylinder pressure p in bar, the mean temperature

$$T_m = \frac{T - T_W}{2} \tag{3.66}$$

and the estimated velocity in the control volume

$$u = \sqrt{u'^2 + \left(\frac{u_P}{2}\right)^2} \; . \tag{3.67}$$

3.5.2. Cylinder Wall Temperature

With the mean gas temperature in the combustion chamber T determined by the model for the control volume, see Sec. 3.2.2, and the cylinder surface area A_{cyl} given by Eq. (3.61), only wall temperature T_W is left to be determined to solve Eq. (3.60). Wall temperature during stationary engine operation can be estimated by correlations given by Scheele [78]:

$$\begin{aligned} T_{W,piston} &= 393 \; K + 150 \; K \cdot \left(\frac{n}{n_{max}} \frac{p_{im}}{p_{im,max}} \frac{1 - Y_{EGR}}{\lambda} \right) \\ T_{W,head} &= 393 \; K + 125 \; K \cdot \left(\frac{n}{n_{max}} \frac{p_{im}}{p_{im,max}} \frac{1 - Y_{EGR}}{\lambda} \right) \\ T_{W,liner} &= 393 \; K + 100 \; K \cdot \left(\frac{n}{n_{max}} \frac{p_{im}}{p_{im,max}} \frac{1 - Y_{EGR}}{\lambda} \right) \end{aligned} \tag{3.68}$$

where n_{max} and $p_{im,max}$ denote the maximum engine speed and maximum intake manifold pressure respectively for a given engine.

During cold start this model is not valid as the wall temperature at the onset of the start is equal to the engine starting temperature and rises along with every passed combustion. Hence, a measured cold start wall temperature is used, Fig. 3.17, averaged over all four cylinder wall temperatures. A temperature offset applied to this temperature crank angle relationship covers different start temperatures. Alternatively, a constant wall temperature can be set.

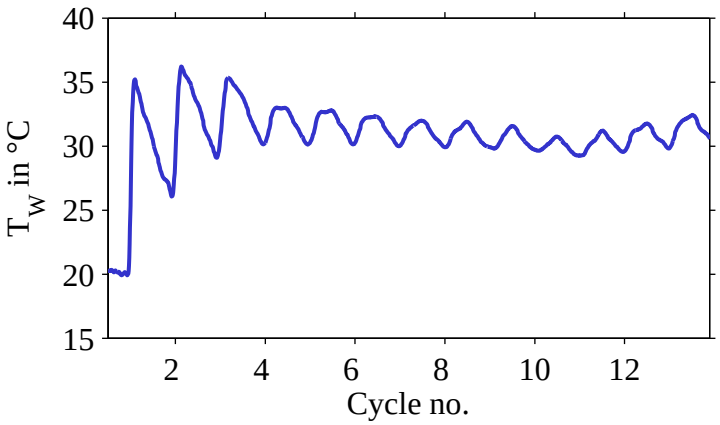

Figure 3.17.: Measured wall temperature of an engine start at 20 °C. Notable is the large amplitude during the first three cycles resulting from high in-cylinder pressure and therefore high gas temperature.

3.6. Turbulent Flow

Making predictions about combustion and wall heat transfer processes in a quasi-dimensional modeling approach can be achieved by a turbulence model that estimates turbulent velocity fluctuation. A common model regarding turbulence is the Reynolds decomposition, where the turbulent flow u is decomposed in a mean value u_F and the superimposed fluctuating component u':

$$u = u_F + u' \,. \tag{3.69}$$

This is also valid for other quantities as e.g. kinetic energy, so one can define K as the kinetic energy of the mean flow and k as the kinetic energy of the superimposed turbulent flow field. To estimate kinetic energies a k-K-model by Poulos and Heywood [69] is applied:

$$\frac{dK}{dt} = \frac{1}{2}\,\dot{m}_{in}\,u_{in}^2 - P + K\,\frac{\dot{m}_{out}}{m} \tag{3.70}$$

and

$$\frac{dk}{dt} = P - m\,\varepsilon + k\,\frac{\dot{m}_{out}}{m} \tag{3.71}$$

respectively. The model describes the build-up and decay of the kinetic energies as functions of various entities. $\dot{m}_{in}$ is the mass flow into the system tied to the inlet velocity u_{in} and $\dot{m}_{out}$ the mass flow out of the system. P is a term that describes the energy transfer along the energy cascade from large eddies to smaller ones and is modeled as

$$P = 0.3307\,C_\beta\,\frac{K}{L_{max}}\,\sqrt{\frac{k}{m}} \tag{3.72}$$

with C_β as the turbulent dissipation constant.

The turbulent dissipation rate ε of Eq. (3.71) characterizes the dissipation of macro scale energy in the form of eddy velocity to a micro scale energy constituted by inner energy and, therefore, noticeable in macroscopic terms as a temperature increase. Turbulent dissipation is

$$\varepsilon = \frac{u'^3}{L_{max}}\,. \tag{3.73}$$

According to Bozza et al. [14], Eq. (3.70) and Eq. (3.71) are extended by a turbulence production term due to density changes $\dot{\rho}/\rho$. These equations then become

$$\frac{dK}{dt} = \frac{1}{2}\,\dot{m}_{in}\,u_{in}^2 - P + K\,\frac{\dot{m}_{out}}{m} + K\,\frac{\dot{\rho}}{\rho} \tag{3.74}$$

and

$$\frac{dk}{dt} = P - m\,\varepsilon + k\,\frac{\dot{m}_{out}}{m} + k\;\frac{\dot{\rho}}{\rho}\,. \tag{3.75}$$

With the knowledge about the kinetic energies one can describe the velocity of the mean flow u_f by

$$K = \frac{1}{2}\,m\,u_f^2\,. \tag{3.76}$$

When assuming *local isotropic turbulence*, which is valid for high Reynolds numbers and small eddies, kinetic energy of the superimposed turbulent flow becomes

$$k = \frac{3}{2}\,m\,u'^2\,, \tag{3.77}$$

which enables calculation of the fluctuating component of the flow field u'. Isotropic means that no preferential spatial direction can be discerned. This assumption is valid for flow fields in the combustion chamber as Reynolds numbers tend to be in the range of 10^4. Fig. 3.18 shows the calculated in-cylinder Reynolds number for the given conditions with a first peak during intake stroke and a second smaller one after TDC during pressure rise due to combustion.

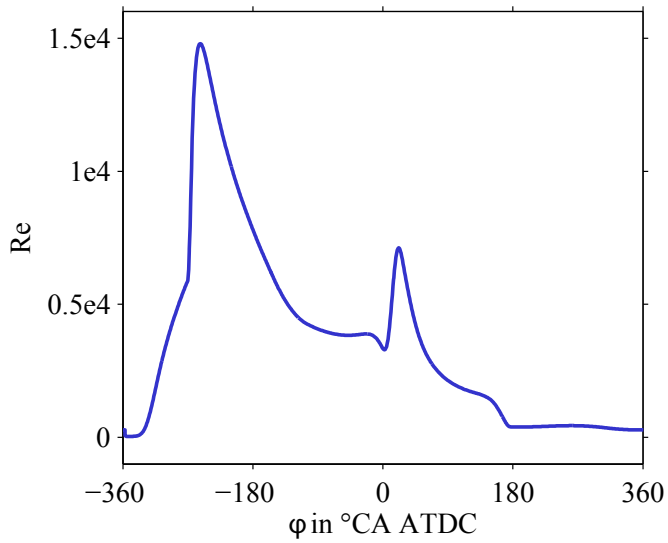

Figure 3.18.: Calculated in-cylinder Reynolds number for $\varphi_{ign} = 5$ °CA BTDC, $p_{im} = 1$ bar, $n = 1000\ \mathrm{min}^{-1}$

3.7. Fuel Injection

To limit model complexity, fuel injection is modeled as proposed by Bargende et al. [9] by a fuel mass flow into the combustion chamber[1], where evaporation takes place as a function of a evaporation time constant τ_{evap}

$$\frac{dm_{fv}}{dt} = \frac{m_f - m_{fv}}{\tau_{evap}} \,. \tag{3.78}$$

with the injected fuel mass m_f and vapor fuel mass m_{fv}. The fuel is injected linearly over time according to

$$\frac{dm_f}{dt} = \frac{m_{f,net}}{\tau_{inj}} \tag{3.79}$$

[1]Since a direct injection engine is modeled.

with the net fuel mass $m_{f,net}$ of the current cycle obtained from the air mass of the preceding cycle with a given relative equivalence ratio

$$m_{f,net} = \frac{m_{air}}{\lambda \, (A/R)_s} \, . \tag{3.80}$$

The evaporated fuel mass is applied to Eq. (3.11). To satisfy Eq. (3.17) it is also necessary to determine the enthalpy of the fuel and the enthalpy of evaporation that is drawn from the combustion chamber. Since parts of the fuel do not evaporate before arriving at the combustion chamber walls, the enthalpy of evaporation is drawn rather from the walls than from the gas. Bargende et al. [9] suggest a ratio of 50 %, which is applied here as well. A resulting injection and evaporation is displayed in Fig. 3.19.

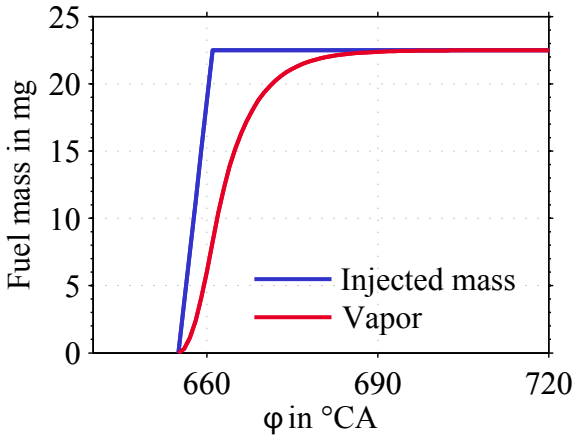

Figure 3.19.: Fuel evaporation with $\tau_{inj} = \tau_{evap} = 10^{-2}$ s for $p_{in} = 1$ bar, $\lambda = 1.0$, speed $= 1000$ min^{-1}

3.8. Exhaust Gas Recirculation

EGR is the amount of exhaust gas residing in the cylinder volume from the preceding cycle. For conservative engine concepts the term EGR comprises three possible effects: residual gas, valve overlap effect and external EGR. In Diesel engines, where pressure ratio between intake and exhaust manifold is of the order of two to three and residual gas consists mostly of air, residual gas and valve overlap effects do not play a major role in the engine cycle. Hence, external EGR is required to implement exhaust gas recirculation. This is, however, not the case for SI engines.

Due to lower intake pressures during partial load, residual and overlap effects are the dominating effects. The possibilities to manipulate the amount of residual gas are limited, whereas the overlap effect is exploited by applying a variable camshaft.

Increasing residual gas fraction has several effects on engine operation:

- Less trapped fresh air (at the same intake pressure and temperature). With stoichiometric operation this results in a lower heat release. This effect is also dependent on temperature of the preceding cycle: a higher temperature leads to a lower volumetric efficiency which is obvious from the thermal equation of state, Eq. (3.3) and is often used for thermal dethrotteling to reduce pumping losses.

- Lowered maximum burn temperature due to inert gas, delayed combustion and higher specific heat capacity of the burnt gas[1]. This leads to a reduced NO_x generation - which is the main reason why it is utilized for Diesel engines.

- Increased cyclic variations.

A semi-empirical model by Fox et al. [25] is employed to predict EGR. It is based on the following assumptions

- *Residual gas is distributed homogeneously throughout the control volume.* This is a direct conclusion from the 0D-approach of the control volume modeling.

- *Residual gas can be described by a mixture of burnt gases of the previous cycle.* A distinction in regard to temperature of unburnt or burnt zone is applied since the specific heat capacity is a strongly non-linear function of temperature.

- *EGR is assumed to be zero for the first cycle of a cold start.* The purge of the cylinder volumes during coast-down can be expected to be complete, the reason being the engine shut-down taking several engine cycles during which fresh air flows through the engine and no fuel is injected.

The model considers the following input variables: engine speed, intake and exhaust pressure, compression ratio, equivalence ratio and a valve overlap that accounts for the flow across the valve during overlap period.

[1] Burnt gas components H_2O and CO_2 are three-atomic molecules with corresponding higher degrees of freedom and therefore higher specific heat capacity.

The EGR rate $Y_{EGR} = m_{EGR}/m$ is assumed to be comprised of two different effects: The residual gas is the part that is not purged during gas exchange and resides in the cylinder when the next cycle starts. It is modeled via

$$y_{EGR,res} = C_{res} \, \frac{1}{\lambda} \, \frac{(p_{im}/p_{em})^{-0.74}}{\varepsilon} \tag{3.81}$$

depending on the relative equivalence ratio λ, pressures in the intake and exhaust manifolds p_{im} and p_{em} and the compression ratio ε.

If valve overlap is applied, a back flow from exhaust manifold into the cylinder occurs especially at partial loads where intake manifold pressure is low. This back flow is characterized by a valve overlap factor [25]

$$OF = \frac{d_{iv} \, A_{iv} + d_{ev} \, A_{ev}}{V_d} \tag{3.82}$$

with the intake valve diameter d_{iv} and exhaust valve diameter d_{ev}. The valve-lift integrals A_{iv} and A_{ev} denote areas under the valve-lift/crank-angle curves:

$$A_{iv} = \int_{ivo}^{iv=ev} l_{iv} \, d\varphi \quad \text{and} \quad A_{ev} = \int_{iv=ev}^{evo} l_{ev} \, d\varphi \, . \tag{3.83}$$

Utilizing the overlap factor makes it possible to model the overlap gas fraction

$$y_{EGR,ov} = C_{ov} \, \frac{OF}{n} \, \left(\frac{p_{im}}{p_{em}} \right)^{-0.87} \sqrt{|p_{em} - p_{im}|} \, . \tag{3.84}$$

C_{res} and C_{ov} are non-dimensional constants with values of 0.632 and 1.266 respectively [25]. The sum of both effects then constitutes the EGR rate

$$Y_{EGR} = y_{EGR,res} + y_{EGR,ov} \, . \tag{3.85}$$

Finally the EGR is set to zero for the first combustion of each cylinder and to the modeled value afterwards.

3.9. Gas Properties

Several properties of gaseous media are required in different parts of the engine model. Specific heat capacity c_p and molar weight MW of air and burnt gas as well as the fuel are used for calculating dU in the energy balance, Eq. (3.2). This can be achieved by using the caloric equations of state

$$h = c_p\, T \quad \text{and} \quad u = c_V\, T \tag{3.86}$$

with the correlation between c_V and c_p

$$c_V = c_p - R_u/MW \quad \text{or} \quad c_V = c_p - R\,. \tag{3.87}$$

Furthermore, transport properties of air, namely viscosity, are required for Reynolds number calculation in the combustion model (Sec. 3.4) as well as the enthalpy of evaporation of the fuel modeled.

3.9.1. Burnt Gas

Various attempts to model caloric properties of burnt gas are available in literature. A common approach, especially for modeling Diesel engines, is the model by Zacharias [98], who used a component approach for the burnt gas. With information about fractions of the species appearing in a gas mixture for a given temperature and pressure, one can calculate the properties of the mixture by the mixing rule for ideal gas. As pointed out by Warnatz et al. [93] more than 1000 species occur during the combustion process of an internal combustion engine. Tracking every single species is very time consuming, making a reduction sensible. Zacharias considered 20 species and concluded there would be a chemical equilibrium at temperatures higher than 1500 K. Real gas behavior is accounted for by applying a virial expansion of the ideal gas equations of state. The resulting data was then approximated by a polynom. An advantage of the Zacharias algorithm is the efficiency in terms of computing time. A major drawback, however, is the fixed H/C-ratio to 2.35, which is a H/C-ratio of long-chain hydrocarbons typical for Diesel fuel. Grill [32] showed large deviations for equilibrium mole fractions between H/C-ratios of Gasoline and Diesel fuel respectively, which leads to large deviations in caloric properties as well. Furthermore, the model is valid for stoichiometric and over-stoichiometric equivalence ratios only. This

fact renders the model unsuitable for SI engine cold start simulation, where low equivalence ratios are encountered.

Another recent work to model burnt gas properties is outlined by de Jaegher [43], which employs an equilibrium calculation of a number of species as well. The gas properties are based on the JANAF tables [87]. This work enhances the considered domain by the under-stoichiometric part. A still fixed H/C-ratio of 2.0 limits this approach also.

Based on the restrictions of the aforementioned approaches to modeling flue gas properties, a more flexible approach is applied in this work. The chemical software *Cantera* [63] is used to calculate the chemical equilibrium of an air-fuel mixture on a discrete grid of pressure, temperature and equivalence ratio solving an equation system of equilibrium reactions for a minimum in Gibbs energy.[1]

The widespread GRI-Mech reaction mechanism [83] provides the equilibrium constants for this equation system. GRI-Mech is a chemical mechanism consisting of 53 species with 325 reactions. The mechanism contains no larger species than propane, this, however, is of no concern since equilibrium composition is independent of the length of hydrocarbons to start with. On the other hand, it is not independent of hydrogen-to-carbon ratio of the fuel. This ratio is implemented by assuming a mixture of C_3H_8 and C_2H_2, which satisfies the constraint given by the fuel to be modeled, here gasoline, with a H/C-ratio of 1.85.

It is possible to calculate the kinetics of chemical reactions and it is reasonable, too, if pollutant emissions are to be modeled. This detailed computing can become very complex and unwieldy. Dependent upon the mechanism up to several hundreds or thousands of differential equations have to be solved. As mentioned, this can be circumvented by assuming chemical equilibrium, since caloric and transport properties of the mixture are of interest only and the influence of minor species is negligible for these, see Fig. 3.20.

A common approach is then to apply a freezing temperature [43], [32] to the equilibrium calculation. Above the freezing temperature full equilibrium at the specific operating point is applied, below it the reactions are assumed to be "frozen". A freezing temperature of 1600 K is assumed according to an equilibrium study carried out by Grill [32]. Grill considered CO-

[1] Refer to [91], [93] for further information about chemical reaction modeling.

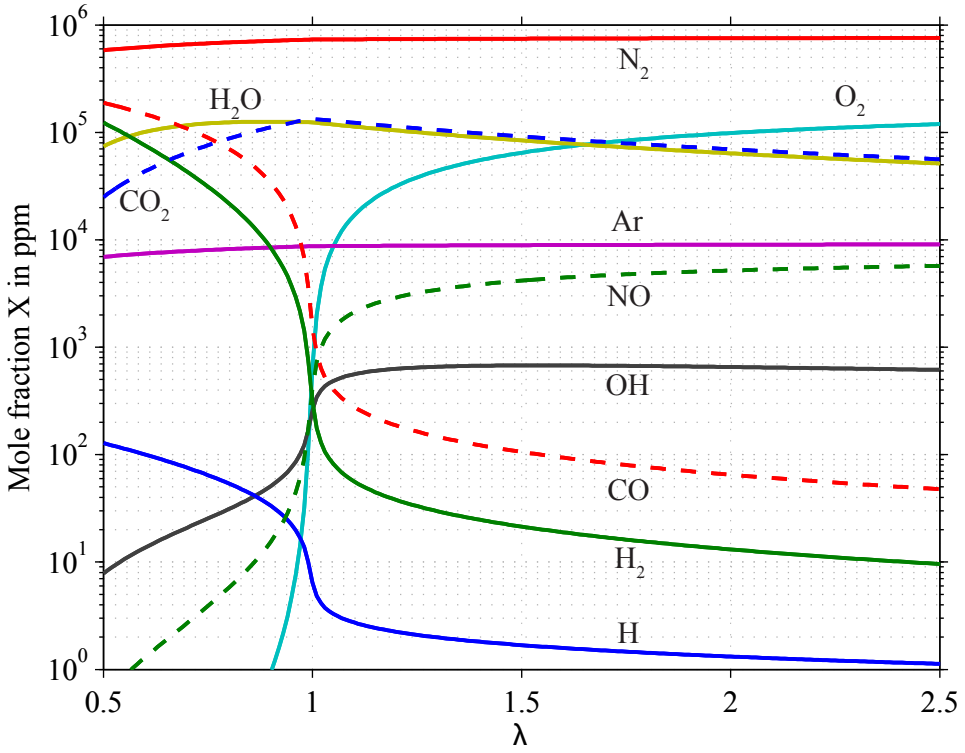

Figure 3.20.: Calculated mole fractions of burnt gas for a gasoline-air mixture with a H/C-ratio of 1/1.85 in equilibrium at $T = 2000$ K and $p = 20$ bar

oxidation and OH-creation during an infinitely fast cool down of a burnt gas mixture by 100 K and showed that a freezing temperature of 1600 K represents a valid compromise for most engine operating points.

The properties c_p and MW are then stored in a three dimensional table $f(T, p, \lambda)$ on a grid of 100 K for temperature, $1, 10, 100$ bar for pressure and values of 0.6, 0.8, 1.0, 1.2, 1.6, 2, 5, 10^6 for λ. Fig. 3.21 shows the specific isobaric heat capacity c_p of a burnt gas in chemical equilibrium at a pressure of 20 bar.

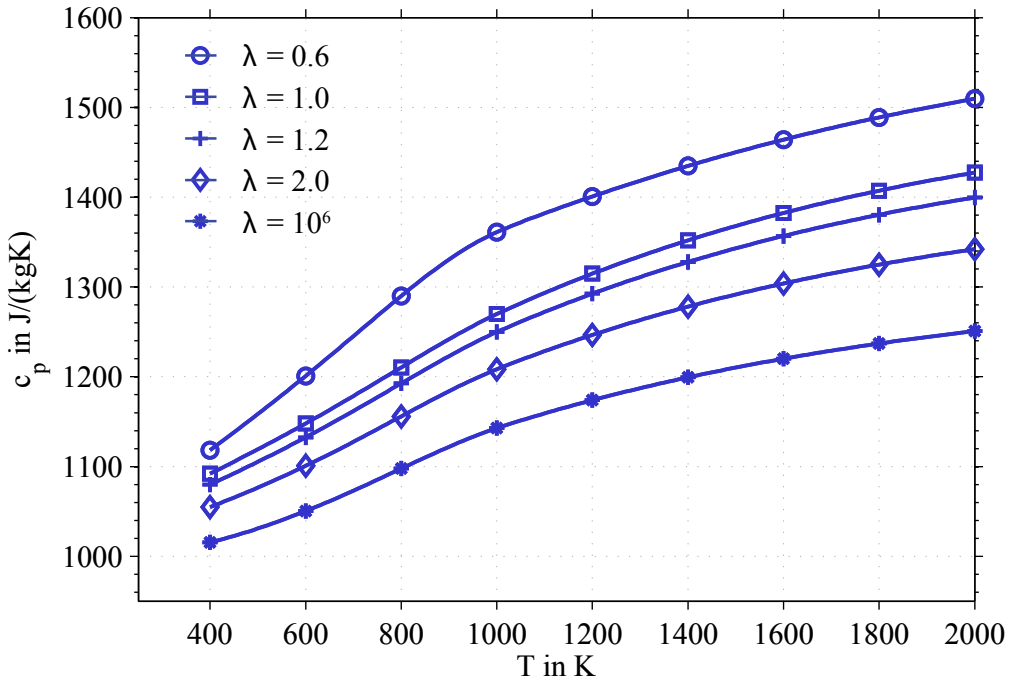

Figure 3.21.: Calculated specific heat capacity of burnt gas for a gasoline-air mixture with a H/C-ratio of 1/1.85 in chemical equilibrium at $p = 20$ bar

Summarizing the aforementioned facts, the following advantages of this method can be stated:

- The H/C-ratio can be supplied according to the fuel considered,
- flexible equivalence ratio,
- dissociation is accounted for,
- the humidity can be specified,
- the low computational effort and
- the availability of *Cantera* as a solver for chemical reactions and for mixtures.

3.9.2. Air

Dynamic viscosity as well as specific heat capacity of air are primarily a function of temperature[1] and can be obtained from literature, e.g. [42], [91]. Here, the component approach,

[1] In the temperature-pressure regime found in an internal combustion air can be treated as ideal gas as mentioned in Sec. 3.2.

described above, is used to supply these properties. It is capable of providing information of gas properties with respect to the humidity of air. Water has a lower molar weight and a higher specific heat capacity than dry air and, therefore, biases these properties of air and burnt gases. A further consequence is the lowered oxygen mole fraction and a lowered heat release during the engine cycle.

A variation of the relative humidity of air is displayed in Fig. 3.22. The relative difference in specific heat capacity at constant pressure is about 1.2 % for dry air compared to air with a relative humidity of $\phi = 1$.
Pressure and temperature effects on molar weight of (humid) air is negligible and is assumed to be $MW_{air} = 28.86\,^{\mathrm{kg}}/_{\mathrm{kmol}}$.

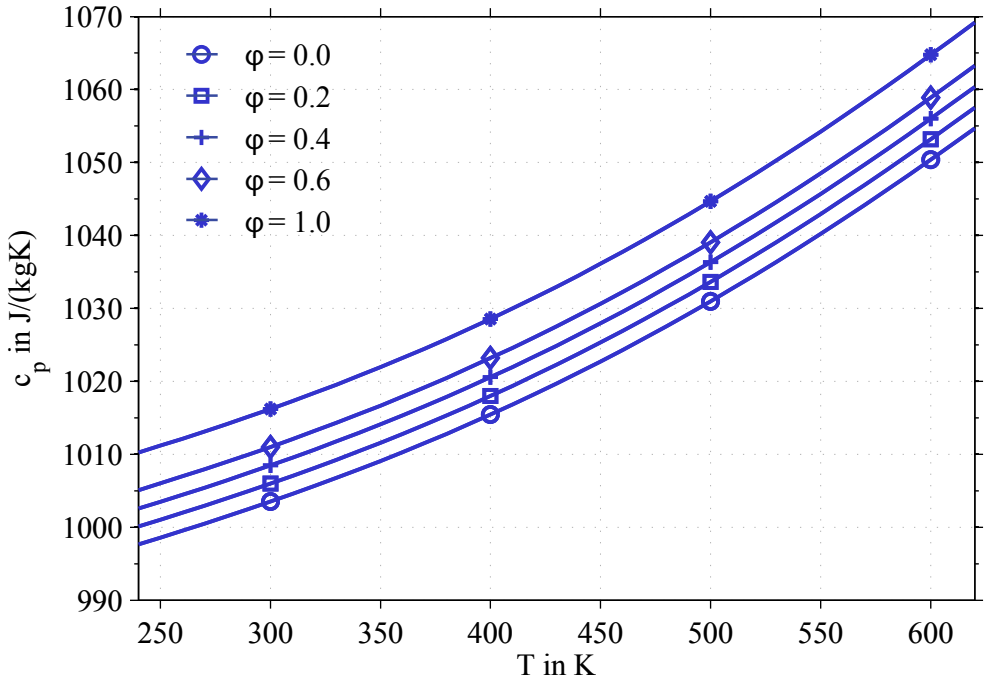

Figure 3.22.: Calculated specific heat capacity of air at different relative humidities referenced to $T = 293$ K and $p = 1$ bar

3.9.3. Fuel

Since evaporation of fuel is modeled with a constant evaporation time and transport processes of fuel are not accounted for (Sec. 3.7), molar weight, specific heat capacity at constant

pressure and enthalpy of evaporation have to be determined only.[1]

Specific heat capacity at constant pressure is calculated by polynoms, see Turns [91]:

$$\overline{c_p} = 4.184 \left(a_1 + a_2\,\theta + a_3\,\theta^2 + a_4\,\theta^3 + a_5\,\theta^{-2}\right) \tag{3.88}$$

with $\theta = T/1000$. Here $\overline{c_p}$ denotes the molar heat capacity. The specific heat capacity is defined as

$$c_p = \frac{\overline{c_p}}{MW}\ . \tag{3.89}$$

Tab. 3.3 shows the coefficients for Eq. (3.88).

Table 3.3.: Coefficients for specific heat capacity of different fuels [91]

Fuel	**Formula**	**MW**	$\mathbf{a_1}$	$\mathbf{a_2}$	$\mathbf{a_3}$	$\mathbf{a_4}$	$\mathbf{a_5}$
Isooctane	C_8H_{18}	114.23	-0.55313	181.62	-97.787	20.402	-0.03095
Methanol	CH_3OH	32.04	-2.7059	44.168	-27.501	7.2193	0.20299
Ethanol	C_2H_5OH	46.07	6.990	39.741	-11.926	0	0
Gasoline	$C_{8.26}H_{15.5}$	114.8	-24.078	256.63	-201.68	64.750	0.5808
Gasoline	$C_{7.76}H_{13.1}$	106.4	-22.501	227.99	-177.26	56.048	0.4845

Specification of enthalpy of evaporation of gasoline vary widely between 305 $^{\mathrm{kJ}}/_{\mathrm{kg}}$, Heywood [37], and 420 $^{\mathrm{kJ}}/_{\mathrm{kg}}$, Bargende et al. [9]. No experimental data being available, a mean value of 362.5 $^{\mathrm{kJ}}/_{\mathrm{kg}}$ is used.

3.10. Power Transmission

On the basis of known in-cylinder pressure, the modeling of the engine speed during cold start requires knowledge about the acting torques on the moving engine parts. This can be acquired by applying an energy balance in the form of a balance of external torques on the

[1] In contrast to more sophisticated evaporation models as in [19], [80], where properties such as viscosity, density and diffusion coefficients have to be determined as well.

powertrain

$$M_{gas} + M_{starter} = M_{inertia} + M_{friction} + M_{break} + M_{gen} \ . \tag{3.90}$$

The individual torques are:

- M_{gas} the torque caused by the gas forces on the piston,
- $M_{starter}$ the torque delivered by the starter,
- $M_{inertia}$ the torque occurring during acceleration and deceleration of a given mass, which is used to determine engine speed,
- $M_{friction}$ the torque caused by friction of the moving engine parts,
- M_{break} the useful torque transmitted to the device to be moved, here the wheels of the car, for cold start this is usually zero as the gearbox is disengaged,
- M_{gen} the torque required to drive the generator and is assumed to be zero.

These torques shall be described in the following section. A depiction of simulated torques during a typical engine start-up is shown in Fig. 3.23. The figure shows the starter torque required to overcome friction and pumping losses until the first combustion occurs. During the expansion following the first combustion, work is transferred to the power train and an acceleration in engine speed is evident. This acceleration is caused by the torque transferred to the inertias of the system.

3.10.1. Crankshaft

A number of different one-dimensional crankshaft models are possible. With increasing complexity these are: a rigid crankshaft with a single-mass flywheel as shown in Fig. 3.24, a rigid crankshaft model with a two-mass fly wheel, Fig. 3.25, and an elastic crankshaft with a two-mass flywheel, Fig. 3.26.
In contrast to FEM, this approach reduces the number of necessary equations restricting the computational effort to reasonable values in the context of cold start simulation. The compound of crankshaft, attached flywheel and auxiliary systems is divided into several inertias: one inertia for the auxiliary systems, four inertias for the crankshaft (one for each crank slider mechanism) and two for the two-mass flywheel. The inertias are connected by

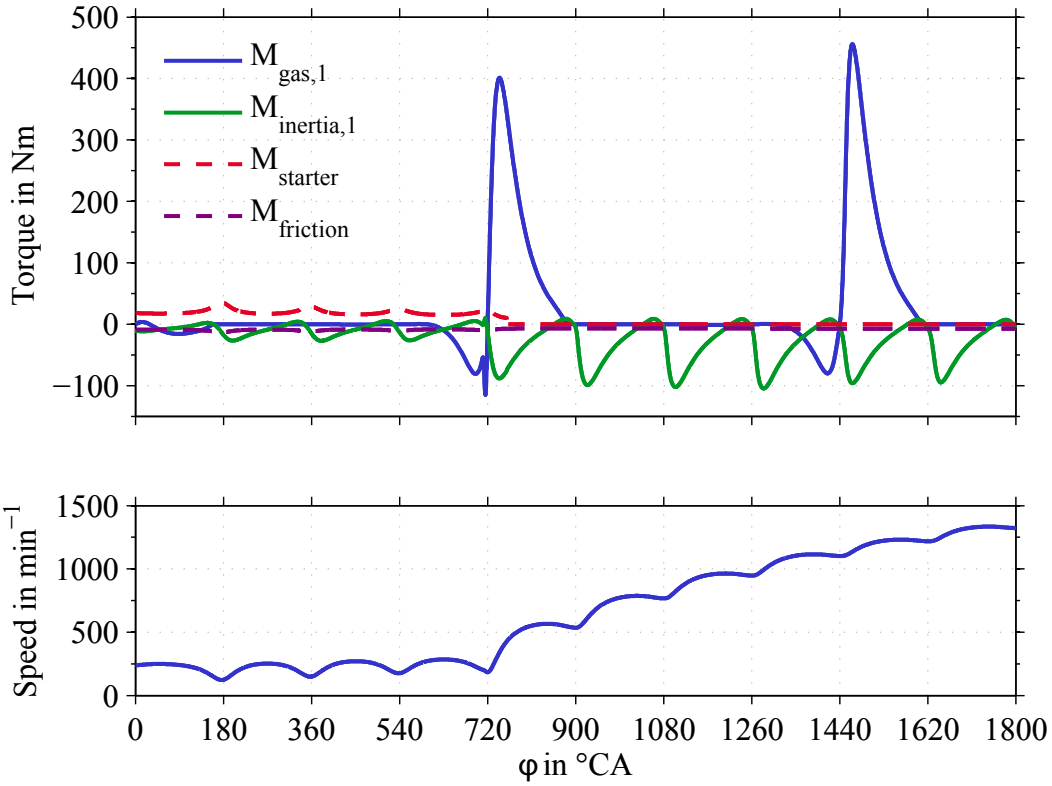

Figure 3.23.: Calculated torques and engine speed during a typical engine start up for an engine with a rigid crankshaft

spring-damper elements, each with a constant spring and damping coefficient determined by fitting to measurements.

For solving mathematical models of mechanical systems with finite degrees of freedom different traditional algorithms are at hand, e.g. Lagrange's equations [89]:

$$\frac{d}{dt}\left(\frac{\partial L}{\partial \dot{q}_j}\right) - \frac{\partial L}{\partial q_j} = Q_j \tag{3.91}$$

with the Lagrange function L

$$L = E_{kin} - E_{pot} \tag{3.92}$$

and q as the generalized coordinates, in this case the crank angle φ. Q_j is the term for sources and sinks such as dampings, starter torque, gas torques and output torque. Let

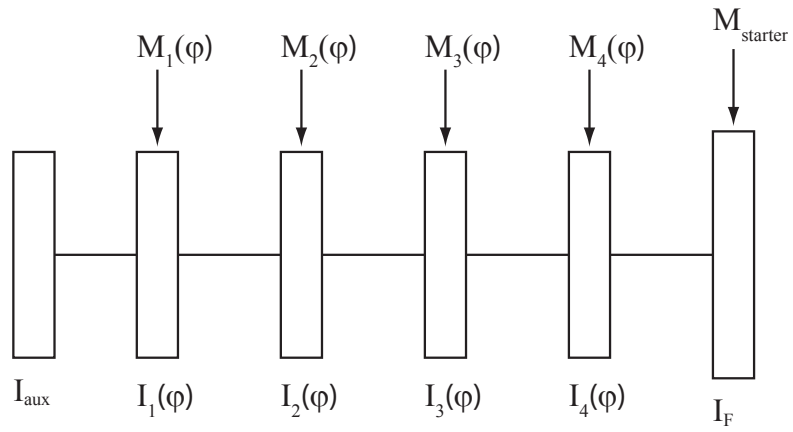

Figure 3.24.: Model of a rigid crankshaft with a single-mass flywheel

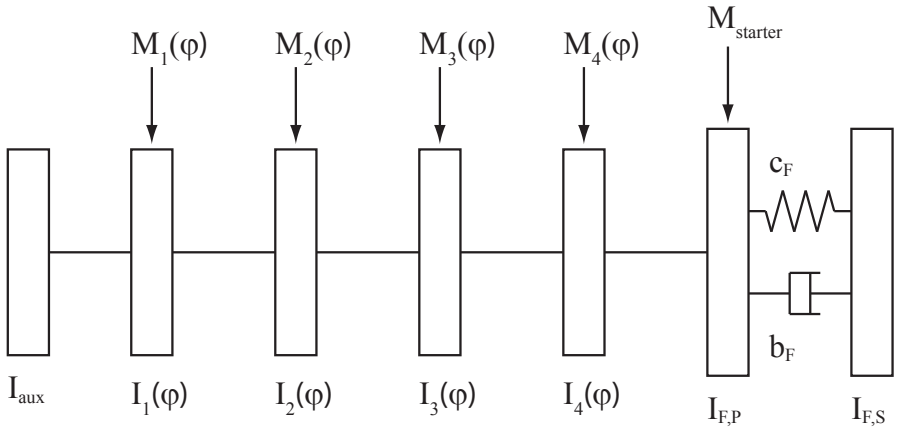

Figure 3.25.: Model of a rigid crankshaft with a two-mass flywheel

E_{kin} represent the kinetical energy of the system

$$E_{kin} = \sum_{i=1}^{N} \frac{1}{2} I_i(\varphi)\ \dot{\varphi}_i^2 \tag{3.93}$$

and E_{pot} the potential energy

$$E_{pot} = \sum_{i=1}^{N} \frac{1}{2} c_{i,i+1} \left(\varphi_i - \varphi_{i+1}\right)^2 \ . \tag{3.94}$$

The obtained equation system can be used to describe mechanical systems with simulation software like *SIMULINK* [57]. This work, however, exploits the advantages of *DYMOLA* where equations for an individual object such as a spring or damper can be stated individually. The instancing and connection of the objects generate an equation system that is

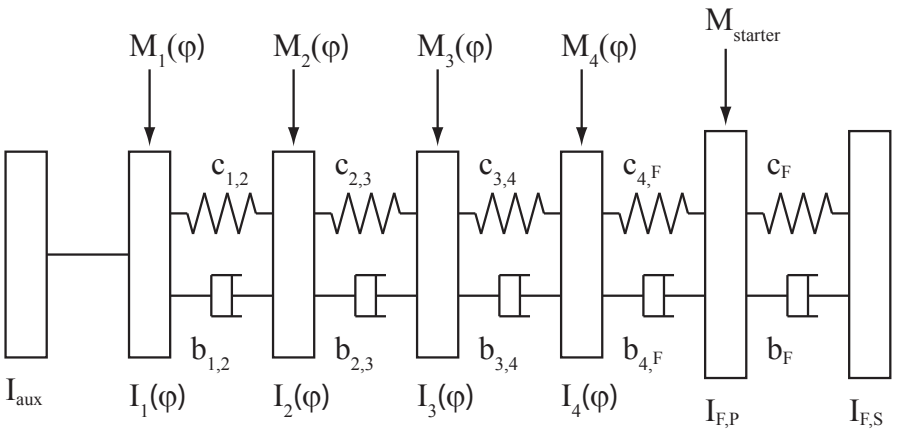

Figure 3.26.: Model of an elastic crankshaft with a two-mass flywheel

solved by an integration algorithm supplied by the simulator. Dresig [21] states that a model containing both stiff and non-stiff elements, here the crankshaft and the two-mass flywheel respectively, should be avoided to prevent stiff differential equation systems. Solvers for stiff systems being readily available, this problem is not as serious and both models with a two-mass flywheel can be used with little difference in computing time.

Moment of Inertia

Rotational inertia is a property of a given body determined by its mass and geometry. It characterizes the resistance to changes in movement, be it direction or value. Governing equations for a rotational inertia object are [65]

$$\begin{aligned} \varphi_i &= \varphi_{i+1} \ , \\ I\ \ddot{\varphi}_i &= M_i + M_{i+1} \ . \end{aligned} \tag{3.95}$$

where i denotes a position index.

In general, the moment of inertia of an individual object can be calculated by decomposition of a given mass into infinitesimal small mass elements dm and integrating the square of each radius over these mass elements

$$I = \int r^2 \, dm \ . \tag{3.96}$$

For a cylinder with a constant density the moment of inertia around the rotational axis

yields

$$I_{cyl} = \frac{1}{2} r^2 \, m \; . \tag{3.97}$$

Moments of inertia of oscillating parts of the engine, like piston and part of the connecting rod, are not independent of crank angle φ. Instead they vary with changing position r of these elements. Since the connecting rod has a rotating and an oscillating movement component, a common approach is to discretize the connecting rod into two masses [35]. In this case, the oscillating mass is given by the engine data sheet, but can, however, be determined by breaking down the mass into one third oscillating and two thirds rotating mass if the center of gravity is not known. The moment of inertia of a crank slider mechanism is therefore

$$I(\varphi) = r^2 \, m_{rot} + r^2 \, m_{osc} \, x'^2 \tag{3.98}$$

respectively

$$I(\varphi) = I_{rot} + r^2 \, m_{osc} \, x'^2 \tag{3.99}$$

and the differentiation yields

$$I'(\varphi) = \frac{dI}{d\varphi} = 2 \, m_{osc} x' \, x'' \, r^2 \; . \tag{3.100}$$

The governing equations for an oscillating element are then

$$\begin{aligned} \varphi_i &= \varphi_{i+1} \; , \\ I \, \ddot{\varphi}_i + \frac{1}{2} I' \dot{\varphi}_i^2 &= M_i + M_{i+1} \; . \end{aligned} \tag{3.101}$$

Spring and Damper

The powertrain compound itself is characterized by certain spring and damping behavior. It is, as the inertias mentioned above, discretized into individual spring-damper elements. The springs are implemented as ideal, massless springs with the governing equations

$$\begin{aligned} 0 &= M_i + M_{i+1} \; , \\ M_{i+1} &= c \, (\varphi_{i+1} - \varphi_i) \; . \end{aligned} \tag{3.102}$$

The torque applied to a spring induces a torsion of the spring element according to the spring stiffness c.

Analogue, an ideal, massless damper is used

$$\begin{aligned} 0 &= M_i + M_{i+1} \ , \\ M_{i+1} &= b\left(\dot{\varphi}_{i+1} - \dot{\varphi}_i\right) \ . \end{aligned} \tag{3.103}$$

Here the applied torque induces a change in angular velocity dependent on the damping constant b.

Two-Mass Flywheel

Due to the strongly non-uniform output torque of internal combustion engines (compare Fig. 3.23), a flywheel (Fig. 3.27) is mounted on the output side of the engine. The task of the flywheel is to dampen the oscillations of the powertrain on the gear box side to increase comfort to the passengers and to decrease stress on the gear box itself [23].

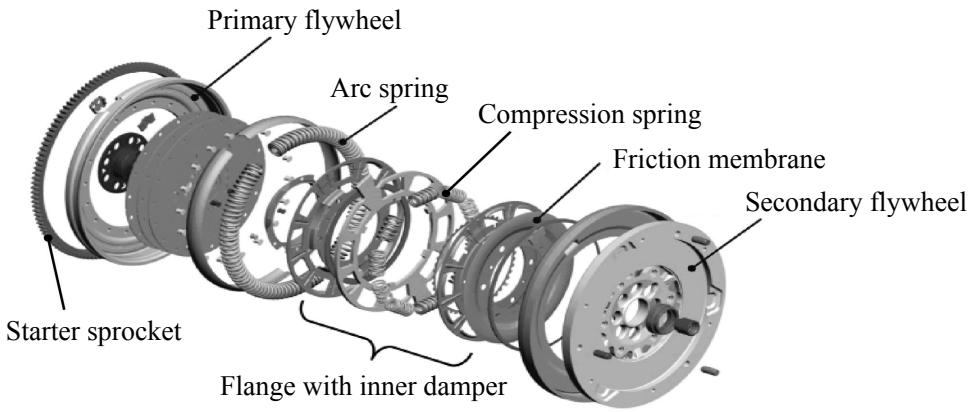

Figure 3.27.: Structure of a two-mass flywheel [6]

For modern engines with high indicated mean effective pressures this approach is insufficient as torque amplitudes are higher and can not be filtered adequately with a single mass flywheel. Therefore, two-mass flywheels [23] consisting of two masses connected by springs and dampers were developed. Masses, spring stiffnesses and dampings are adjusted in such

a way as to achieve a high degree of isolation between engine and output side during normal engine operation. However, isolation at high engine speeds implies resonance frequencies at low levels. The resonance frequency has to be passed during engine start-up, which can lead to oscillations with large amplitudes dependent upon the time spent in the resonance frequency range [72]. An engaging of the starter beyond resonance frequency of the two-mass flywheel can lessen this effect.

Nonetheless, oscillations during passage have a strong influence on engine speed and can be modeled by a spring-damper element with appropriate parameters. Common two-mass flywheels display a complex configuration with different springs and a damping that is caused by a friction disk as well as by the mounting of the springs in grease. Despite this, the same simple modeling approach as with the crankshaft is used to reduce model and calibration complexity.

3.10.2. Gas Torque

The gas force F_P resulting from the pressure in the cylinder is transmitted by the connecting rod to the crank of the crankshaft and, in effect, causes a torque, see Fig. 3.28. This torque can be expressed as

$$M_{gas} = F_P \; s_\perp(\varphi) \tag{3.104}$$

where $s_\perp$ is the lever of force F_P at any position φ. The piston force is determined by the cylinder pressure p_{cyl} and the piston area A_P

$$F_P = A_P \; (p_{cyl} - p_{cc}) \tag{3.105}$$

with the assumption that crank case pressure p_{cc} is equal to atmospheric pressure.
The piston position s_p can be deducted from Fig. 3.28 as

$$s_P = \sqrt{(l+r)^2 - d^2} - r \; cos \; \varphi - l \; cos \; \psi \; . \tag{3.106}$$

Defining the connecting rod ratio $\lambda_c = r/l$ as well as the offset ratio $\mu = d_{off}/l$ and

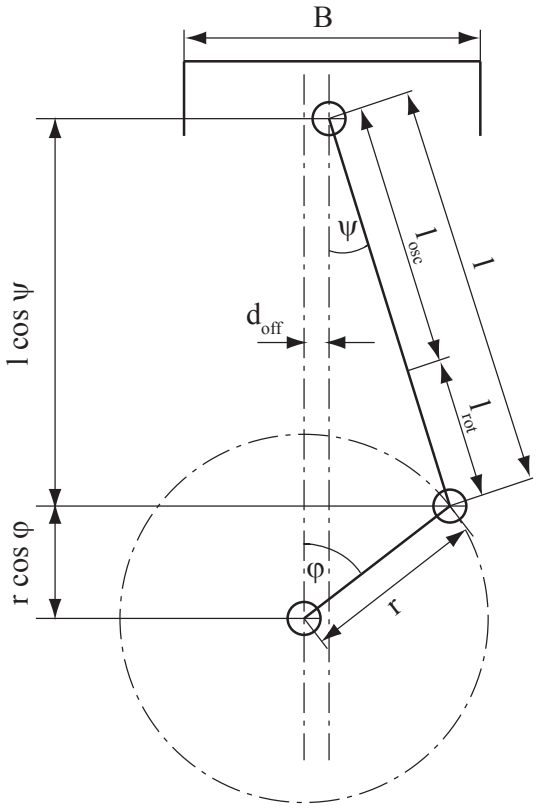

Figure 3.28.: Geometry of a crank slider mechanism with axial offset

considering the geometric relationships

$$\begin{aligned} r\ sin\ \varphi &= d + l\ cos\ \psi\ , \\ cos\ \psi &= \sqrt{1 - sin^2\psi} \end{aligned} \tag{3.107}$$

one can express the piston position as a function of crank angle φ only

$$s_P = \sqrt{(l+r)^2 - d^2} - r\ cos\ \varphi - l\sqrt{1 - (\lambda_c\ sin\ \varphi - \mu)^2}\ . \tag{3.108}$$

The normalized piston position x

$$x = \frac{s_P}{r} = \frac{1}{r}\sqrt{(l+r)^2 - d^2} -\ cos\ \varphi - \frac{1}{\lambda_c}\sqrt{1 - (\lambda_c\ sin\ \varphi - \mu)^2} \tag{3.109}$$

can be differentiated with respect to φ to yield the piston speed coefficient

$$x' = \frac{dx}{d\varphi} = sin\ \varphi + \frac{cos\ \varphi(\lambda_c\ sin\ \varphi - \mu)}{\sqrt{1-(\lambda_c\ sin\ \varphi - \mu)^2}} \tag{3.110}$$

and furthermore, the piston acceleration coefficient

$$x'' = \frac{d^2x}{d\varphi^2} = cos\ \varphi + \frac{\lambda_c\ cos\ \varphi^2 + sin\ \varphi(\mu - \lambda_c\ sin\ \varphi)(1-(\mu - \lambda_c\ sin\ \varphi)^2)}{(1-(\lambda_c\ sin\ \varphi - \mu)^2)^{3/2}}\ . \tag{3.111}$$

Now it is possible to express the instantaneous lever of F_P as

$$s_\perp(\varphi) = r\ x'(\varphi) \tag{3.112}$$

and it is thus possible to determine the torque applied to the crankshaft by the gas forces in the cylinder with Eq. (3.104).

3.10.3. Friction

The approach to describe mechanical friction in the engine implemented here, follows a model by Sandoval and Heywood [75], which itself is an improvement of a model by Patton et al. [66]. Friction losses are divided into several categories: crankshaft friction, reciprocating friction, valvetrain friction and losses from auxiliary systems. Mechanical losses result from the relative motion between solid surfaces separated by engine oil. Auxiliary component losses is the work required to drive engine accessories such as water pump, oil pump and fuel pump. The losses in the following equations are expressed as mean effective pressures in kPa.

To model influence of temperature dependency of oil the viscosity scaling in the hydrodynamic friction term is assumed to be

$$\mu_{scal} = \sqrt{\frac{\nu_{hs}(\vartheta)}{\nu_0(\vartheta_0)}}\ . \tag{3.113}$$

ν_0 is the kinematic viscosity of the oil at reference temperature $\vartheta_0 = 90\ °C$

$$\nu_0 = k\ exp\left(\frac{\theta_1}{\theta_2 + \vartheta_0}\right)\ . \tag{3.114}$$

ν_{hs} is the kinematic viscosity in the high shear range typical for oil in engine operation [75]

and is determined by

$$\nu_{hs} = \nu \, \frac{\mu_\infty}{\mu_0} \tag{3.115}$$

with the kinematic viscosity at the current oil temperature ϑ_{oil}

$$\nu = k \; exp\left(\frac{\theta_1}{\theta_2 + \vartheta_{oil}}\right) \; . \tag{3.116}$$

The parameters k, θ_1, θ_2 and $\frac{\mu_\infty}{\mu_0}$ are oil grade dependent and are provided in Tab. 3.4.

Table 3.4.: Coefficients of the oil viscosity model [75]

Oil Grade	**k in** mm^2/s	θ_1 **in °C**	θ_2 **in °C**	$\frac{\mu_\infty}{\mu_0}$
5W20	0.04576	1225	104.4	0.76
5W40	0.14	1018.74	125.91	0.8
10W30	0.1403	869.72	104.4	0.76

Crankshaft friction is then given as

$$\begin{aligned} fmep_c = 1.22 \cdot 10^5 \left(\frac{D_b}{B^2 \; 2r \; N_{cyl}}\right) + \\ 3.03 \cdot 10^{-4} \; \mu_{scal} \left(\frac{n \; D_b^3 L_b \; N_b}{B^2 \; 2r \; N_{cyl}}\right) + 1.35 \cdot 10^{-10} \left(\frac{D_b^2 \; n^2 \; N_b}{N_{cyl}}\right) \; , \end{aligned} \tag{3.117}$$

reciprocating friction with gas pressure loading

$$fmep_{r,gas} = 6.89 \frac{p_{im}}{p_0} \left(0.088 \sqrt{\mu_{scal}} \; \varepsilon + 0.182 \frac{F_t}{F_{t0}} \varepsilon^{1.33 - 0.0566 \overline{u_P}}\right) \; , \tag{3.118}$$

reciprocating friction without gas pressure loading

$$\begin{aligned} fmep_r = 294 \; \mu_{scal} \; \frac{\overline{u_P}}{B} + 4.06 \cdot 10^4 \frac{F_t}{F_{t0}} \frac{C_r}{B^2} \left(1 + \frac{500}{n}\right) + \\ 3.03 \cdot 10^{-4} \; \mu_{scal} \left(\frac{n \; D_b^3 L_b \; N_b}{B^2 \; 2r \; N_{cyl}}\right) \; , \end{aligned} \tag{3.119}$$

and valvetrain friction

$$fmep_v = 244\ \mu_{scal}\ \frac{n\ N_b}{B^2\ 2r\ N_{cyl}} + C_{ff}\left(1+\frac{500}{n}\right)\frac{N_v}{2r\ N_{cyl}} + C_{rf}\frac{n\ N_v}{2r\ N_{cyl}} + C_{oh}\ \mu_{scal}\ \frac{l_{v,max}^{1.5}\ n^{0.5} N_v}{B\ 2r\ N_{cyl}} + C_{om}\left(1+\frac{500}{n}\right)\frac{l_{v,max}\ N_v}{2r\ N_{cyl}}\ . \tag{3.120}$$

The coefficients C_i are dependent upon design of the valve train. As the engine analyzed here features a DOHC camshaft design with finger follower the coefficients are $C_{ff} = 600$, $C_{rf} = 0.0227$, $C_{oh} = 0.2$ and $C_{om} = 25.8$ [75].

Auxiliary losses are speed-dependent only

$$fmep_{aux} = 8.32 + 1.86 \cdot 10^{-3}\ n + 7.45 \cdot 10^{-3}\ n^2\ . \tag{3.121}$$

The total losses are then

$$fmep = C_{loss} \cdot (fmep_c + fmep_{r,gas} + fmep_r + fmep_v + fmep_{aux})\ . \tag{3.122}$$

C_{loss} is a model constant to fit the model to measurements.

3.10.4. Starter and Dynamometer

For start operation, a starter is installed to accelerate the engine from standstill and to generate sufficient rail pressure. It generates a torque according to a distinct power output

$$M_{starter} = \frac{P}{2\ \pi \cdot n \cdot 60\frac{s}{min}} \quad \forall n \leq n_{starter,max}$$
$$M_{starter} = 0 \quad \forall n > n_{starter,max}\ . \tag{3.123}$$

Starter torque is applied until a threshold speed $n_{starter,max}$ of 460 min^{-1} is reached, where it is disengaged. Power is set to 450 W according to the measured engine speed during cranking.

Furthermore a dynamometer is modeled in order to implement non-start operation points, e.g. for model calibration. The dynamometer is speed controlled with an ideal controller, i.e. without deviation between actual and set value.

3.11. Summary

This chapter outlines a quasi-dimensional model of a spark ignition engine sufficient to simulate cold start. The model can assist in ECU calibration of a DISI engine's cold start, i.e. to find optima in engine parameters for specific optimization criteria such as engine speed trajectory. The engine speed is chosen as the main criterion for evaluation of an individual engine start as its measurement is comparably simple and can be employed in every engine to be examined and calibrated. Therefore, its modeling is the emphasis but not the sole purpose of this model. Furthermore, variables that can not be measured, or only at very high costs[1] can be simulated e.g. pressures and temperatures in the cylinder as well as torques in the crankshaft.

The model is divided into two main parts: the thermodynamic model of the gas flows and conversions in the significant control volumes, which deliver the in-cylinder pressure and the second main part, the mechanical model of the powertrain, to enable predictions about the engine speed. The thermodynamic model comprises of the mass and energy balances of the control volumes, the gas property models, heat transfer, models of restrictions such as valves and the throttle plate, injection and combustion. The combustion model describes the turbulent premixed flame by fractal theory. To this extend, it uses information about turbulence to determine the increase in laminar flame front area. The mechanical part of the engine's model consists of a crank slider model converting the in-cylinder pressure into a torque acting on the crankshaft. Both, gas torque and torque of the starter, accelerate the engine against inertia and friction torque. In order to make predictions about the mean effective pressure of each individual cycle, a torsional behavior model is implemented in the form of a one-dimensional depiction of the crankshaft and the flywheel with individual inertias and spring-damper elements.

The models involved have such a level of complexity making a calibration with measurements necessary. This comprises the identification of optimal values for the model constants by iteratively comparing measurement and simulation results, which is described in the following chapter.

[1] A large cost in the context of ECU calibration for the cold start of a serial engine configuration.

4. Model Calibration

Stating and implementing individual models as described in Chapter 3 is necessary but not sufficient for simulating real processes by means of a gray box approach. Instead, models have to be also calibrated according to suitable measurements, i.e. model constants have to be optimally estimated to ensure the best fit of model and measurement.

This chapter starts with stating the prerequisites for successful model calibration, followed by an outline of the calibration method itself. It continues with the description of the calibration of the individual models.

4.1. Prerequisites

Since the models have a certain degree of simplification, calibration is needed to ensure a maximum validity to the process to be modeled, i.e. to achieve the best fit between simulation and experimental data by estimating the model constants. Model constants cover real process effects that are not or only insufficiently described by the models.

Based on statements by Schulze [81] certain prerequisites are presented that are necessary for a successful calibration:

- *Experiments shall be reproducible.* There are different gradations of stochastic behavior of real processes. In terms of engine design, an example for a low variation is the in-cylinder pressure during a complete cycle without combustion. If, however, combustion takes place, in-cylinder pressure is affected by the course of combustion. Combustion itself is strongly dependent upon local flow field and upon local fuel distribution especially during combustion initiation. This leads to a comparably high variation.

For the first case a single measurement can be sufficient, whereas the second example requires averaging of many working cycles because an individual cycle is not representative due to the aforementioned cyclic variations.

- *Boundary conditions shall be as complex as necessary only* to reduce undesirable effects as e.g. the influence of capacities.
- *Measurement frequency and resolution have to be high enough to ensure detection of all significant effects.*
- *Experiments shall be employed in a way as to allow for calibration of as few model constants individually as possible.* This not only reduces the uncertainties in the calibration process, hence reducing the restriction of validity to very specific conditions, but also decreases the necessary computing effort during optimization.

4.2. Optimization Algorithm

One of the standard methods to fit model to measurements is the least squares method [24], which is also used in this context. Let y_i be the experimental data at each data point i for m observations and t_i the points in time

$$y_i = y(t_i), \quad i = 1, ..., m \; . \tag{4.1}$$

ϕ_i is the corresponding simulation data

$$\phi_i = \phi(t_i, \mathbf{\Theta}), \quad i = 1, ..., m \tag{4.2}$$

with $\mathbf{\Theta}$ as the model constants to be identified. With the residuals being the difference between observation and model data

$$r_i = y_i - \phi_i \tag{4.3}$$

one can express the least squares and weighted least squares as

$$g(\mathbf{\Theta}) = \|r\|^2 = \sum_{1}^{m} r_i^2 \tag{4.4}$$

and

$$g(\mathbf{\Theta}) = \|r\|_w^2 = \sum_1^m w_i \, r_i^2 \; . \tag{4.5}$$

Weighted least squares is applied when more than one objective has to be satisfied.

With the aim to minimize the squared residuals between experimental data and the mathematical model, a global optimization problem can now be stated as

$$\min_{\mathbf{\Theta}} \; g(\mathbf{\Theta}) \tag{4.6}$$

with $g(\mathbf{\Theta})$ as the objective or loss function.

Since the equation system of the residuals can not be solved directly, a numerical optimization determines the approximate solution by an optimum seeking algorithm. Fig. 4.1 shows the iterative optimization process of computing successive simulation runs with a certain parameter set and comparing the result with measurement data.

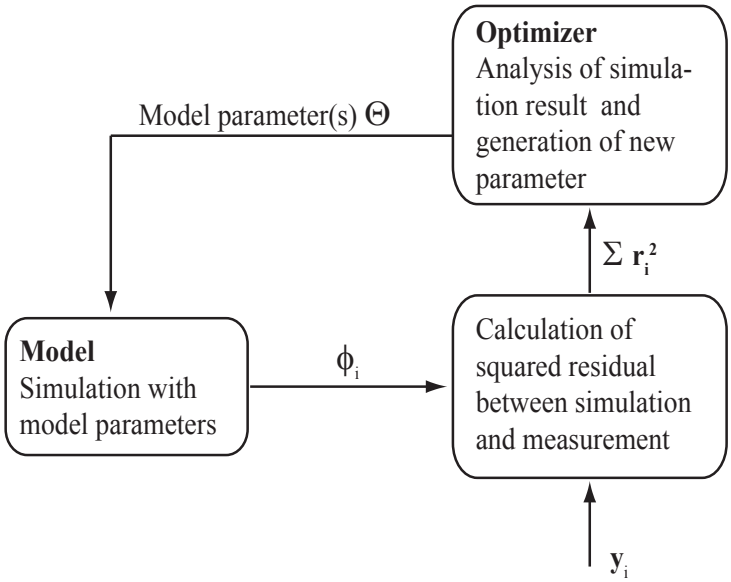

Figure 4.1.: Iterative optimization process with measurement data y_i, model data ϕ_i and model parameters $\mathbf{\Theta}$. The squared residuals $\sum r_i^2$ are to be minimized by the optimization algorithm for a best fit of the model to measurement data.

Optimization is of iterative nature. Therefore, computing time is a limiting factor and as such, it is advisable to reduce the number of model parameters as much as possible. This lessens the so-called "curse of dimensionality" [64] where the computing effort increases exponentially with the number of parameter space dimensions. Nevertheless, some models have to be calibrated holistically due to a interaction of the submodels. Consequently more than one parameter has to be identified simultaneously. This circumstance requires an optimization algorithm capable of finding global optima in n-dimensional search spaces, namely, metaheuristical optimization approaches.

Metaheuristical optimization methods are derivative free and contain stochastic terms allowing them to escape local minima and reducing the necessity to restart the optimization from different starting positions. The main advantage, compared to non-heuristical approaches is the 100 % likelihood to find the global minimum[1], which is not the case for e.g. gradient based methods [64]. Metaheuristical algorithms are among others Genetic Algorithms, Tabu Search, Particle Swarm Method and Simulated Annealing.

Here the Simulated Annealing algorithm by Kirkpatrick et al. [45] is used. It emulates the cool down of metals with phase change from liquid to solid. Different cooling scenarios are possible. If cooling-down is fast, atoms can not move into positions with minimal energy, which results in unfavorable stress within the material. This expresses a local minimum in stored energy only. For this reason, annealing is applied in metallurgy, which means that metal is reheated and cooled down slowly. In this case metal ions "have enough time" to reach the minimal energy state.

In analogy to the temperature in the real process, in algorithm terms a stochastic parameter T is introduced characterizing the probability of the acceptance of a parameter set less fit than a previous one. This temperatures decreases over the iterations according to a predefined cooling schedule. A high temperature implies a high probability for acceptance of a less fit candidate - likewise to the real process, where a higher temperature means a higher kinetic energy of the atoms which reduces the likelihood for them to get stuck in unfavorable places regarding bound energy. As temperature lowers, the stochastic term plays a lesser role and the function value's importance increases in deciding over acceptance

[1] Presuming an infinitely slow cool down.

or rejection.

The algorithm can be stated as:

0. Choose $\mathbf{\Theta}_0$ and $T_0 \in [0, \infty]$, set k = 0. Calculate loss function $g(\mathbf{\Theta}_k)$.

1. Generate a candidate $\mathbf{\Theta}_{k+1}$ according to a probability distribution R. Calculate $g(\mathbf{\Theta}_{k+1})$.

2. If $g(\mathbf{\Theta}_{k+1}) \leq g(\mathbf{\Theta}_k)$, accept $\mathbf{\Theta}_{k+1}$ as new iteration point and return to step 1. If $g(\mathbf{\Theta}_{k+1}) > g(\mathbf{\Theta}_k)$, accept $\mathbf{\Theta}_{k+1}$ with probability $P(\Delta g) = exp\left(\frac{\Delta g}{k_B\, T}\right)$ with $\Delta g = g(\mathbf{\Theta}_k) - g(\mathbf{\Theta}_{k+1})$ else retain $\mathbf{\Theta}_k$. Set $T_{k+1} = 0.8\, T_k$.

3. Test for termination criterion and stop or increment k and return to step 1.

Since the Boltzmann constant k_B is scaling the arbitrary temperature only, it is set to unity. The probability function P is compared to a random number between 0 and 1 to decide over acceptance or rejection of the candidate. Optimization is stopped when a threshold temperature or threshold value of the objective function is reached.

Certain properties have to be adjusted according to the optimization problem at hand:

- Initial and final temperatures,
- starting values, lower and upper boundaries,
- cooling schedule, here a geometric series, e. g. $T_i = 0.8\, T_{i-1}$, this depends strongly on the optimization problem,
- maximum number of function evaluations per temperature step,
- candidate generation, e. g. a normal distribution with a range according to the set lower and upper boundaries.

Experience proves the algorithm to be efficient and reliable in finding the global optimum of a given problem. Furthermore, apart from model calibration, this algorithm can be applied to optimize the process to be modeled itself, i. e. the engine operation.

4.3. Submodel Calibration

Turbulence Model

The function of the turbulence model is to determine the fluctuating part of the flow field u' as presented in Sec. 3.6. Measurements of fluctuating velocity were not available. As a compromise the turbulence model is calibrated to 3D-CFD simulations of the engine for a fixed engine speed of 1500 min^{-1}, a manifold pressure of 1 bar and an intake cam shift of $-20°$, which constitutes a typical engine start operation point. Although the applied CFD method, RANS with a k-ε-model, models turbulence only empirically, it is widely accepted to be accurate. Fluctuating velocity is averaged over the three space directions and compared to values computed by the zero-dimensional turbulence model. Free model constants are the dissipation constant C_β and the scaling factor for fluctuating velocity component $C_{u'}$ which are identified to be 2 and 0.5 respectively.

Fig. 4.2 shows the comparison of both models during intake and compression stroke. During the intake stroke a phase shift of the peak is obvious which can be attributed to the zero-dimensional modeling approach. Neglecting spacial resolution, the model still shows its potential.

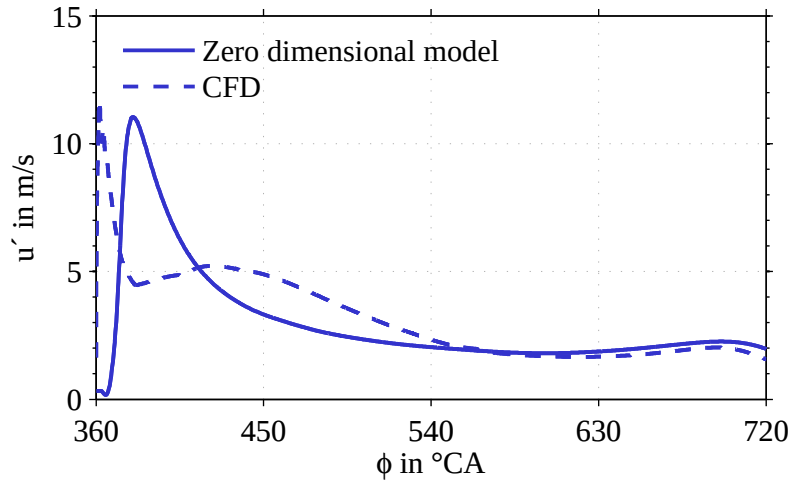

Figure 4.2.: Fluctuating component of the in-cylinder velocity at n = 1500 min^{-1}

Gas Exchange Model

The quantity of primary interest determined by the gas exchange model is the amount of trapped mass of fresh air expressed as volumetric efficiency, see Sec. 3.2.2. It is important due to the direct relationship of indicated mean effective pressure to air mass in the cylinder considering a constant relative equivalence ratio. The volumetric efficiency depends upon several factors. One example being the heat transfer to and from the walls in the plenums as well as in the cylinders during intake stroke. These are functions of both heat transfer coefficients and wall temperatures and are covered by the respective heat transfer models. A higher heat transfer into the gas during intake causes the temperature of the gas to increase with the corresponding decrease in density and, therefore, lower volumetric efficiency. A similar effect on the volumetric efficiency is induced by the amount and the effective properties of residual gas dependent on the character of intake stroke, mixture formation and combustion of the preceding cycle. Like a high heat transfer, a high EGR rate and a high temperature lead to decreased volumetric efficiency due to similar effects. These effects, heat transfer and residual gas, shall not be subject to calibration because, firstly, neither can be directly quantified by given measurements and, secondly, it would furthermore imply a considerably higher number of free model constants.

Apart from operational parameters, geometric ones also have a strong effect on the gas exchange. Geometry is represented in the model by the volume of the intake manifold, the throttle plate diameter as well as the intake and exhaust valve diameters, discharge coefficients and valve timings. Discharge coefficients are gathered from literature as mentioned in Sec. 3.3.2. Valve diameters and timings are given by engine data, phase shift of the intake camshaft is defined by the engine run information. This leaves intake manifold volume V_{im}, throttle plate diameter D_{th} and discharge coefficient offset $C_{d,offset}$ as free parameters of the gas exchange model.

Contrary to the cold start simulation, the calibration of the gas exchange model is set up with the complete engine model on a dynamometer test bench with speed, spark timing, intake cam shift and throttle position as inputs obtained from a dynamic measurement for a fully warmed up engine, Fig. 4.3. It shall be noted that a comparison with cold start measurements is possible but does not yield valuable results as the volumetric efficiency

calculation of the engine control unit is not precise during start. Hence, operation points with a warmed up engine are used.

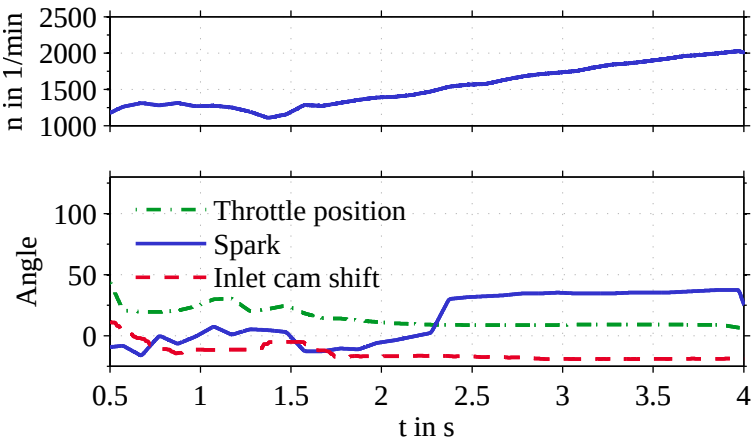

Figure 4.3.: Input parameters of the gas exchange model calibration for a warmed-up dynamic engine operation

The result of the simulation with the identified parameters $V_{im} = 2000$ cm^3, $D_{th} = 30$ mm and $C_{d,offset} = 0.5 \cdot 10^{-5}$, namely, manifold pressure p_{im} and volumetric efficiency λ_V, is compared with measurement values in Fig. 4.4. Intake manifold pressure of the simulation shows the typical fluctuating trace due to the intake strokes of the individual cylinders. A sufficient agreement between measurement and simulation for this dynamic operation is achieved.

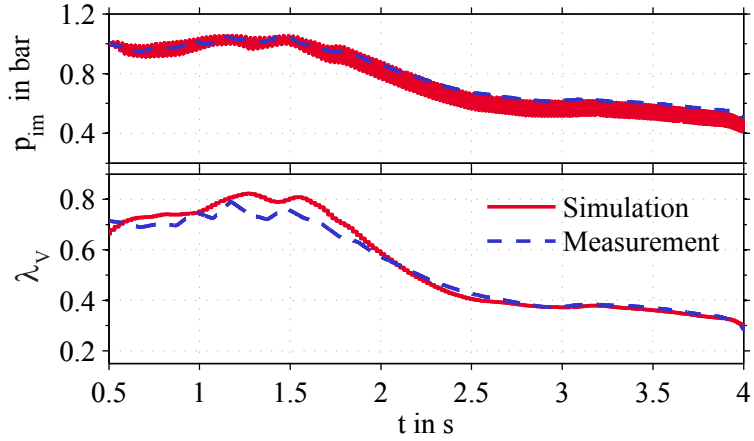

Figure 4.4.: Results of the gas exchange model calibration

Leakage Model

The leakage model as described in Sec. 3.3.3 determines the mass flow and the enthalpy flow across the piston rings. It is calibrated via a pressure trace of the motored operation during cold start. Fig. 4.5 shows the comparison of in-cylinder pressure data with the simulation result of the engine model and a calculation of an ideal case of a closed volume with adiabatic walls.

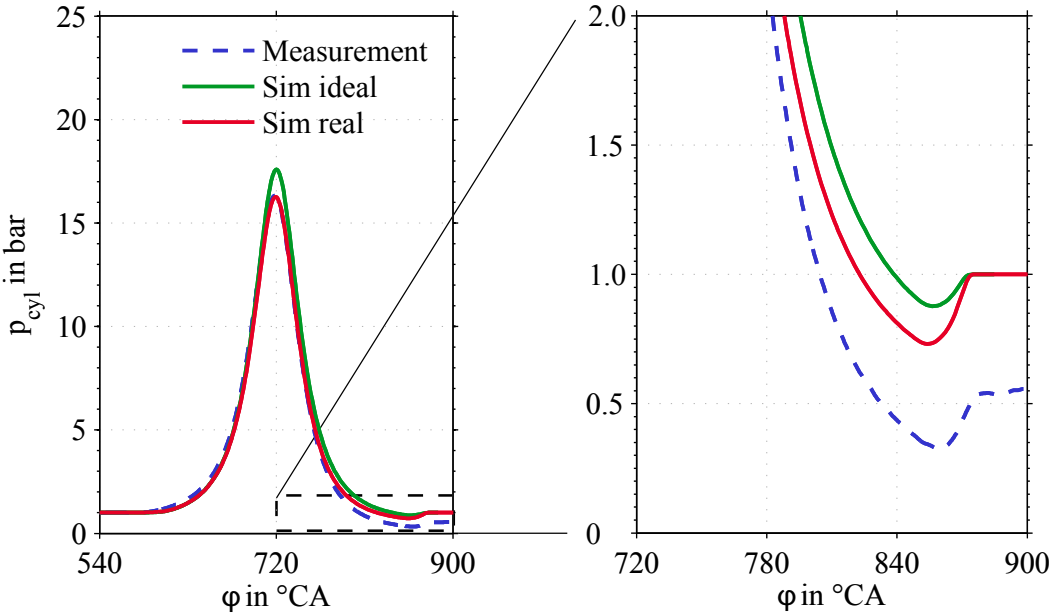

Figure 4.5.: In-cylinder pressure during motored part of engine start with n = 200 min^{-1}, ideal simulation case with a closed control volume and adiabatic walls, real simulation takes leakage and heat loss into account

It is obvious that during expansion a pressure drop below ambient conditions occurs. This is caused by three effects. Two of them are losses in inner energy due to heat transfer to the walls and the leakage across the piston rings. The last effect is caused by an intake valve closing that is too late for very low engine speeds. An ejection of air during the compression stroke thus leads to a late effective compression start and in return to an effectively extended expansion. This can be studied at the closed-volume, adiabatic walls case in Fig. 4.5 where a pressure drop below ambient condition occurs also.

A further pressure deviation between measurement and calibrated simulation is caused by

the measuring principle applied. Since the pressure indicators are of the piezoelectric principle, they only detect changes in pressure and have to be recalibrated every cycle to compensate for occurring zero shift. This deviation is amplified while motoring with low engine speed, which is visible in the pressure trace, Fig. 4.5. To enable a comparison between measurement and simulation, the pressure trace of the measurement is offset to a reasonable value of exhaust pressure during open exhaust valve, Fig. 4.6. This in turn makes calibration of the free parameters C_{leak} and n_{leak} of the leakage model possible. Identified values of the two constants are $0.5 \cdot 10^{-7}$ m and 0.4 respectively.

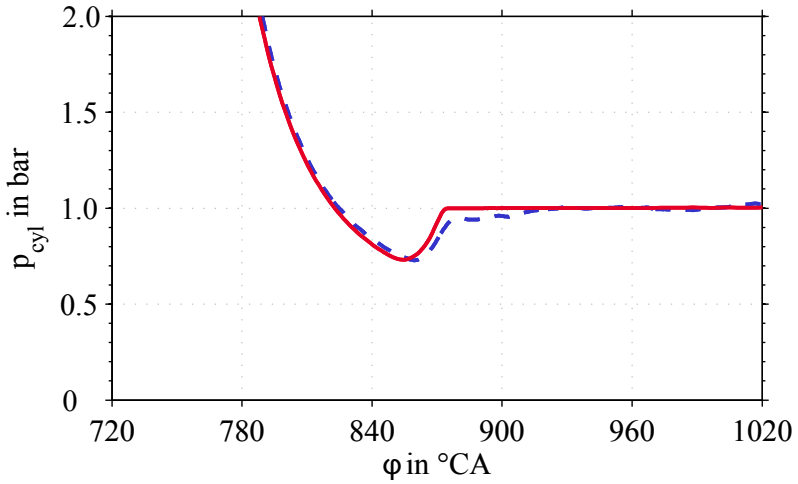

Figure 4.6.: In-cylinder pressure for the calibrated leakage model compared to offset measured pressure

Combustion Model

Combustion is modeled via the fractal combustion model introduced in Sec. 3.4. Model constants are C_{ign} for the ignition delay model and the constant for scaling the outer cutoff scale C_l of the turbulent flame propagation model. Measurement data for calibrating the combustion model is obtained at stationary engine operation, characterized by engine speed and volumetric efficiency. The reasoning is that during stationary operation, boundary conditions for combustion can be determined exactly, contrary to the cold start where equivalence ratio and volumetric efficiency measurement are imprecise. Therefore, the intake pressure is adjusted to fit the air mass in the cylinder of the simulation to that of the measurement in order to eliminate the influence of cylinder charge on the result of the combustion model.

Especially the indicated mean effective pressure is dependent upon volumetric efficiency.

Here, the calibration criterion is the heat release characterized by the burnt mass fractions 5 %, 50 % and 90 %. The calibration of the combustion models yields values of $C_{ign} = 1.5$ and $C_l = 0.32$, the result is shown in Fig. 4.7. In general, a satisfactory agreement is evident that supports the flexibility of the modeling approach described in literature [14]. An exception is the retarded spark timing for the high load cases where a larger deviation can be observed. This can possibly be attributed to the ignition model, which is not as mature as the fractal combustion model.

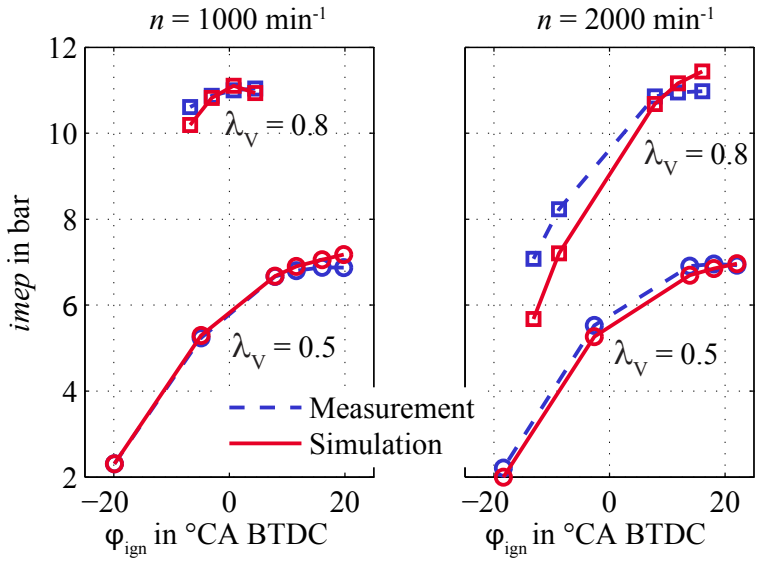

Figure 4.7.: Results of combustion model calibration for $C_{ign} = 1.5$ and $C_l = 0.32$, *imep* for spark timing variation at stationary engine operation with engine speed n and volumetric efficiency λ_V

It has to be noted that a two stage approach for calibration of the combustion model is employed. Due to the large size of the complete engine model, runtime is long compared to a single cylinder model. Hence, an initial calibration of a single cylinder model is performed to obtain "good" starting values for the second run with the complete engine model. This gives rise to the opportunity to reduce the stochastic term of the optimization algorithm for the complete engine model, see Sec. 4.2, therefore enhancing the local search of the algorithm and minimizing the required optimization iterations.

Friction Model

The friction model is calibrated against the same operation points as the combustion model. The result with a model constant value of $C_{loss} = 1.18$ is depicted in Fig 4.8. A good agreement is obvious for the higher loads in both speed cases. The discrepancy in the low load cases can not be explained directly. Sandoval and Heywood [75] validated the friction model against engine speed variation measurements. Consequently it is not clear whether the model is valid for spark variations. On the other hand discrepancies of the order of 10 % in friction mean effective pressure, as is the case here, have an effect of about 2 % in the calculation of break mean effective pressure. In conclusion, it can be noted that the friction model is sufficient for determining break mean effective pressure from indicated mean effective pressure for an engine cold start.

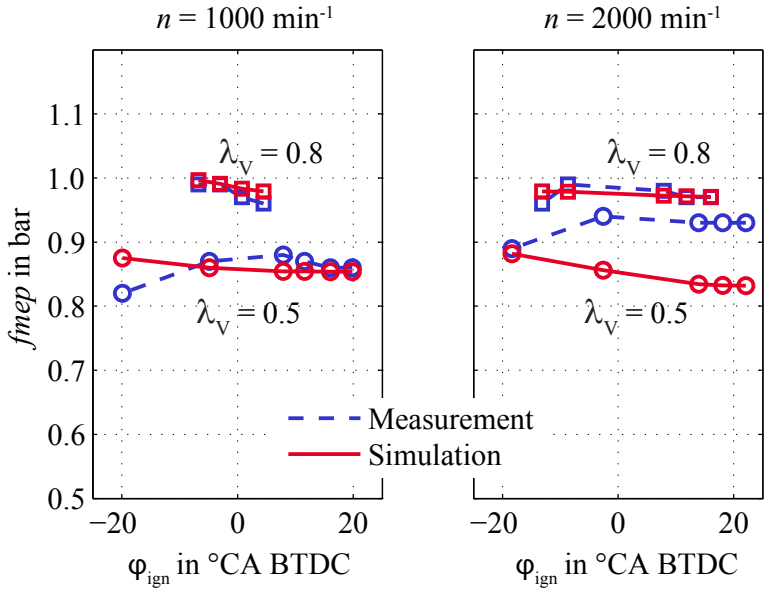

Figure 4.8.: Results of loss model calibration for $C_{loss} = 1.18$, friction mean effective pressure *fmep* for a spark timing variation at stationary engine operation with engine speed n and volumetric efficiency λ_V

Mechanical Power Transmission Model

The parameters of the crankshaft model - moments of inertia, spring and damper constants, Sec. 3.10.1 - are dependent upon geometry and material of the individual components of the crankshaft and flywheel compound. These properties can be calculated by FEM requiring

knowledge about the exact geometry. Since this data was not available and is often not available for the ECU calibration procedure in general, both during model development and during use by the application engineer, a more practical approach is used. The parameters are considered to be free model constants, which can be fitted to measurement data. Therefore, the mechanical model is instanced individually with cylinder pressures from measurement as input and measured engine speed as reference. Calibration yields the values shown in Tab. 4.1. It is apparent that the stiffness constants of the cranks are of magnitudes higher than the stiffness constant of the flywheel. This is in line with the intended isolation of engine and output side of the crankshaft at moderate to high engine speeds. A low stiffness leads to a low resonance frequency and isolation of the two parts at higher engine speeds.

Table 4.1.: Constants of the mechanical model

Parameter	**Unit**	**Value**
$c_{1,2}...c_{3,4}$	$^{\mathrm{Nm}}/_{\mathrm{rad}}$	489000
$b_{1,2}...b_{3,4}$	$^{\mathrm{Nms}}/_{\mathrm{rad}}$	0.1
$c_{4,F}$	$^{\mathrm{Nm}}/_{\mathrm{rad}}$	586000
$b_{4,F}$	$^{\mathrm{Nms}}/_{\mathrm{rad}}$	0.6
c_F	$^{\mathrm{Nm}}/_{\mathrm{rad}}$	213.79
b_F	$^{\mathrm{Nms}}/_{\mathrm{rad}}$	2.44
I_{aux}	kgm^2	0.02449
$I_{rot,1}...I_{rot,4}$	kgm^2	0.02817
$I_{F,prim}$	kgm^2	0.087971
$I_{F,sec}$	kgm^2	0.040729

Fig. 4.9 shows a comparison of the best fits for the models with single-mass and two-mass flywheel. The general trend of the speed trace is captured even with the single-mass flywheel. However, if the individual working cycles have to be assessed, the deviations between simulation and measurement tend to be too high. This is why a discretization of the flywheel is applied, see Fig. 4.9(b). Despite the simple model of the flywheel, two masses connected by a spring-damper element with constant stiffness and damping coefficients, the agreement is sufficient e.g. for drawing conclusions about the indicated mean effective pressure from measured engine speed.

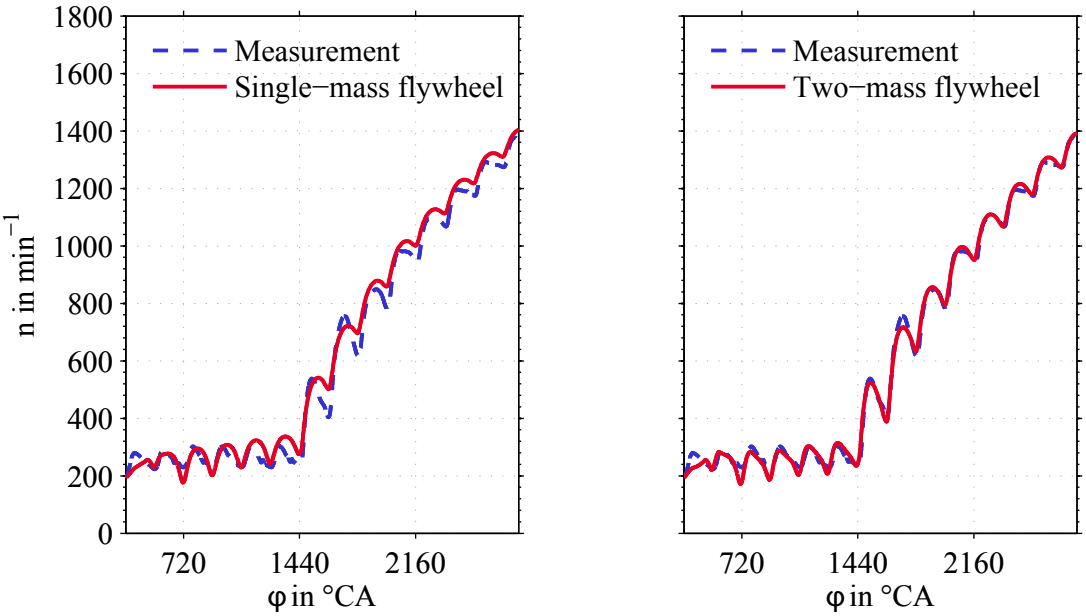

Figure 4.9.: Result of the power transmission model, (a) single-mass flywheel, (b) two-mass flywheel

4.4. Summary

Model constants are calibrated against appropriate measurements by an optimization algorithm, which minimizes the squared residuals between experimental and simulation data. A Simulated Annealing algorithm is used to increase the likelihood of locating the global optimum of the parameter space investigated, compared to more traditional optimization approaches. Submodels are calibrated individually wherever possible to minimize optimiza-

tion effort and to reduce uncertainties. A good agreement is achieved for the models at the applied boundary conditions. Finally Tab. 4.2 summarizes the values of the model constants.

Table 4.2.: Overview of the model constants

Submodel	**Parameter**	**Value**
Turbulence model	C_{β}	2
	$C_{u'}$	0.5
Gas exchange model	D_{th}	30 mm
	V_{man}	2000 cm^3
	$C_{d,offset}$	$0.5 \cdot 10^{-5}$
Leakage model	C_{leak}	$0.5 \cdot 10^{-7}$
	n_{leak}	0.4
Combustion model	C_{ign}	1.5
	C_{l}	0.32
Friction model	C_{loss}	1.18

In summary, the amount of free parameters still offers relatively simple carry-over to other engines. Calibration is fast, compared to implementing new engine geometry meshes as with CFD methods. Suitable measurements serving as a basis, parameter variations and optimization can be carried out as shown in the next chapter.

5. Application of the Cold Start Model

The previous chapters exemplified how an engine cold start model can be established and calibrated against measurements. Consequently, the present chapter shall evaluate the benefits to the understanding of the engine operation in general and to the engine calibration in particular by the application of this model. The first part consists of a parameter variation of boundary conditions on the one hand and engine operation and geometry parameters on the other. It is followed by a parameter optimization of the engine operation parameters and finally by statements about the measurement evaluation, i.e. the increase of information yield from given experimental data.

5.1. Parameter Variation

Parameter variations can be used to enhance the understanding of the process to be modeled regarding boundary conditions. Furthermore, information about effects of certain engine operation parameters can be gained that otherwise would be difficult to examine. This makes the investigation of the interrelationships of different parameters possible.
If not stated otherwise, the engine operation parameters for the following parameter variations are as given in Tab. 5.1 with ambient pressure p_{amb}, ambient temperature T_{amb}, throttle plate angle α_{th}, spark timing φ_{ign}, end of injection φ_{eoi}, intake valve shift $\Delta\varphi_{ivo}$ and exhaust valve shift $\Delta\varphi_{evo}$.
The throttle angle is represented by a relative angle where 0 % represents a closed throttle plate and 100 % a fully opened one. The relative throttle plate angle α_{th} is ramped down during start to simulate a real engine operation, Fig. 5.1(a). This is done to limit speed overshoot since the targeted idle speed is about 700...800 min^{-1} and a wide open throttle would lead to very high engine speeds.

Table 5.1.: Reference operation parameters

Parameter	p_{amb}	T_{amb}	α_{th}	φ_{ign}	φ_{eoi}	$\Delta\varphi_{ivo}$	$\Delta\varphi_{evo}$	λ
Unit	mbar	°C	%	°CA BTDC	°CA BTDC	°CA	°CA	-
Value	1013	20	14	0	65	0	0	1

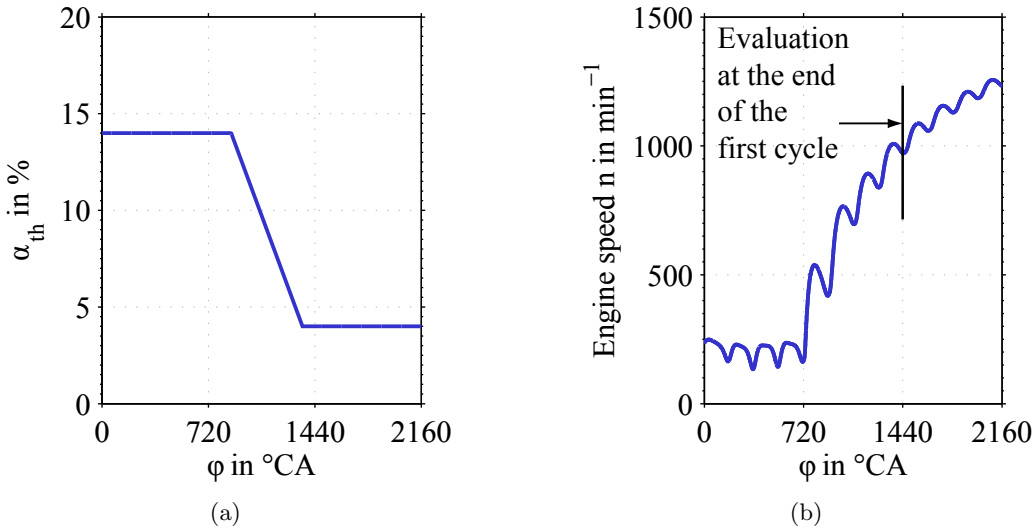

Figure 5.1.: Boundary conditions for start evaluation, (a) relative throttle angle α_{th} during parameter variations, (b) instant of evaluation at the end of the first complete engine cycle

Several variables are used to evaluate the cold start quality: volumetric efficiency λ_V to assess the gas exchange, indicated mean effective pressure *imep* for the quality of combustion and the engine speed n for the overall response of the engine to the given engine parameters. Fig. 5.1(b) marks the instance of evaluation of these quantities after the first engine cycle.

5.1.1. Compression Ratio

The compression ratio of a reciprocating internal combustion engine is defined as the ratio of compression volume to the total cylinder volume

$$\varepsilon = \frac{V_c}{V_d + V_c} \tag{5.1}$$

and is a major engine geometry parameter concerning efficiency and the occurrence of knock phenomena. Fig. 5.2 shows the result of a compression ratio variation from 8 to 12 for in-cylinder pressure and engine speed during cold start. As one would expect, an increase in compression ratio increases the in-cylinder pressure rise during combustion, which in turn causes a higher indicated mean effective pressure for a given volumetric efficiency and spark timing. This results in a higher engine speed gradient, Fig. 5.3(b). The difference in engine speed at $\varphi = 1440$ °CA sums to 19 min^{-1}. Two effects counteract each other with compression ratio variation regarding engine speed. An increased compression ratio increases indicated mean effective pressure during the fired cycles and therefore the speed gradient during this phase. However, it also increases the pressure-volume work to be delivered by the starter lowering the initial speed for the first combustion. This fact has to be taken into account to ensure a minimum engine speed during cranking phase.

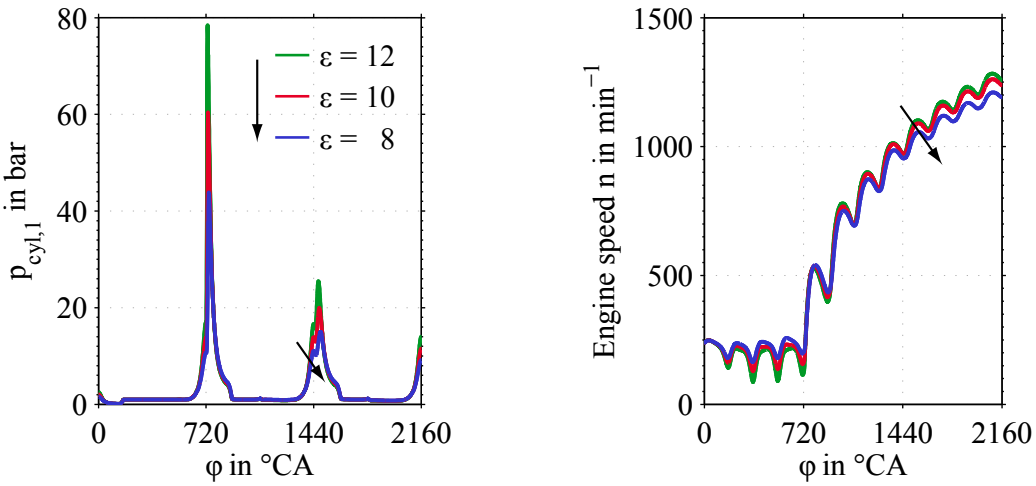

Figure 5.2.: Compression ratio variation, (a) depicts the in-cylinder pressure of the first cylinder, (b) the resulting engine speed with a lower minimal speed during cranking for the high compression ratio

5.1.2. Flywheel

The effects of several parameters of the flywheel model can be studied, as shown in Sec. 3.10.1. As an example, a variation in flywheel inertia is depicted in Fig. 5.3. A reduction in flywheel inertia increases the speed gradient as well as other transient operation as this measure de-

creases the necessary kinetic energy per speed increment. An unduly reduction of inertia is, however, not advisable as the isolation between engine and output side is hampered. This results in higher vibrational amplitudes and frequencies and is therefore to be avoided. A high inertia on the other hand enhances the isolation but worsens the transient behavior of the engine.

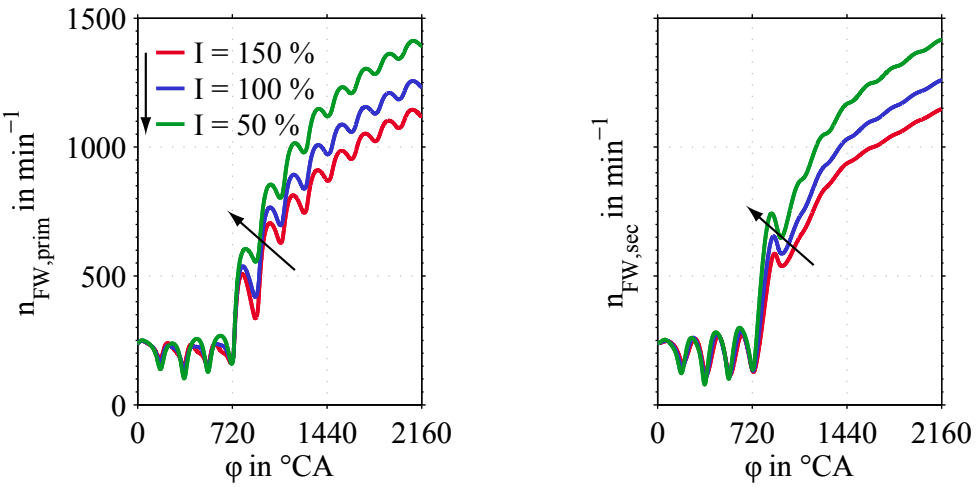

Figure 5.3.: Flywheel inertia variation, (a) speed of the primary mass of the flywheel, (b) speed of the secondary mass

5.1.3. Number of Cylinders

Based on the engine models structure, easy variations of geometry parameters as shown in the preceding sections are possible. This can be extended to the number of installed cylinders as well. Fig. 5.4 depicts the cold start for a variation of cylinder number with the speed at the primary mass of the flywheel, Fig. 5.4(a), and the speed at the secondary mass, Fig. 5.4(b). Here the total mass of the flywheel is kept constant, the mass of the crankshaft is increased according to the number of cylinders.

The speed traces appear to be very similar for the 4- and 6-cylinder engines which is due to a comparable relative mass of the flywheel to be accelerated on the one hand and a sufficient isolation of primary and secondary mass for the speed range in question on the other. The three- and especially the two-cylinder engines, however, exhibit a more critical behavior

as the oscillation at the secondary side of the flywheel and their feedback to the primary mass are more severe. Additionally, the relatively higher mass of the flywheel decreases the speed gradient. A separate optimization of flywheel geometry would have to be carried out. Nonetheless, the low-cylinder-number engines are more prone to critical operation regimes, e.g. a two-cylinder engine could not as easily compensate a low quality combustion during cold start as a four-cylinder engine.

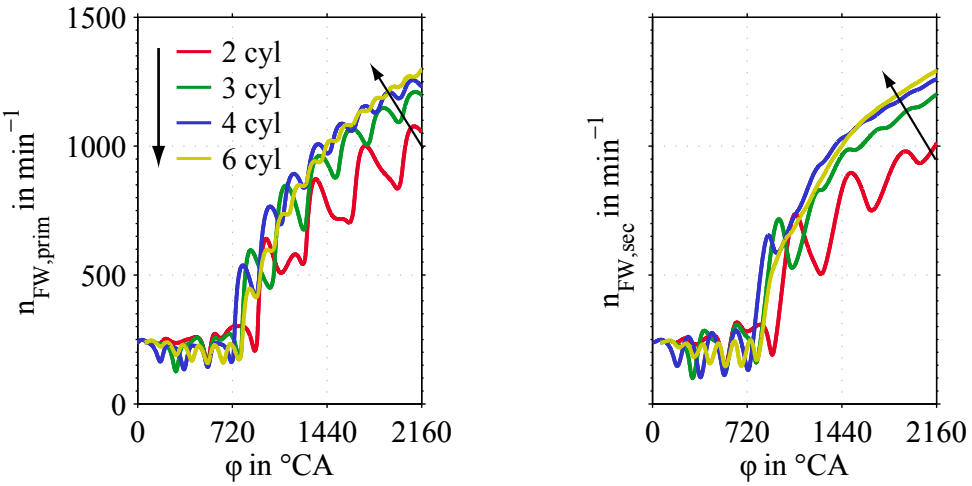

Figure 5.4.: Cylinder number variation, (a) speed of the primary mass of the flywheel, (b) speed of the secondary mass

5.1.4. Ambient Pressure

Altitude represents a challenge in engine operation since ambient pressure declines with height. This reduces the effective in-cylinder air mass and therefore can be detrimental to starting performance.

A standardized model that describes the tropospheric pressure change is outlined in ISO 2533:1975 Standard Atmosphere [1]:

$$p_{amb} = p_0 \left(1 - \frac{0.0065\ h}{288.15}\right)^{5.255} \tag{5.2}$$

with h as the height above sea level in m and p_0 as the standard pressure of 1013.25 mbar. The model incorporates the temperature influence as the temperature in the troposphere

decreases also with height. Fig. 5.5 shows the correlation of ambient pressure and height above sea level.

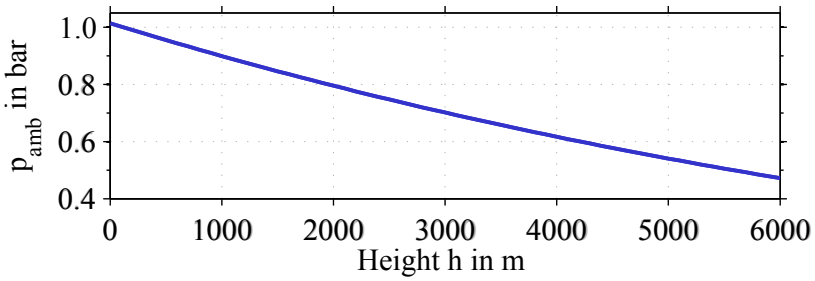

Figure 5.5.: Norm atmospheric pressure in regard to height above sea level [1]

The effect of reduced pressure on cold start performance is shown in Fig. 5.6. A variation of ambient pressure corresponding to 0, 1000, 2000 and 3000 m is carried out respectively. A reduced ambient pressure causes the volumetric efficiency to be lower and as a result, indicated mean effective pressure and engine speed to be lower as well. Apparent is the speed difference of 216 min^{-1} at $\varphi = 1440$ °CA. This reduced engine speed can mean difficulties in maintaining a cold start if one or several poor combustions occur as it is more likely that the engine speed reaches zero.

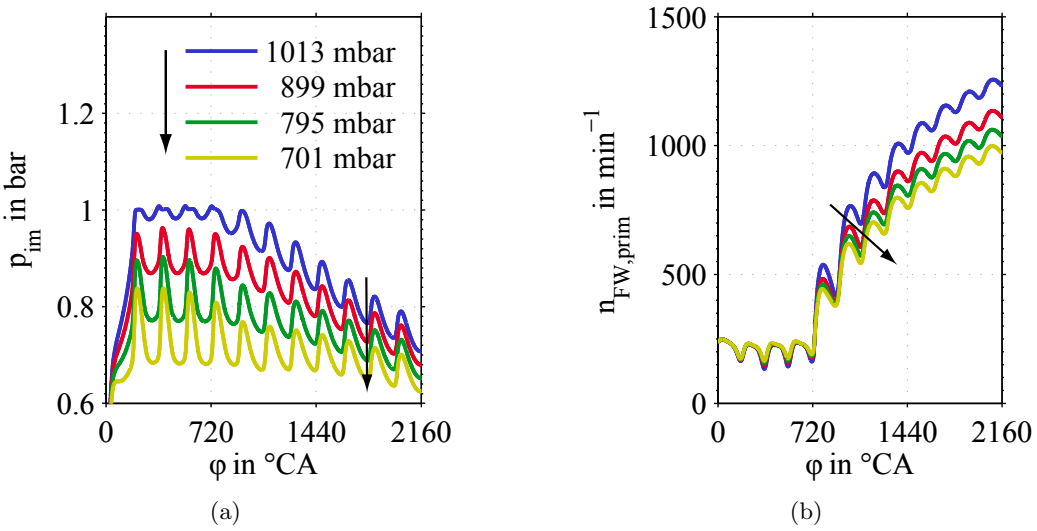

Figure 5.6.: Influence of ambient pressure on start performance, (a) intake manifold pressure, (b) engine speed

To compensate for a reduced ambient pressure, the throttle plate has to be opened further to reduce flow resistance. Fig. 5.7 presents the mean volumetric efficiency during the first fired cycle for a simultaneous variation of ambient pressure and throttle angle. At ambient pressures around 1000 mbar a positive relationship between throttle angle and volumetric efficiency can be observed in the range of $\alpha_{th} = 4...14$ %. Any further increase in throttle angle affects volumetric efficiency barely, because engine speed is so low that a small free area hardly impedes the air mass flow. What is noteworthy, however, is the nearly nonexistent influence of throttle angle on the volumetric efficiency with low ambient pressures.

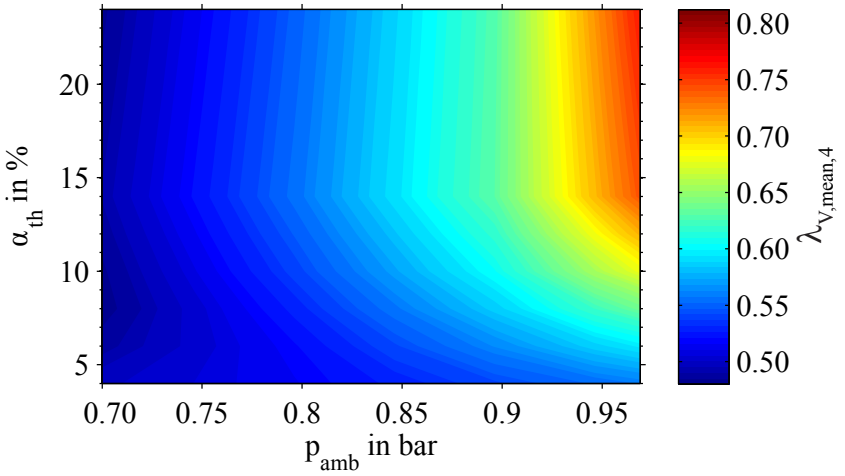

Figure 5.7.: Mean volumetric efficiency of the first fired cycle $\lambda_{V,mean,4}$ as a function of ambient pressure p_{amb} and relative throttle angle α_{th}

5.1.5. Ambient Temperature

Ambient temperature has a major effect on cold start performance of an SI engine due to the challenge arising from the problematic mixture preparation with low temperatures as described in Sec. 1. Since mixture formation is modeled by a simple model only, the analysis of ambient temperature is restricted to the variation of volumetric efficiency. The result of different ambient temperatures on volumetric efficiency and engine speed is depicted in Fig. 5.8.

A lower ambient temperature causes a higher volumetric efficiency as stated by the thermal equation of state, Eq. (3.3). The difference amounts to 0.04 or 5 % for a variation from -20 °C to 20 °C. The sensitivity of volumetric efficiency to ambient temperature might

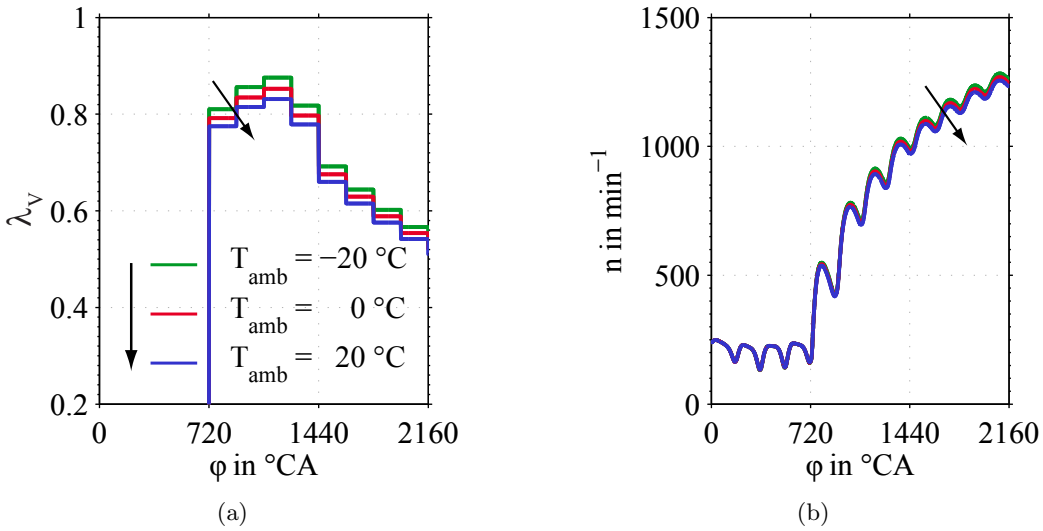

Figure 5.8.: Influence of ambient temperature on start performance, (a) volumetric efficiency, (b) engine speed

not be high but can have a significant effect on cold start strategy as a higher air mass means a higher amount of fuel to be evaporated in order to achieve a combustible mixture accompanied by lower available enthalpy. Hence, a throttling at very low temperatures can help in reducing the necessary amount of fuel to evaporate. Fig. 5.9 shows the results of an investigation concerning influence of throttle angle and ambient temperature on volumetric efficiency. With this map it is possible to determine the required throttle angle for a given volumetric efficiency value for all ambient temperatures in question.

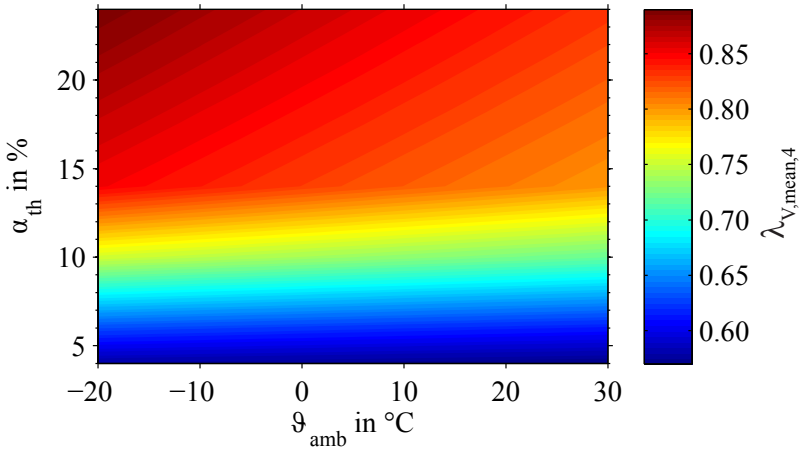

Figure 5.9.: Mean volumetric efficiency of the first fired cycle $\lambda_{V,mean,4}$ as a function of ambient temperature ϑ_{amb} and relative throttle angle α_{th}

5.1.6. Valve Phase Shift

Valve timings have a strong impact on gas exchange and therefore on engine performance. Both intake and exhaust valve timings are examined to show the potential impact on engine starting behavior.

Intake valve phase shift influences the volumetric efficiency dependent upon engine speed. At high engine speeds a late intake valve timing is advisable to increase the air mass entering the cylinder by taking advantage of fluid dynamic effects. At low engine speeds, however, a late intake valve closing does not prevent the freshly aspirated air to leave the cylinder again during compression stroke. Apparently, a speed specific timing optimum in regard to maximum volumetric efficiency can be identified. Fig. 5.10 shows the effect of an intake valve phase shift variation on cylinder pressure at stationary operation with $n = 1000$ min^{-1}. A later timing lowers the volumetric efficiency and therefore reduces the in-cylinder pressure and indicated mean effective pressure.

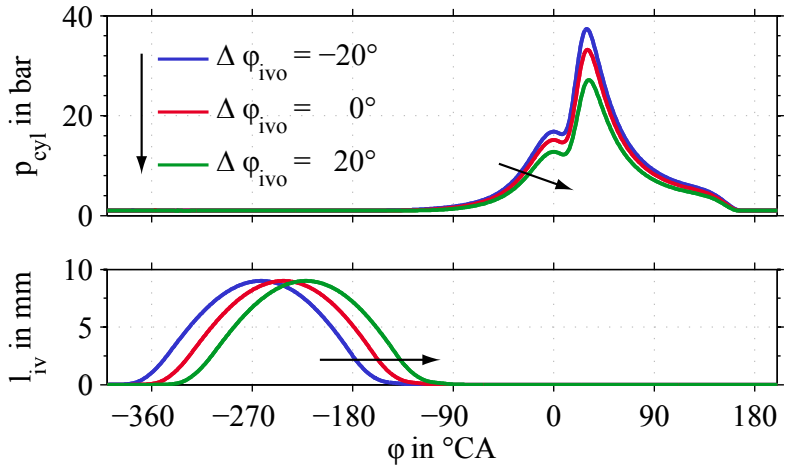

Figure 5.10.: Effect of $\Delta\varphi_{ivo}$ variation on in-cylinder pressure, $n = 1000$ min^{-1}

Additionally to the intake camshaft, whose phase can be adjusted in the examined engine concept, an exhaust cam phase variation is applied as well to show the potential effects. The exhaust valve phase shift directly determines the amount of work transferred to the crankshaft as a later timing delays blow-down and increases expansion work. However, the increased valve overlap with the corresponding effects on the exhaust gas recirculation as described in Sec. 3.8, have to be taken into account.

Accordingly, Fig. 5.11 shows the basic relationship between exhaust valve timing and in-cylinder pressure. An early exhaust valve opening reduces the effective expansion stroke and in turn the work transferred to the crankshaft. A late exhaust valve opening increases both the transferred work and EGR.

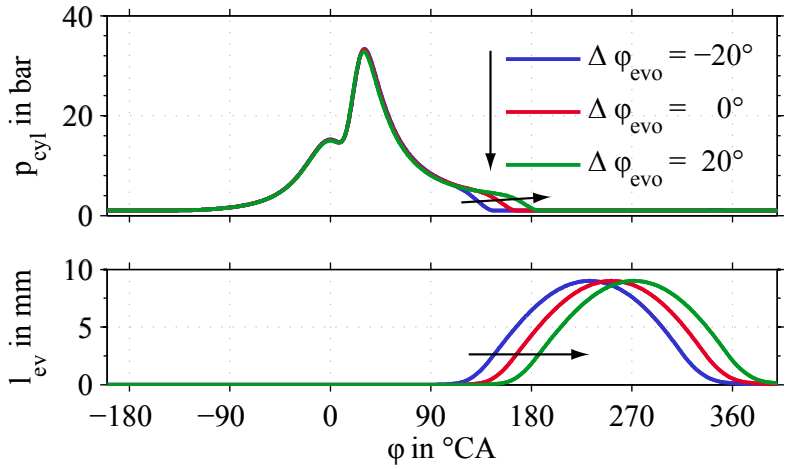

Figure 5.11.: Effect of $\Delta\varphi_{evo}$ variation on in-cylinder pressure, $n = 1000$ min^{-1}

For the cold start case a similar cam phase variation is generated. The resulting engine speed after the first four combustions is depicted in Fig. 5.12. A maximum is apparent for $\Delta\varphi_{ivo}$ = -20°, i.e. for early intake valve closing (Fig. 3.11).

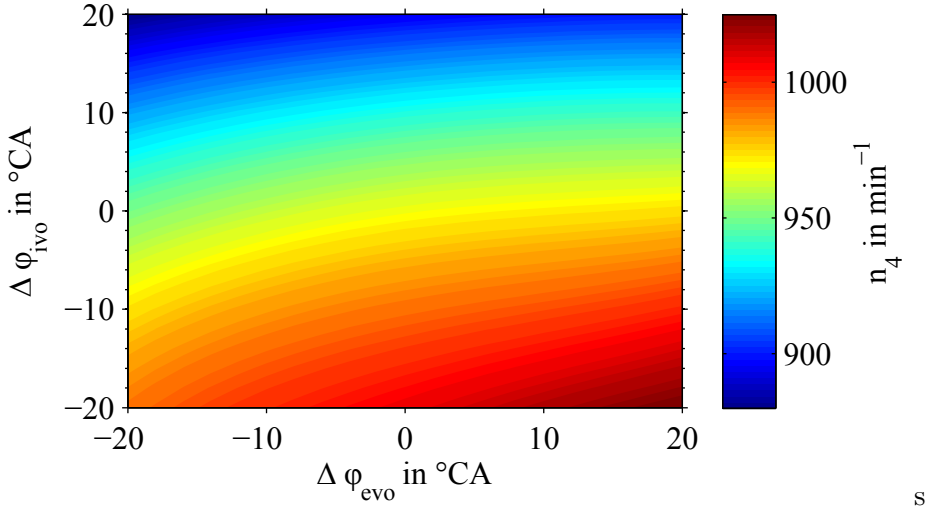

Figure 5.12.: Engine speed after the first fired cycle as a function of intake $\Delta\varphi_{ivo}$ and exhaust valve phase shifting $\Delta\varphi_{evo}$

For a given engine the course of engine speed during start is mainly a function of indicated mean effective pressure, which in turn is - with a constant spark timing - a direct function of volumetric efficiency and expansion stroke. Therefore, a late intake valve opening leads to a lower volumetric efficiency which is visible in Fig. 5.13. Furthermore, it is obvious that exhaust valve phase shift has a negligible effect on engine speed development.

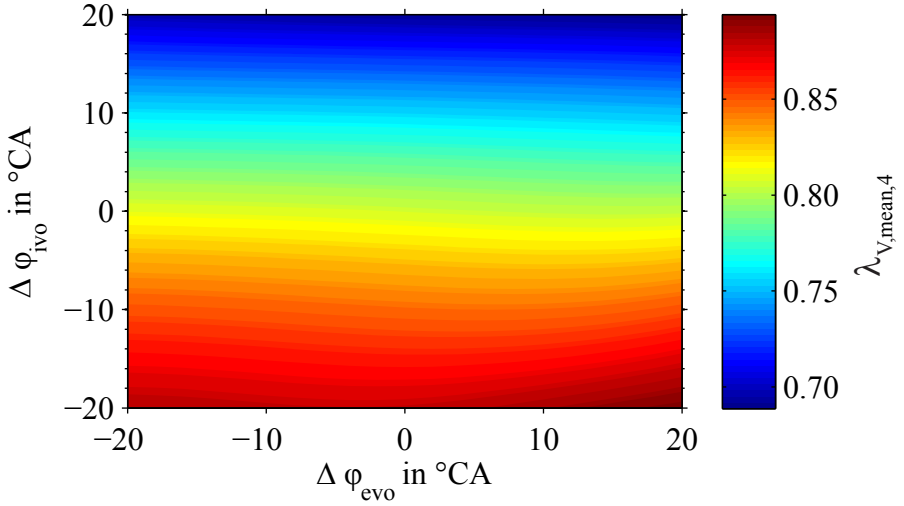

Figure 5.13.: Mean volumetric efficiency for the first fired cycle as function of intake $\Delta\varphi_{ivo}$ and exhaust valve phase shifting $\Delta\varphi_{evo}$

5.1.7. Stratified Operation

During cold start a stratified mixture operation is employed to reduce THC emissions. Stratified operation stands for an injection in the compression stroke as opposed to a homogeneous operation with an injection in the intake stroke. The applied approach to model this operation is outlined in Sec. 3.2.2. The differentiation of the cylinder volume into a mixture and a combined air-EGR zone enables the input of equivalence ratios of the mixture λ_{mix} and the complete charge in the cylinder λ_{global} and finally the simulation of a stratified charge combustion. An operation with increased global equivalence ratio and a fixed mixture equivalence ratio λ_{mix} exhibit a reduction in integral heat release, as expected by a lowered fuel mass burnt, Fig. 5.14. The center of combustion, however, occurs earlier than compared to the case with $\lambda_{global} = 1.0$.

This can be explained by the decreased distance the flame has to travel because of the decreased volume of the mixture zone. The resulting cylinder pressure behaves accordingly.

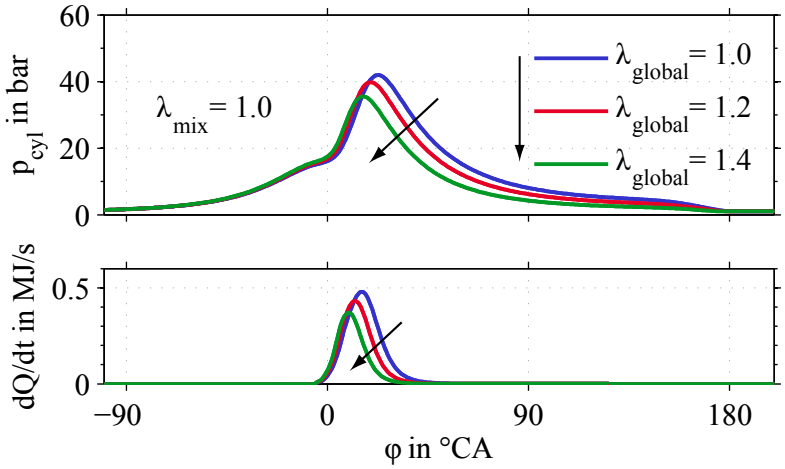

Figure 5.14.: Effect of global λ-variation on cylinder pressure and heat release rate, $\lambda_{mix} = 1.0$, $n = 1000$ min^{-1}

An increased global equivalence ratio decreases the maximum pressure value and shifts the maximum pressure according to the heat release rate.

Another characteristic of an increase in global equivalence ratio is the increased air mass trapped in the cylinder which leads to a higher compression pressure and partly compensates for the lowered fuel mass, which is injected at a higher global equivalence ratio. This effect occurs due to the reduced exhaust gas temperatures that is caused by a larger amount of unburnt air. Therefore, temperature in the cylinder during intake stroke is also reduced, leading to an increase in volumetric efficiency.

Fig. 5.15 shows the results of a variation of mixture equivalence ratio with fixed global equivalence ratio. According to the laminar flame speed dependence upon equivalence ratio, Sec. 3.4.3, the heat release rate exhibits a maximum at an equivalence ratio of around $\lambda_{mix} = 1.0$. With a leaner mixture the flame velocity decreases and the maximum of heat release rate and in-cylinder pressure occur delayed.

As expected, different air-fuel mixtures require different ignition timings for an optimal combustion concerning efficiency. Another degree of freedom is introduced by the stratified charge operation, where global equivalence ratio is compounded by the mixture equivalence ratio necessitating a further engine calibration.

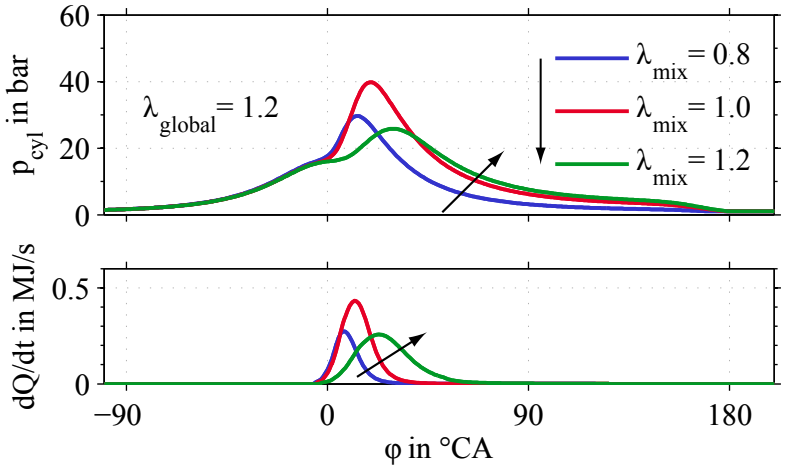

Figure 5.15.: Effect of mixture λ-variation on cylinder pressure and heat release rate, $\lambda_{global} = 1.2$, $n = 1000$ min^{-1}

5.2. Optimal Start

Cold start optimization can have several optimization criteria such as robustness, start-up time, pollutant and noise emission. Robustness is the most critical, since it is the prerequisite for other criteria. This fact is exemplified in Fig. 5.16.

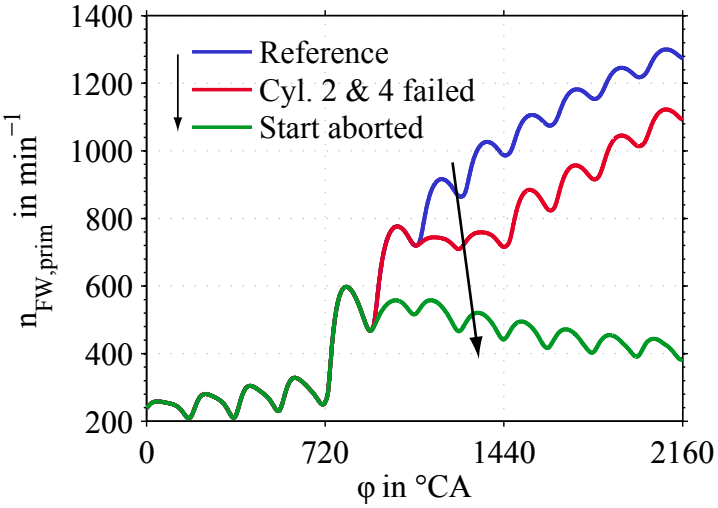

Figure 5.16.: Examples for different degrees of start success representing the robustness of starting performance

A successful reference start is compared to a semi-successful start with cylinders two and four exhibiting incomplete combustions and a failed start aborted after the first complete

combustion. Even if the start event shows several failed combustions but reaches the idle speed threshold at last, this still implies an increase in pollutant emissions and starting time.

As mixture preparation is not modeled explicitly, robustness can not be evaluated directly. Instead the speed gradient, here the engine speed after the first cycle, is chosen. The optimal parameter values for a speed-optimal start can be determined in different ways. The most obvious would be to examine two- or three-dimensional maps of the system's response to input parameters. An example for this approach is given in Fig. 5.17. The map shows the engine speed as a response of a variation of equivalence ratio λ and spark timing φ_{ign}. Fig. 5.17 contains several statements. An optimum in engine speed in regard to equivalence ratio and spark timing is apparent at around $\lambda = 1.0$ and $\varphi_{ign} = 10°$ BTDC. Furthermore, an optimum spark timing with respect to equivalence ratio can be obtained, which is displayed by the white arrow. The background to this relationship is the lowered laminar flame speed with increasing equivalence ratio.

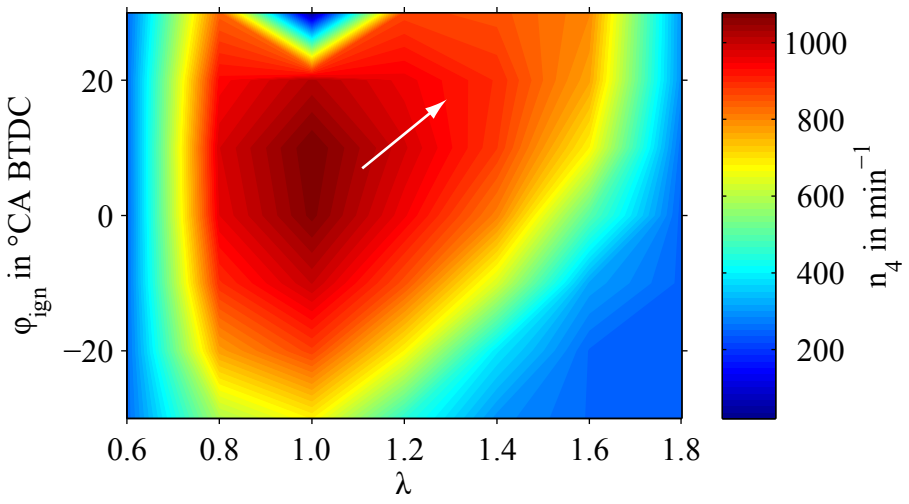

Figure 5.17.: Engine speed after the first fired cycle with time of ignition φ_{ign} and equivalence ratio $\lambda = \lambda_{global} = \lambda_{mix}$ as input. The white arrow denotes the increasing necessary spark advance with increasing equivalence ratio.

This method has the advantage of visualizing the system's response and therefore obtaining a better understanding of the problem. These maps not only show optima but also limits to engine operation. For example in Fig. 5.17 at $\lambda = 1.0$ and $\varphi_{ign} = 30°$ BTDC, the engine fails to run up in contrast to other values of the equivalence ratio at this spark timing. Here

again, the maximum in flame speed is the cause for the very early combustion leading to a larger amount of work transferred to the crankshaft before TDC.
This optimization method does, however, exhibit limitations in obtaining the global optimum for multi-dimensional problems as each map is limited to three dimensions representing only a section of the whole hyperspace.

Therefore, another optimization approach applied here is based upon automatic optimization algorithms outlined in Sec. 4.2. To this end, the engine models output, namely engine speed, is supplied to the algorithm, which employs a characteristic search strategy. Parameters α_{th}, φ_{ign}, $\Delta\varphi_{ivo}$, λ_{global} and λ_{mix} are chosen as free input parameters for a given ambient temperature and pressure. Incorporation of phase shift of the exhaust camshaft $\Delta\varphi_{evo}$ is omitted here as the influence on the start process is low and would have led to an increased computational effort, because the effort increases exponentially with dimensions. Fig. 5.18 shows the optimization process with the loss function $g(\boldsymbol{\Theta}) = -n_4$. The negative sign is applied as the optimization calls for a variable to minimize. The computation time for a single cold start of a four-cylinder engine with 1.2 s duration is 2 min 46 s[1]. For an optimization run with 500 cold start evaluations this sums up to 23 h and is still viable as an engineering tool.

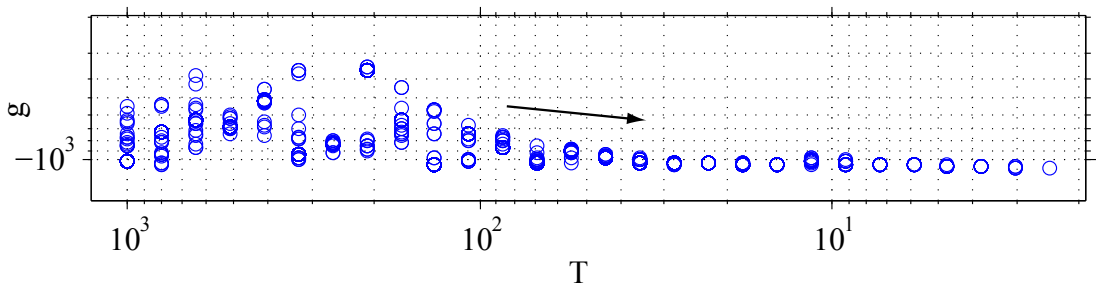

Figure 5.18.: Cold start optimization process with loss function $g(\boldsymbol{\Theta}) = -n_4$ with respect to optimization temperature T. Circles denote individual simulation runs.

The optimization nets in an engine speed improvement of 119 min^{-1} for the operation parameters shown in Tab. 5.2, from 971 min^{-1} for the reference case to 1090 min^{-1} (Fig. 5.19).

In conclusion, both optimization approaches mentioned are legitimate tools for an engi-

[1] On an Intel i7-860 with 8 GB main memory on a single processor core.

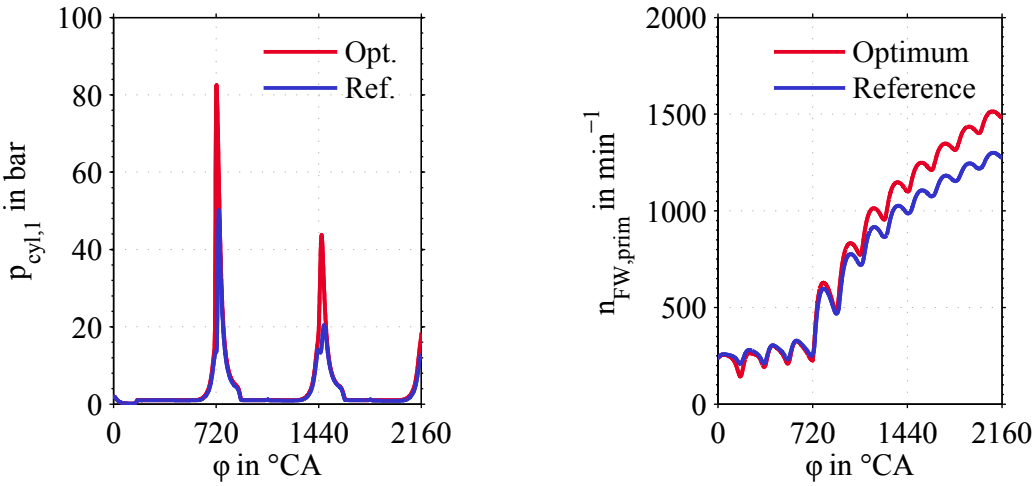

Figure 5.19.: Cold start optimization result, (a) in-cylinder pressure of cylinder one, (b) engine speed

Table 5.2.: Optimal operation parameters for $p_{amb} = 1.013$ bar and $\vartheta_{amb} = 20°C$

Parameter	α_{th}	φ_{ign}	$\Delta\varphi_{ivo}$	λ_{global}	λ_{mix}
Unit	%	°CA BTDC	°CA	-	-
Value	100	14.1	-19.6	0.99	0.98

neering process. Although the manual search has difficulties in finding the optimum in multi-dimensional search space, it is valuable in obtaining information about the general properties of the process to be optimized. As an example, Fig. 5.17 shows a correlation between equivalence ratio and spark timing for the maximum engine speed that would not have been identified with an automatic optimization. Furthermore, it is wise to verify the sensitivity of each parameter in order to reduce the input parameters for the optimization algorithm. Where the manual search enhances understanding of the process in general, the automatic optimization algorithm identifies the optimum with reasonable effort and increases the probability that it is a global one.

5.3. Measurement Evaluation

The enhancement of the information yield from a given measurement can be another task of the engine model. This is possible by fitting simulation results to experimental data and, due to the physically based nature of the model, studying other quantities that are not measured directly. This includes heat release rate determination as well as indicated mean effective pressure and equivalence ratio estimation.

5.3.1. Heat release rate

The heat release rate $\dot{Q}_b$ of a combustion can be determined by applying the energy conservation in the control volume, Eq. (3.17), to a measured in-cylinder pressure signal:

$$\frac{dU}{dt} = \dot{Q}_W - p\dot{V} + \dot{H}_{iv} + \dot{H}_{ev} + \dot{H}_{leak} + \dot{H}_f - \dot{H}_{f,v} + \dot{Q}_b$$

which simplifies during the closed valves phase to

$$\frac{dU}{dt} = \dot{Q}_W - p\dot{V} + \dot{H}_{leak} + \dot{H}_f - \dot{H}_{f,v} + \dot{Q}_b \; . \tag{5.3}$$

All other terms are modeled by the complete simulation model described in Chapter 3. Integrating the heat release rate then gives the heat release Q_b as shown in Fig. 5.20. Determination of combustion phases, cumulative heat release and, with limitations, converted fuel mass is then possible.

5.3.2. Indicated mean effective pressure

A variant of this approach is the *imep*-estimation off of the speed signal during cold start, i.e. the obtaining information about indicated mean effective pressure of every cycle by evaluating the measured high resolution speed signal. Prerequisite is the reliable reproduction of the influence of the powertrain on the speed signal. Sec. 3.10.1 and 4.3 show that this requirement is met here. Each cycle can now be assessed individually regarding indicated mean effective pressure by iteratively adjusting spark timing as to fit the speed signal optimally.

The result of such an optimization is shown in Fig. 5.21. Indicated mean effective pressure of

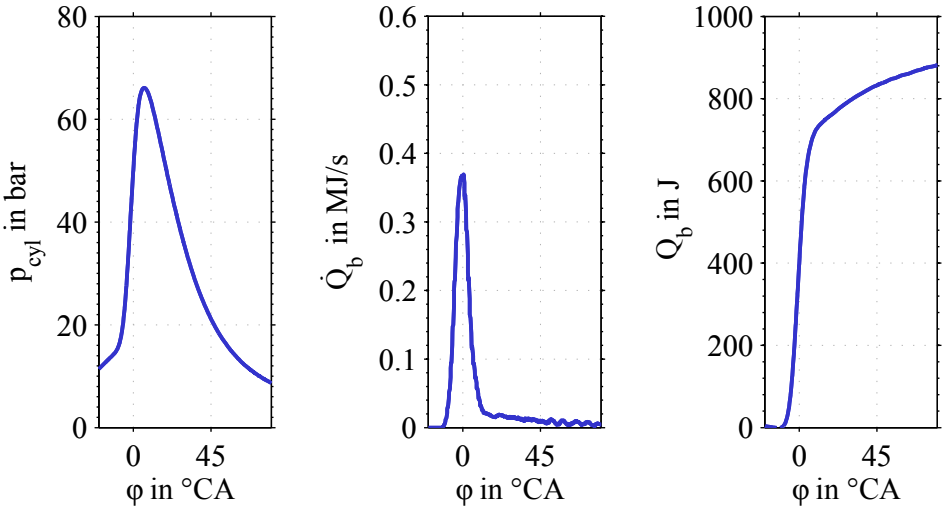

Figure 5.20.: In-cylinder pressure, heat release rate and cumulative heat release of an exemplary combustion during cold start

combustion analysis and of speed evaluation show a reasonable match. A deviation of both is, however, visible for the second and third combustions respectively. The reason can be attributed to the flywheel model, which is quite simple in its structure compared to reality and should therefore be refined.

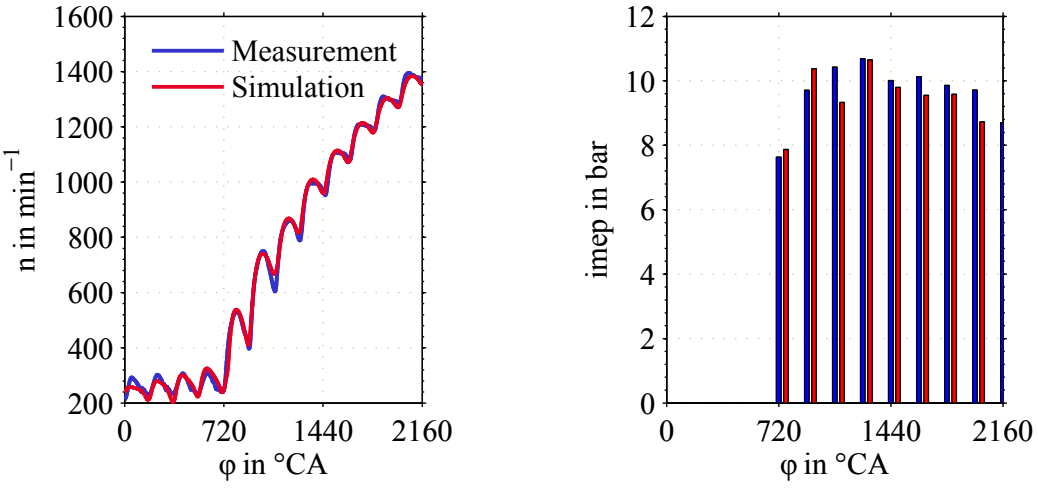

Figure 5.21.: Modeled indicated mean effective pressure from measured speed signal, (a) measured and modeled engine speed, (b) indicated mean effective pressure from combustion analysis and simulation

5.3.3. Equivalence ratio

Apart from *imep*-estimation, another possibility to apply the engine model in the context of measurement evaluation is the use as an *imep*-based equivalence-ratio estimator. As described in Sec. 1.1 equivalence-ratio measurement during cold start is tied to restrictions caused by an inactive sensor and exhaust gas dilution.

Information about air mass in the cylinder and injected fuel mass is not sufficient to determine effective equivalence ratio as of Eq. (3.13). This is caused, in contrast to warmed up conditions, by the incomplete fuel evaporation at cold start conditions. As a consequence, a model based λ-estimation shall be presented. By comparing the heat release rate of experimental data with simulation runs, the equivalence ratio(s) can be adjusted to fit the simulation heat release rate optimally to the measurement. An exemplary result for the assumption of a homogeneous mixture is presented in Fig. 5.22.

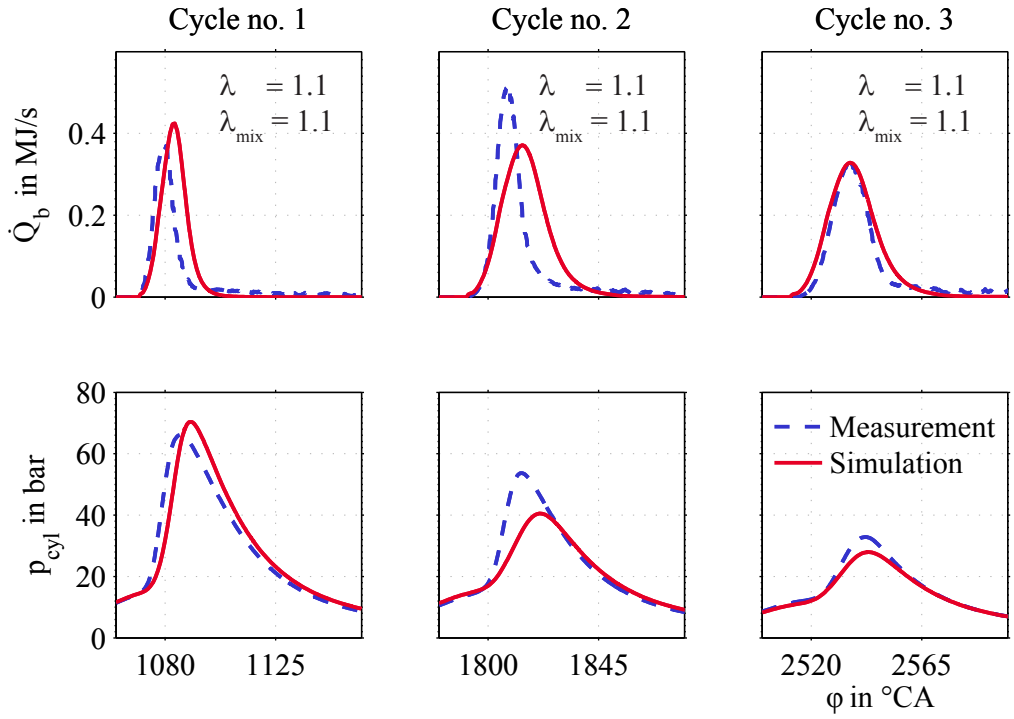

Figure 5.22.: Heat release rate $\dot{Q}_b$ and corresponding pressure of the second firing cylinder during start. Simulation run with *homogeneous* mixture for the first three cycles. λ-values are set to 1.1 for a best fit under the constraint of a homogeneous charge.

Cycles one to three of the second firing cylinder are depicted where both mixture and global equivalence ratio are set to the same value of 1.1, which resembles the best fitting value

in this case. Boundary conditions are set to values of Tab. 5.1. As injection takes place during the compression stroke (φ_{eoi}=65° BTDC), the fuel is not distributed homogeneously throughout the cylinder forming a stratified charge. This is modeled insufficiently with the homogeneous-mixture approach as can be seen by late heat release rates compared to measurement ones.

Hence, the stratified mixture model is employed by supplying different values for global and mixture equivalence ratios. These equivalence ratios act as free parameters during an optimization of the deviation between measured and simulated heat release rates. Fig. 5.23 shows that the global charge is slightly leaner than the mixture zone. The tendency of the fuel-ratio to approach unity in the second and third cycle can be explained by improved evaporization conditions as the start evolves: engine speed increases leading to a higher charge motion, rail pressure reaches its nominal value and wall temperature increases as well due to previous combustions.

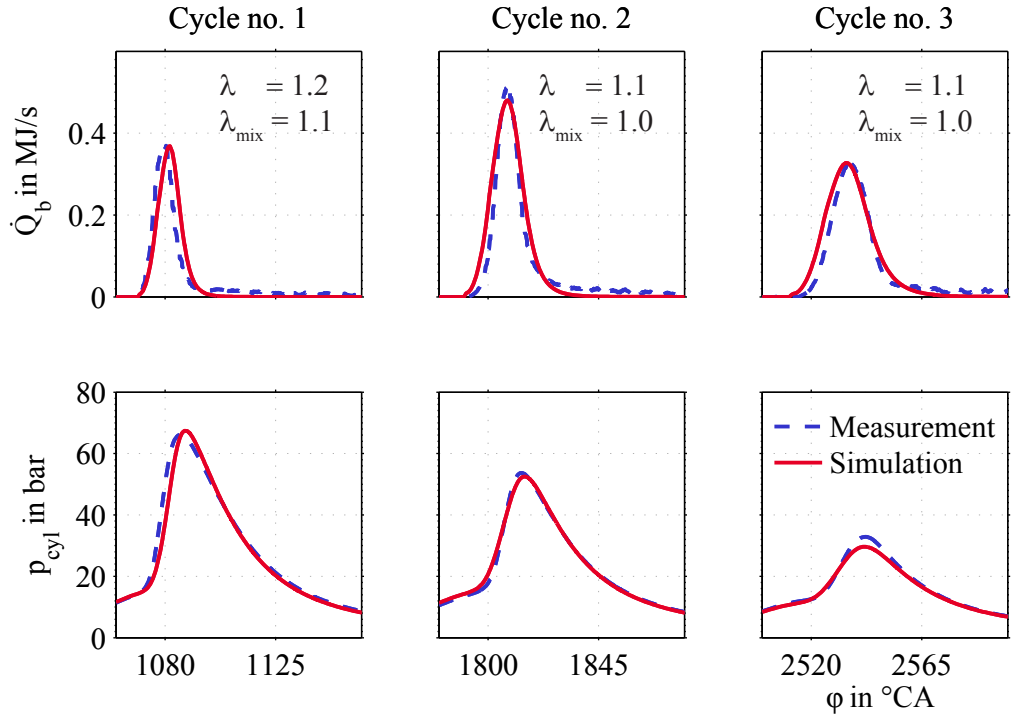

Figure 5.23.: Heat release rate $\dot{Q}_b$ and corresponding pressure of the second firing cylinder during start. Simulation run with *stratified* mixture for the first three cycles. λ and λ_{mix} are set to the best fitting values.

5.4. Summary

The chapter shows the utilization of the engine model as a means of increasing the understanding of the strongly instationary cold start process. Parameter variations can be conducted with little effort and show the correct trends, which can give hints on how to proceed in the calibration of the ECU with operation parameter variation such as valve phase shift, throttle angle and equivalence ratio. The physical background of the model enables geometry variations to show reasonably reliable trends. Furthermore, optimization of the cold start is possible. This a-priori optimization with a model is not meant to replace real experiments but can reduce the necessary effort of identifying an optimum by supplying good initial values for the optimization at a test bench. At last, the engine model can be used for measurement evaluation in order to estimate indicated mean effective pressure during start from engine speed signal and equivalence ratios from heat release rates.

6. Conclusion and Outlook

6.1. Conclusion

Optimizing the cold start of an SI engine is a challenging task due to several reasons. The engine start is characterized by a high dynamic and a short duration with operation points not encountered elsewhere during engine operation, e.g. low engine speeds with high load. Hence, substituting cold start experiments by experiments with a fully warmed up engine is restricted, if an accurate ECU calibration is to be achieved. Another challenge is the delay between experiments, which is caused by the requirement to condition the engine block temperature to a defined value. Furthermore, the cold start suffers from a highly stochastic nature, meaning cyclic variations occurring during normal engine operation are not averaged out by many cycles but, instead, are amplified by the transient run-up. This requires repetition of experiments to ensure significant results. The increasing number of ECU parameters to be calibrated allow for better optima to be achieved on the one hand but increases the calibration effort exponentially on the other. These factors taken into account lead to high expenses if cold start calibration is to be based exclusively on experimental data.

To support the application engineer an engine model is presented that complies with the requirements of reasonable computational cost and precise cold start prediction. In contrast to most modeling approaches found in literature it is capable of both simulating the complete cold start with individual working cycles and additionally enhance information content by indirectly deducing quantities which can not be measured directly. The model falls into the gray box category, i.e. it is based on physical laws and augmented by empirical models. A quasi-dimensional approach was chosen in order to limit the computing time and simultaneously to enable a flexible modeling with incorporation of geometric features of

the engine at hand. In this context, quasi-dimensional means modeling processes not only zero-dimensional but with abstract information about the geometry of certain sub-processes such as the flame propagation.

The thermodynamical part of the engine model consists of control volumes of the cylinders and the intake and exhaust manifolds. These control volumes are stated by mass and energy balances as well as gas equations of state. Gas properties are determined via the chemical software *Cantera* and stored in look-up tables for exhaust gas and air. The gaseous fuel is treated by polynomial approaches found in literature. Losses during the engine operation such as wall heat transfer and gas blow-by, which are especially severe during cold start, are depicted as well by appropriate models. A flame model based upon fractal theory describes the flame propagation. A requirement for the flame propagation modeling is the knowledge of turbulence level. Turbulence in turn is determined by a K-k-model. Fuel injection is modeled with a simplistic approach that assumes evaporation as a function of a time constant.
Control volumes are connected by one-dimensional orifice models delivering the mass flow. Separate approaches cover different restriction types such as throttle plate and valves. The thermodynamical part of the engine model provides state variables of the control volumes of the engine such as pressures, temperatures and masses. Pressure in the combustion chambers then yields the forces acting on the pistons driving the powertrain. The powertrain is represented by a mechanical model that contains the energy balances for the discretized engine mechanics containing crankshaft, con-rods and flywheel. The compound of crankshaft and flywheel consists of spring-damper elements representing a one-dimensional shaft. An empirical friction model is used in order to estimate the friction mean effective pressure. Purpose of the mechanical model is the prediction of time-resolved crankshaft speed during cold start. Engine speed is a signal that is measured in a serial engine ECU configuration and can therefore be studied with ease.

Complementary to the development of the engine model, measurements were carried out to gain insight into the particularities of the SI engine cold start and also to calibrate the engine model with suitable data. To this end, a test bench with a four-cylinder passenger-car SI engine coupled with standard measurement equipment was installed. The necessary

calibration of the different submodels was achieved by a global optimization algorithm. Finally, the models show a satisfactory agreement of measurement and simulation. This applies to stationary operation points as well as to instationary cold start operation. As a result, the engine model accepts a range of engine input parameters equally to the ECU input to a real engine. Spark advance, throttle angle, intake valve phase shift and equivalence ratio can be supplied in addition to boundary conditions such as ambient temperature and pressure as well as air humidity. It could be demonstrated that the model reacts reasonably to these inputs.

To show the potential of the engine model it was then subject to different parameter variations. Engine geometry parameters such as flywheel inertia, number of cylinders and compression ratio were investigated. As expected, with increasing inertia a delayed start-up was observed. Cylinder number variation showed that a lowered cylinder number led to a lower maximum engine speed. Especially with the two-cylinder case, a severe decrease in start robustness is apparent due to an increased speed fluctuation caused by long intervals between firing cylinders.

Apart from geometric parameters, the influence of boundary conditions was also investigated. A decrease in ambient pressure leads to a decreased engine speed flare since less air is delivered to the cylinder. Simulation results, however, showed a low impact of throttle plate angle on the volumetric efficiency at low ambient pressure. Additionally, the ECU parameters valve phase shift and equivalence ratio were varied in order to show general interrelationships.

Parameter variations are well suited for deepening the understanding of the underlying processes modeled. They are, however, limited to a few parameters only, since higher dimensional parameter spaces can not be visualized properly. In particular, if a global optimum is to be identified, it deems appropriate to apply a search algorithm. The optimum search was conducted in five dimensions of ECU parameters: throttle plate angle, spark timing, intake cam shift and equivalence ratios with the engine speed as maximization criterion. An optimum could be identified that increased the engine speed during cold start by about 10 %.

Apart from simulating the whole cold start process a priori, it is also possible to utilize the model for measurement evaluations. This encompasses determination of indicated mean effective pressure and equivalence ratios respectively. The indicated mean effective pressure was derived by the mechanical model from measured high resolution engine speed during a start, equivalence ratio by means of the complete engine model by comparing the burn rates of measurement and simulation. The indicated mean effective pressure showed a satisfactory agreement with measurement data, the equivalence ratio could not directly be validated since no data was available in the scope of this work.

In conclusion, modeling the thermodynamic as well as the mechanical part of the engine, as far as the torques and angular speeds are concerned, is possible with this model approach. The model complies with the aforementioned requirements of low computational effort and flexibility. Several advantages justify the effort for implementation and calibration of such an engine model. Further insight is gained into the process as variables are simulated that can otherwise only be determined with high effort. The model supports the ECU calibration process in providing data of parameter studies and increasing the information gain of experimental data. It can be configured to different engine configurations relying mainly on the mathematical description of physical laws.

6.2. Outlook

The engine model is capable of simulating gas exchange, combustion and engine run-up. It is, however, not capable of simulating the mixture preparation process adequately. On the contrary, equivalence ratio during the individual engine cycles has to be supplied as a free model parameter.
This, on the one hand, makes a parameter variation possible in order to investigate the influence of equivalence ratio on the engine cycle. On the other hand, it is not suited for varying ECU parameters affecting mixture preparation such as rail pressure, injection timing(s) and injection mass split. It is thus the next logical step to implement an evaporation model, which delivers equivalence ratio directly. Several variants are possible to model injection and evaporation of fuel in the cylinder volume. CFD or 0D-model each with parcel spray modeling respectively or x-τ-models for the description of fuel wall film.

CFD-code with proprietary spray models most often apply a Lagrangian approach of tracking the droplet parcels. These in turn represent a number of droplets - the so-called discrete droplet model. Gas and liquid phases are coupled by mass, energy and momentum balances. This makes the simulation of penetration of the spray cone, heat and mass transfer between droplets and the surrounding gas possible. Problematic with CFD methods in general are the costly mesh generation and the high computational effort[1]. This is especially valid for cold start, where several engine cycles are to be simulated for a single start.

Parcel tracking is also possible within the scope of 0D-modeling, with the obvious loss in spatial resolution. The model approach is almost identical to that of the CFD-method. This results in a lower but in most cases still acceptable accuracy. It benefits, however, by a significant lower computational effort than spray modeling with CFD.

The least complex method of mixture preparation modeling is of the family of x-τ-models for the description of fuel wall film dynamics. These models were developed for manifold injection engines, as outlined in Sec. 1.3. For DISI engines, however, no consistent set of parameter values can be found since boundary conditions for injection and mixture preparation are considerably more dynamic than for PFI engines.

In conclusion, the high cost for CFD as well as the low flexibility of the x-τ-model leaves the parcel model for 0D-simulation as the most valid option for modeling mixture preparation during cold start.

[1] If a grid size is chosen that guarantees a sufficiently high accuracy.

Bibliography

[1] *Standard Atmosphere, ISO 2533:1975.*

[2] AB, Dynasim: *Dymola.* http://www.3ds.com/products/catia/portfolio/dymola, 2009.

[3] Aquino, C. F.: *Transient A/F Control Characteristics of the 5 Litre Central Fuel Injection Engine.* SAE Technical Papers, 810494, 1981.

[4] AVL: *Indiset.* http://www.avl.com, April 2010.

[5] Baehr, H. D.: *Thermodynamik.* Springer Verlag, Berlin, 13. Auflage, 2006.

[6] Balashov, D., L. Burkovski, F. Ferderer, A. Fidlin, M. Kremer, B. Pennec, and R. Seebacher: *Simulation bei Drehschwingungsdämpfern.* ATZ Autotechnische Zeitschrift, 108:1038–1045, 2006.

[7] Baratta, M., E. Spessa, S. d'Ambrosio, and A. Vassallo: *Cycle-Resolved Detection of Combustion Start in SI Engines by Means of Different In-Cylinder Pressure Data Reduction Techniques.* ASME ICES2006-1367, 2006.

[8] Bargende, M.: *Ein Gleichungsansatz zur Berechnung der instationären Wandwärmeverluste im Hochdruckteil von Ottomotoren.* Dissertation, Technische Hochschule Darmstadt, 1990.

[9] Bargende, M., C. Burkhardt und A. Frommelt: *Besonderheiten der thermodynamischen Analyse von DE-Ottomotoren.* MTZ Motortechnische Zeitschrift, 62, 2001.

[10] Basshuysen, R. und F. Schäfer (Herausgeber): *Handbuch Verbrennungsmotor.* Vieweg, Wiesbaden, 2007.

[11] Bates, S. C.: *Flame Imaging Studies of Cycle-By-Cycle Combustion Variation in a SI Four-Stroke Engine.* SAE Technical Papers, 892086, 1989.

[12] Bird, R. B., W. E. Stewart, and E. N. Lightfoot: *Transport Phenomena.* John Wiley & Sons, Inc., New York, 2nd edition, 2002.

[13] Blizard, N. C. and J. C. Keck: *Experimental and Theoretical Investigation of Turbulent Burning Model for Internal Combustion Engines.* SAE Technical Papers, 740191, 1974.

[14] Bozza, F., A. Gimelli, S.S. Merola, and B.M. Vaglieco: *Validation of a Fractal Combustion Model through Flame Imaging.* SAE Technical Papers, 2005-01-1120, 2005.

[15] Brenan, K. E., S. L. Campbell, and L. R. Petzold: *Numerical Solution of Initial-Value Problems in Differential-Algebraic Equations.* North-Holland, New York, 1989.

[16] Cheng, W. K.: *Transient Engine Startup and Shutdown Process.* In Zhao, F. (editor): *Technologies for Near-Zero-Emission Gasoline-Powered Vehicles*, chapter 1, pages 1–29. SAE International, Warrendale, Pa., 2007.

[17] Csallner, P.: *Eine Methode zur Vorausberechnung der Änderung des Brennverlaufes von Ottomotoren bei geänderten Betriebsbedingungen.* Dissertation, Technische Universität München, 1981.

[18] Curtis, E., C. Aquino, D. Trumpy, and G. Davis: *A New Port and Cylinder Wall Wetting Model to Predict Transient Air/Fuel Excursions in a Port Fuel Injected Engine.* SAE Technical Papers, 961186, 1996.

[19] D'Errico, G. and A. Onorati: *An Integrated Simulation Model for the Prediction of GDI Engine Cylinder Emissions and Exhaust After-Treatment System Performance.* SAE Technical Papers, 2004-01-0043, 2004.

[20] Drake, M. C., T. D. Fansler, A. S. Solomon, and G. A. Szekely Jr.: *Piston Fuel Films as Source of Smoke and Hydrocarbon Emissions from a Wall-Controlled Spark-Ignited Direct-Injection Engine.* SAE Technical Papers, 2003-01-0547, 2003.

[21] Dresig, H.: *Schwingungen und mechanische Antriebssysteme.* Springer Verlag, Berlin, 2000.

[22] ETAS: *INCA.* http://www.etas.com/en/products/inca.php, April 2010.

[23] Fidlin, A. und R. Seebacher: *Simulationstechnik am Beispiel des ZMS.* In: *LuK Kolloquium*, 2006.

[24] Floudas, C. A. and P. M. Pardalos (editors): *Encyclopedia of Optimization.* Springer Verlag, Berlin, 2nd edition, 2009.

[25] Fox, J. A., W. K. Cheng, and J. B. Heywood: *A Model for Predicting Residual Gas Fraction in Spark-Ignition Engines.* SAE Technical Papers, 931025, 1993.

[26] Fritzson, F.: *Principles of Object-Oriented Modeling and Simulation with Modelica.* Wiley Interscience, 2004.

[27] Gandhi, A. H., C. E. Weaver, E. W. Curtis, T. F. Alger, C. L. Anderson, and D. L. Abata: *Spray Characterization in a DISI Engine During Cold Start: (2) PDPA Investigation.* SAE Technical Papers, 2006-01-1003, 2006.

[28] Gatowski, J. A., J. B. Heywood, and C. Deleplace: *Flame Photographs in a Spark-Ignition Engine.* Combustion and Flame, 56(1):71–81, 1984.

[29] GmbH, Testa: *FID.* http://www.testa-fid.de, 2010.

[30] Gouldin, F. C.: *An Application of Fractals to Modeling Premixed Turbulent Flames.* Combustion and Flame, 68(3):249–266, 1987.

[31] Grau, J. H.: *Modeling Methodology of a Spark-Ignition Engine and Experimental Validation-Part II: Gas Exchange Process.* SAE Technical Papers, 2002-01-2191, 2002.

[32] Grill, M.: *Objektorientierte Prozessrechnung von Verbrennungsmotoren.* Dissertation, Universität Stuttgart, 2006.

[33] Grünefeld, G., V. Beushausen, P. Andresen, and W. Hentschel: *A Major Origin of Cyclic Energy Conversion Variations in SI Engines: Cycle-by-Cycle Variations of the Equivalence Ratio and Residual Gas of the Initial Charge.* SAE Technical Papers, 941880, 1994.

[34] Grote, A.: *Zum Verhalten instationärer Kraftstoffwandfilme in Einlasskanälen von Ottomotoren.* Dissertation, Universität Karlsruhe, 1999.

[35] Hafner, K. E. und H. Maass: *Torsionschwingungen in der Verbrennungskraftmaschine.* Springer Verlag, Berlin, 1985.

[36] Hardenberg, H.: *Die Berechnung des freien Öffnungsquerschnittes von Kegelventilen.* MTZ Motortechnische Zeitschrift, 30:59–63, 1969.

[37] Heywood, J. B.: *Internal Combustion Engine Fundamentals.* McGraw Hill, New York, 1988.

[38] Hilditch, J., Z. Han, and T. Chea: *Unburned Hydrocarbon Emissions from Stratified Charge Direct Injection Engines.* SAE Technical Papers, 2003-01-3099, 2003.

[39] Hires, S. D., R. J. Tabaczynski, and J. M. Novak: *The Prediction of Ignition Delay and Combustion Intervals for a Homogeneous Charge, Spark Ignition Engine.* SAE Technical Papers, 780232, 1978.

[40] Hochgreb, S.: *Liquid Fuel Impingement on the Piston Bowl of a Direct-Injection, Spark-Ignited (DISI) Engine Under Stratified Operation.* SAE Technical Papers, 2001-01-3646, 2001.

[41] Hustad, J. E. and O. K. Sönju: *Experimental Studies of Lower Flammability Limits of Gases and Mixtures of Gases at Elevated Temperatures.* Combustion and Flame, 71:283–294, 1988.

[42] Incropera, F. P. and D. P. DeWitt: *Fundamentals of Heat and Mass Transfer.* John Wiley & Sons, Inc., New York, 1990.

[43] Jaegher, P. de: *Einfluss der Stoffeigenschaften von Verbrennungsgasen auf die Motorprozeßrechnung.* Postdoctoral Thesis, Technische Universität Graz, 1984.

[44] Kee, R. J., F. M. Rupley, and J. A. Miller: *CHEMKIN-II: A FORTRAN Chemical Kinetics Package for the Analysis of Gas-Phase Chemical Kinetics.* Sandia-Report, SAND89-8009, 1989.

[45] Kirkpatrick, S., C. D. Gelatt, and M. P. Vecchi, Jr.: *Optimization by Simulated Annealing.* Science, 220:671–771, 1983.

[46] Klein, D. and W. K. Cheng: *Spark Ignition Engine Hydrocarbon Emissions Behaviors in Stopping and Restarting.* SAE Technical Papers, 2002-01-2804, 2002.

[47] Klein, M. and L. Eriksson: *A Specific Heat Ratio Model for Single-Zone Heat Release Models.* SAE Technical Papers, 2004-01-1464, 2004.

[48] Koga, N.: *An Experimental Study on Fuel Behavior during the Cold Start Period of a Direct Injection Spark Ignition Engine.* SAE Technical Papers, 2001-01-0969, 2001.

[49] Kufferath, A., W. Samenfink und J. Gerhardt: *Die neue Emissionstrategie der Benzin-Direkteinspritzung.* Motortechnische Zeitschrift, 11:916–923, 2003.

[50] Kufferath, A., W. Samenfink, and J. Gerhardt: *High Pressure-Stratified Start, the Better Start Strategy for Gasoline Direct Injection.* In *12. Aachener Kolloquium Fahrzeug- und Motorentechnik*, 2003.

[51] Kulzer, A. C.: *BDE-Direktstart.* PhD thesis, Universität Stuttgart, 2004.

[52] Lechtape-Grüter, R.: *Rechnerische Simulation der Ölverbrauchs- und Öltransportwege im Bereich Kolben-Kolbenring-Zylinder.* Technischer Bericht, FVV, 1999.

[53] Lemmon, E.W., M.L. Huber, and M.O. McLinden: *NIST Standard Reference Database 23: Reference Fluid Thermodynamic and Transport Properties-REFPROP, Version 9.0*, 2010.

[54] Liebsch, S., O. Dingel, J. Maaß, M. Günther, M. Kratzsch, and S. Zwahr: *Model Based E85 Cold Start Optimization for DISI Engines.* SAE Technical Papers, 2009-01-1909, 2009.

[55] Luan, Y.: *Gasoline Engine Cold Start Fuel Calibration.* PhD thesis, Wayne State University, Detroit, Michigan, 2005.

[56] Mandelbrot, B. B.: *The fractal geometry of nature.* W. H. Freeman and Company, New York, 1983.

[57] MathWorks, The: *SIMULINK.* http://www.mathworks.com/products/simulink/, 2009. `http://www.mathworks.com/products/`.

[58] MathWorks, The: *xPC Target*. http://www.mathworks.com/products/xpctarget/, 2010. `http://www.mathworks.com/products/xpctarget/`.

[59] Matthews, R. D. and Y. Chin: *A Fractal-Based SI Model: Comparisons of Predictions With Experimental Data*. SAE Technical Papers, 910079, 1991.

[60] Meier, K.: *Berechnung der Schadstoffbildung im OTTO-Motor bei großen Abgasrückführraten*. Dissertation, Technische Hochschule Karlsruhe, 1997.

[61] Metghalchi, M. and J. C. Keck: *Burning Velocities of Mixtures of Air with Methanol, Isooctane and Indolene at High Pressures and Temperatures*. Combustion and Flame, 48:191–210, 1982.

[62] Modelica Association: *Modelica® - A Unified Object-Oriented Language for Physical Systems Modeling, Language Specification, Version 3.2*, March 2010.

[63] N. N.: *Cantera 1.7.1*. http://code.google.com/p/cantera/, 2009. `http://code.google.com/p/cantera/`.

[64] Nelles, O.: *Nonlinear System Identification*. Springer Verlag, Berlin, 2000.

[65] Otter, M.: *Objektorientierte Modellierung Physikalischer Systeme*. Automatisierungstechnik, 47:A1–A16, 1999.

[66] Patton, K. J., R. G. Nitschke, and J. B. Heywood: *Development and Evaluation of a Performance and Efficiency Model for Spark-Ignition Engines*. SAE Technical Papers, 890836, 1989.

[67] Peters, N.: *Laminar flamelet concepts in turbulent combustion*. Symposium (International) on Combustion, 21(1):1231–1250, 1988.

[68] Pischinger, R., M. Klell und Th. Sams: *Thermodynamik der Verbrennungskraftmaschine - Der Fahrzeugantrieb*. Springer Verlag, Wien, 2. Auflage, 2002.

[69] Poulos, S. G. and J. B. Heywood: *The Effect of Chamber Geometry on Spark-Ignition Engine Combustion*. SAE Technical Papers, 830334, 1983.

[70] Radhakrishnan, K. and A. C. Hindmarsh: *Description and Use of LSODE, the Livermore Solver for Ordinary Differential Equations.* Lawrence Livermore National Laboratory Report, UCRL-ID-113855, 1993.

[71] Rao, V. K., D. P. Gardiner, and M. F. Bardon: *Effects of Gas Leakage and Crevices on Cold Starting of Engines.* SAE Technical Papers, 940078, 1994.

[72] Reik, W.: *Höherer Komfort und weniger Geräusch durch das Zweimassenschwungrad.* ATZ Autotechnische Zeitschrift, 100:896–903, 1998.

[73] Reik, W., R. Seebacher und A. Kooy: *Das Zweimassenschwungrad.* In: *LuK-Kolloquium*, 1999.

[74] Russ, S.: *Spark Retardation for Improving Catalyst Light-Off Performance.* In Zhao, F. (editor): *Technologies for Near-Zero-Emission Gasoline-Powered Vehicles*, chapter 5, pages 157–171. SAE International, Warrendale, Pa., 2007.

[75] Sandoval, D. and J. B. Heywood: *An Improved Friction Model for Spark-Ignition Engines.* SAE Technical Papers, 2003-01-0725, (om), 2003.

[76] Santavicca, D. A., D. Liou, and G. L. North: *A Fractal Model of Turbulent Flame Kernel Growth.* SAE Technical Papers, 900024, 1990.

[77] Santoso, H. and W. K. Chen: *Mixture Preparation and Hydrocarbon Emissions Behaviors in the First Cycle of SI Engine Cranking.* SAE Technical Papers, 2002-01-2805, 2002.

[78] Scheele, M.: *Potentialabschätzung zur Verbesserung des indizierten Wirkungsgrades kleinvolumiger Ottomotoren.* Dissertation, Universität Stuttgart, 1999.

[79] Schintzel, K.: *Kohlenwasserstoff-Emissionen eines Motors mit Benzin-Direkteinspritzung und wandgeführtem Brennverfahren.* Dissertation, Universität Madgeburg, 2005.

[80] Schuerg, F., S. Arndt, D. Pfefferle, and B. Weigand: *An Injector-Specific, Analytic-Phenomenological Spray Propagation Model for the Application-Oriented Simulation of Direct Injection SI Engines.* SAE Technical Papers, 2007-01-1851, 2007.

[81] Schulze, A.: *Entwicklung eines eindimensionalen Drei-Wege-Katalysator Modells.* Dissertation, Universität Rostock, 2007.

[82] Shayler, P. J., C. Belton, and A. Scarisbrick: *Emissions and Fuel Utilisation After Cold Starting Spark Ignition Engines.* SAE Technical Papers, 1999-01-0220, 1999.

[83] Smith, G. P., D. M. Golden, M. Frenklach, N. W. Moriarty, B. Eiteneer, M. Goldenberg, C. T. Bowman, R. K. Hanson, S. Song, W. C. Gardiner, V. V. Lissianski, and Z. Qin: *Gri-mech 3.0.* www.me.berkeley.edu/gri-mech/, 2010. `www.me.berkeley.edu/gri-mech/`.

[84] Spalding, D. B.: *Mixing and chemical reaction in steady confined turbulent flames.* Symposium (International) on Combustion, 13(1):649–657, 1971.

[85] Stanglmaier, R., C. E. Roberts, Jr., O. A. Ezekoye, and R. D. Matthews: *Condensation of Fuel on Combustion Chamber Surfaces as a Mechanism for Increased HC Emissions From SI Engines During Cold Start.* SAE Technical Papers, 972884, 1997.

[86] Stegemann, F.: *Verbrennungsregelung auf Basis von Verbrennungsinformationen aus der hochaufgelösten Motordrehzahl.* Diplomarbeit, Hochschule Wismar, 2008.

[87] Stull, D. R. and H. Prophet: *JANAF Thermochemical Tables*. 1971.

[88] Suck, G.: *Untersuchung der HC-Quellen an einem Ottomotor mit Direkteinspritzung.* Dissertation, Otto-von-Guericke-Universität Magdeburg, 2001.

[89] Thomsen, J. J.: *Vibrations and Stability.* Springer Verlag, Berlin, 2003.

[90] Tiller, M.: *Introduction to Physical Modeling with Modelica.* Kluwer Academic Publishers, 2004.

[91] Turns, S. R.: *An Introduction to Combustion.* McGraw-Hill, Boston, 2. edition, 2000.

[92] Vibe, I. I.: *Brennverlauf und Kreisprozeß von Verbrennungsmotoren.* Verlag Technik, Berlin, 1970.

[93] Warnatz, J., U. Maas, and R. W. Dibble: *Combustion: Physical and Chemical Fundamentals, Modeling and Simulation, Experiments, Pollutant Formation.* Springer, Berlin, 4. edition, 2006.

[94] Wermuth, N.: *Emissionsminderung beim Kaltstart durch modellbasierte Motorsteuerung.* Dissertation, Technische Universität Braunschweig, 2002.

[95] Wiemer, S., H. Kubach, and U. Spicher: *Investigations on the Start-Up Process of a DISI Engine.* SAE Technical Papers, 2007-01-4012, 2007.

[96] Woschni, G.: *Universally Applicable Equation for the Instantaneous Heat Transfer Coefficient in the Internal Combustion Engine.* SAE Technical Papers, 670931, 1967.

[97] Yoshiyama, S., E. Tomita, Z. Zhang, and Y. Hamamoto: *Measurement and Simulation of Turbulent Flame Propagation in a Spark Ignition Engine by Using Fractal Burning Model.* SAE Technical Papers, 2001-01-3603, 2001.

[98] Zacharias, F.: *Analytische Darstellung der thermodynamischen Eigenschaften von Verbrennungsgasen.* Dissertation, Technische Universität Berlin, 1966.

A. Dymola Model Depiction

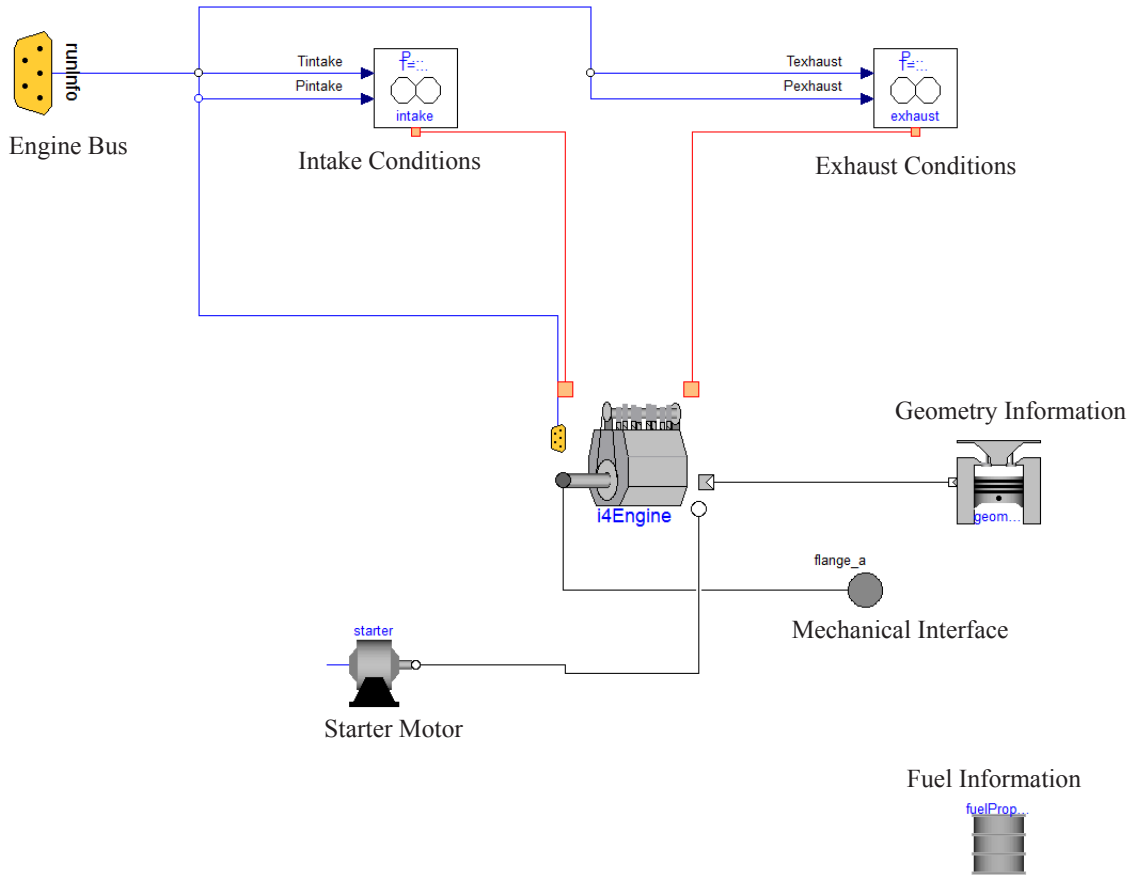

Figure A.1.: Depiction of the `EngineSetup` layer

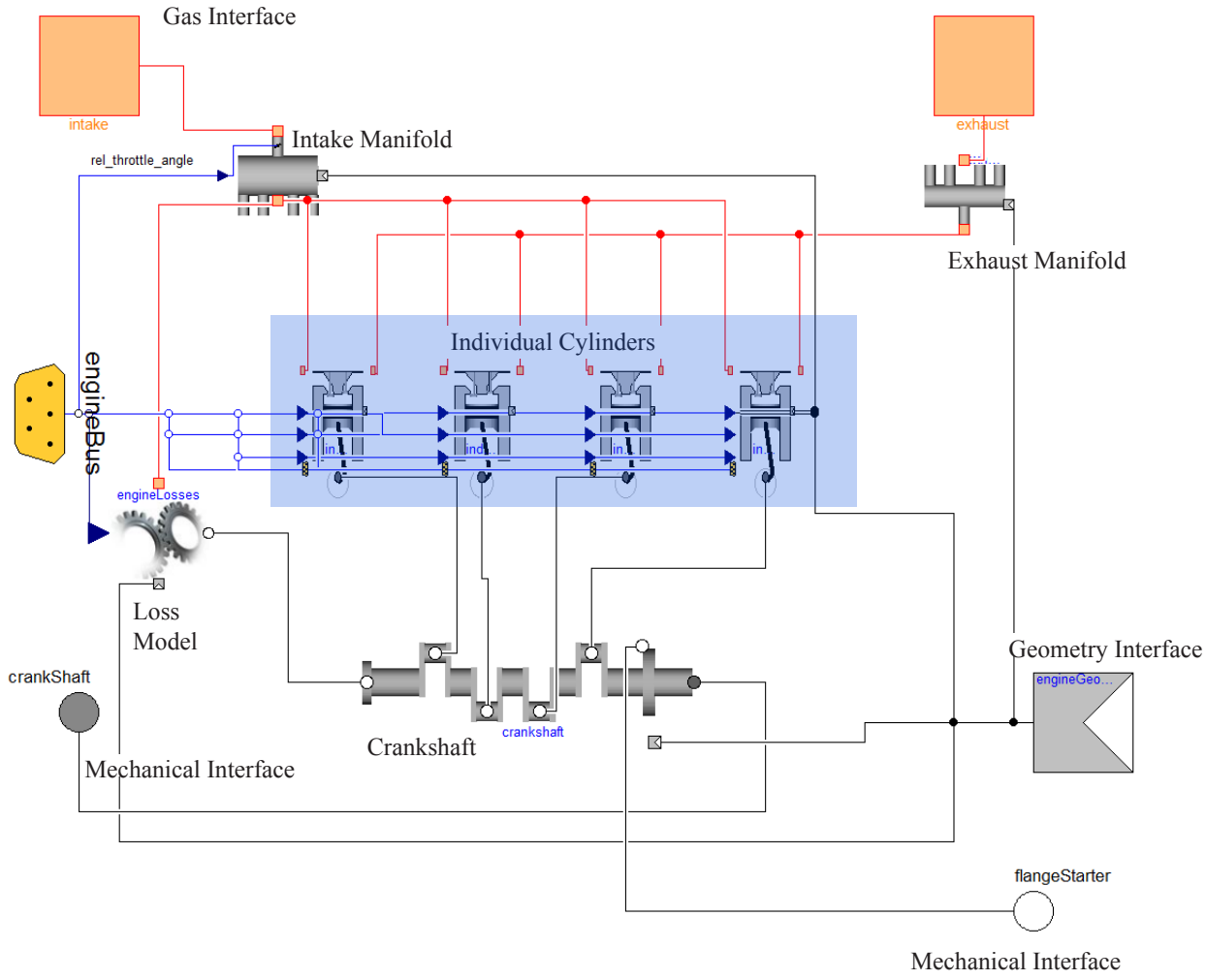

Figure A.2.: Depiction of the `Engine` model layer

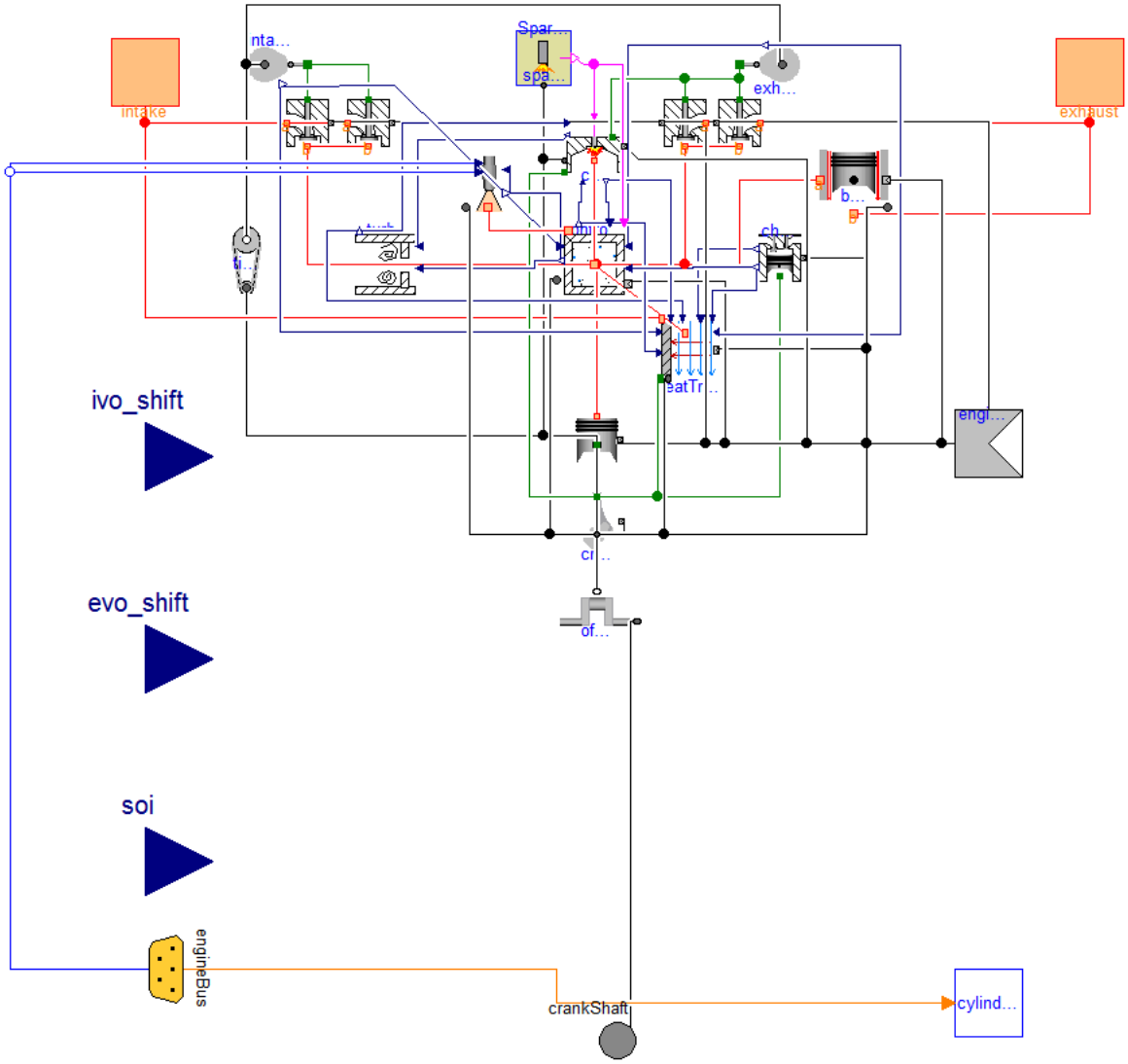

Figure A.3.: Depiction of the `IndividualCylinder` model layer

B. Flame Front Area

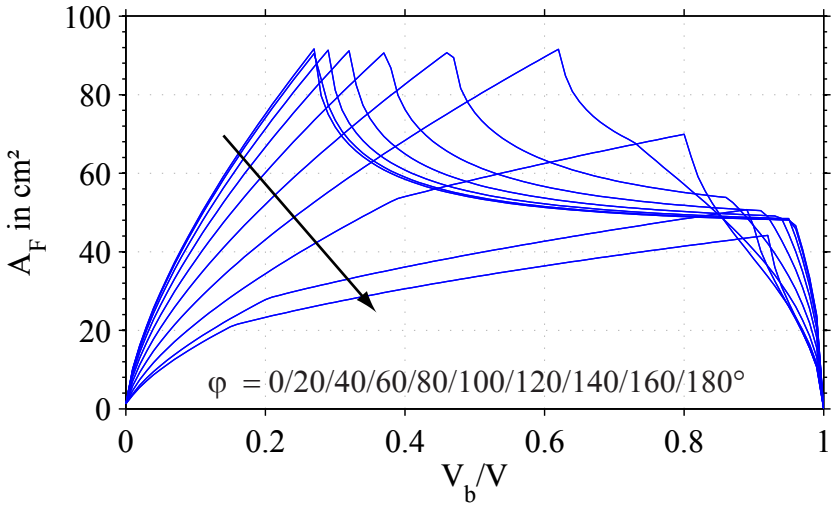

Figure B.1.: Calculated flame front area